

Interpretation of Scanning Tunneling Microscopy
and Spectroscopy of Magnetic Metal Surfaces by
Electron Theory

Daniel Wortmann

Elektronentheorie zur Beschreibung von
Rastertunnel-Mikroskopie und -Spektroskopie von
magnetischen Metalloberflächen

von
Daniel Wortmann

Diplomarbeit in Physik

eingereicht am
Fachbereich Physik
der
Universität Dortmund
im Februar 2000

angefertigt im
Institut für Festkörperforschung
Forschungszentrum Jülich

Contents

1	Introduction	1
2	Density-Functional Theory	5
2.1	The Hohenberg-Kohn theorem	6
2.2	The Kohn-Sham equation	7
2.3	The Local Density Approximation	9
3	The FLAPW-Method	11
3.1	The FLAPW Basis set inside the crystal	12
3.2	A full-potential method	14
3.3	FLAPW in film geometry	15
4	Theory of the STM	19
4.1	The Scanning Tunneling Microscope	19
4.2	Basic theory of tunneling	20
4.3	The Bardeen approach to tunneling	21
4.4	The tunneling current	25
4.5	Tersoff-Hamann's model	26
4.6	Chen's extensions to the Tersoff-Hamann model	28
4.7	'Technical' Aspects	29
4.7.1	Calculation of the corrugation-amplitude	30
4.7.2	Star representation of the corrugation-amplitude	31

5	STM of the $c(2\times 2)$MnCu/Cu(100) surface alloy	35
5.1	Review of experimental results	35
5.2	$c(2\times 2)$ MnCu alloy on the Cu(100) surface	38
5.2.1	Corrugation of the unrelaxed $c(2\times 2)$ MnCu surface alloy	40
5.3	The relaxed surface alloy	46
5.3.1	$p(2\times 2)$ MnCu alloys on the Cu(100) surface	48
5.4	Comparison with the experiments	50
5.5	Effect of an increased exchange splitting	52
5.5.1	Anti-ferromagnetic ordering	54
5.6	STS of the $c(2\times 2)$ MnCu surface alloy	56
6	Buried magnetic alloys	61
6.1	Buried $c(2\times 2)$ MnAg alloys	62
6.1.1	The $c(2\times 2)$ MnAg surface alloy on Ag(100)	62
6.1.2	Subsurface MnAg alloys	64
6.2	Scanning tunneling spectroscopy of buried alloys	66
6.3	Imaging the deeply buried alloy	70
6.3.1	Quantum wells	70
6.3.2	Calculation of deeply buried alloys	73
6.3.3	The film as a model of the semi-infinite crystal	75
6.3.4	STM images of deeply buried $c(2\times 2)$ MnAg alloys	77
6.3.4.1	Majority spin contribution	78
6.3.4.2	The minority spin contribution	80
6.3.4.3	Imaging through quantum well states	85
7	Summary and Outlook	87
	Bibliography	89

Chapter 1

Introduction

The science on the nano-scale is one of the most fruitful and exciting areas of the current physics of condensed matter. It has become possible during the last several years by a group of exciting new experimental methods which allow to investigate surfaces with high real space resolution. These methods are summarized as Scanning Probe Methods. They all implement the same simple principle: a nano-scale probe is approached towards the sample surface of interest until some physical process occurs which can be used to characterize the sample.

The oldest of those methods is the Scanning Tunneling Microscopy (STM) which exploits the quantum mechanical tunnel-effect to obtain information about the sample surface. After this first example of a Scanning Probe Microscope (SPM) a huge number of variations have been developed. Most frequently used is the Atomic Force Microscopy (AFM), which measures the force acting on the probe in the vicinity of the surface. Furthermore, other methods measuring e.g. the local magnetization, the local temperature or local acoustic properties exist.

With STM and AFM it is even possible to reach atomic resolution by which one understands the ability to resolve single atoms of the size of the order of a few Å. Thus these techniques allow to investigate atomic arrangements of surfaces. Obviously this atomic resolution is harder to obtain for closed packed metal surfaces than for relatively open semiconductor surfaces. However, the application of the STM to metal surfaces has proven to open exciting new insights. Combined with the possibility to manipulate single atoms on those surfaces, very spectacular images have been produced¹. To interpret these images a profound understanding of the electronic structure of the system in question is needed.

¹E.g. <http://www.almaden.ibm.com/vis/stm/>

Very recently, a new field of solid state physics was established, called magneto-electronics or spin-electronics. It started with the discovery of the giant magneto-resistance (GMR) effect at the Forschungszentrum Jlich. Another effect, similar to the GMR is the tunneling magneto-resistance (TMR) of magnetic tunnel-junctions consisting of metal/nonmetal junctions in which tunneling of spin-polarized electrons occur. This effect might be used in sensors or to store information in non-volatile memory, so called magnetic random access memory (MRAM). The physical principles of the TMR are very similar to those of the spin-polarized STM currently being developed to investigate magnetic nano-structures.

In the work presented here, STM images are calculated from *first principles*. *First principles* means that no experimental input other than the nuclear charges and positions is required. All *first principles* or *ab initio* results are based on the density-functional theory, by far the most successful quantum theory applicable to real materials. The density-functional equations are solved using the full-potential linearized augmented plane-wave (FLAPW) method in film geometry. This method is a very accurate, state-of-the-art approach which allows to obtain the quantities needed to calculate STM images with very high accuracy. All calculations are performed with the FLAPW-program FLEUR, a recent joint development by the group of Prof. R. Podloucky at the University of Vienna and Dr. S. Blgel at the Institut fr Festkrperforschung of the Forschungszentrum Jlich. A short introduction into density-functional theory and into the FLAPW method will be given in the next two chapters.

The fourth chapter will describe the theory used to describe the tunneling process. Bardeen's approach to the tunneling problem is used, together with the additional rather simple approximation of Tersoff and Hamann, in which the tunneling current is described by sample properties only. This simple ansatz, however, has proven to be quite successful in the application to metal and semiconductor surfaces.

In this thesis, I apply this theory to two key issues in the interpretation of atomically resolved STM images: (i) The problem of chemical contrast of multicomponent surfaces. This will be investigated on the example of the $c(2\times 2)\text{MnCu}/\text{Cu}(100)$ ordered surface alloy, discovered recently. I will show that, in opposite to the interpretation of STM images based on the surface relaxation of the structure, most likely not Mn but Cu is imaged. This interpretation can consistently explain previously unexplained experimental data. (ii) The theory is applied to investigate the possibility to image buried interfaces by the STM. It sounds like a contradiction using a surface sensitive tool to detect buried interfaces. However, for the example of a buried $c(2\times 2)\text{MnAg}/\text{Ag}(100)$ two-dimensional alloy, I could show that this alloy layer can

be detected in STM even if it is buried under as much as ten monolayer of Ag. This is truly a surprising result not expected from the conventional interpretation of STM.

These results show that even though the basic principle of the STM is simple, the interpretation of STM images on the atomic scale without additional theoretical calculations may be incorrect and that the theory can open new vistas and stimulate new experiments.

Chapter 2

Density-Functional Theory

In order to calculate properties of the solid state one must in principle solve the Dirac-equation for an enormous number of interacting particles. Since it is not possible to solve this equation analytically for nontrivial systems, one has to find numerical schemes. However, it is rather obvious that even modern numerical techniques for solving differential equations will fail for a many particle system containing more than only a few particles. Therefore, one has to find some method that can simplify the mathematical model of the system.

One of the simplifications used frequently in solid state physics is the Born-Oppenheimer approximation [AM76]. Since the mass of the atomic nuclei is at least three orders of magnitude larger than the mass of the electrons one can keep the nuclei at fixed positions while solving the electron problem. In this approach one neglects any quantum effects which may arise from the dynamics of the nuclei such as the electron-phonon interaction.

Nowadays, the probably most successful and most often used technique to solve the remaining many electron problem is based on the density-functional theory of Hohenberg and Kohn [HK64, JG89].

This chapter will give a brief introduction into the basics of the density-functional theory. Since this is not the main subject of this work, this part will be kept very short. It will not deal in detail with any of the more subtle problems arising from e.g. degenerate ground states or charge densities that are not representable by one particle densities. Further information on those subjects can be found in [Koh83, Lev79, Esc96]. I also will restrict the presentation to the non-magnetic, non-relativistic case.

2.1 The Hohenberg-Kohn theorem

Two theorems are the foundation of density-functional theory which are attributed to Hohenberg and Kohn [HK64] :

1. Theorem: All ground-state properties are functionals of the ground-state density $n(\vec{r})$.

For a system with a non-degenerate ground-state, it immediately follows that the ground-state itself, i.e. the many-particle wave-function of the ground-state, is a functional of the ground-state density. This first theorem determines the basic strategy that can be used to deal with the many electron system of a solid. Not the many-particle wave-function is the quantity which will be determined, but the electron density $n(\vec{r})$. Since this function depends on only three independent spatial coordinates rather than on $O(3^{10^{23}})$, this is a great simplification of the numerical task.

2. Theorem: The ground-state total energy functional is minimal for the correct ground-state density with respect to all densities leading to the correct number of electrons.

This second theorem now gives a minimization principle which can be used to determine the ground-state density. If the form of the total energy functional is known, the ground state density can be determined using this second theorem.

At this point one has to deal with the question how this total energy functional looks like. In a many particle picture the density is given by $n = \langle \Psi | \Psi \rangle$ where Ψ denotes the antisymmetric many-particle wave-function. Assuming that this density can be expressed in terms of one particle eigenfunctions of a system of electrons in some external potential V_{ext} , this energy functional $E[n]$ was expressed by Kohn and Sham [KS65] in the following form

$$E[n] = T[n] + E_{ext}[n] + E_H[n] + E_{xc}[n] \quad (2.1)$$

where $T[n]$ denotes the kinetic energy of a non-interacting electron gas of density n , E_{ext} describes the interaction with the external potential V_{ext} , E_H contains the classical Coulomb interaction, i.e. the Hartree contribution to the energy, and E_{xc} (which is called the exchange-correlation energy) describes all many-body quantum contributions beyond the Hartree-approximation.

The energy of the interaction with the external potential is given by

$$E_{ext} = \int V_{ext}(\vec{r})n(\vec{r})d\vec{r}, \quad (2.2)$$

where V_{ext} describes some external potential, to which the Coulomb potential of the nuclei will be the largest contribution.

The Hartree-term is given by

$$E_H[n] = e^2 \int \int \frac{n(\vec{r})n(\vec{r}')}{|\vec{r} - \vec{r}'|} d\vec{r}d\vec{r}'. \quad (2.3)$$

The exchange-correlation contribution to the total energy functional is unknown for general systems. I will later deal with the question how to approximate this term.

The kinetic energy $T[n]$ is the kinetic energy of N non-interacting electrons:

$$T[n] = \sum_{i=1}^N \langle \Psi_i | -\frac{\hbar^2}{2m} \nabla^2 | \Psi_i \rangle \quad (2.4)$$

The single electron states Ψ_i in this expression have to be chosen to reproduce the density n by the relationship

$$n = \sum_{i=1}^N \langle \Psi_i | \Psi_i \rangle. \quad (2.5)$$

A discussion of the existence of such a decomposition of the charge density into single particle states can be found in [Lev79].

2.2 The Kohn-Sham equation

The question remains how the actual ground-state density is determined. One possible approach is to transform the minimalization problem into a set of differential equations. Similarly to the derivation of the Schrödinger equation from the variational principle of Rayleigh-Ritz (see for example [SW93]), one applies the method of Lagrange multipliers to the problem. Together with the decomposition of the density in terms of single particle wave-functions as described in the previous section, one arrives at a one-particle eigenvalue problem [KS65]:

$$\left\{ -\frac{\hbar^2}{2m} \nabla^2 + V_{ext}(\vec{r}) + e^2 \int \frac{n(\vec{r}')}{|\vec{r} - \vec{r}'|} d\vec{r}' + V_{xc}(\vec{r}) \right\} \Psi_i = \epsilon_i \Psi_i. \quad (2.6)$$

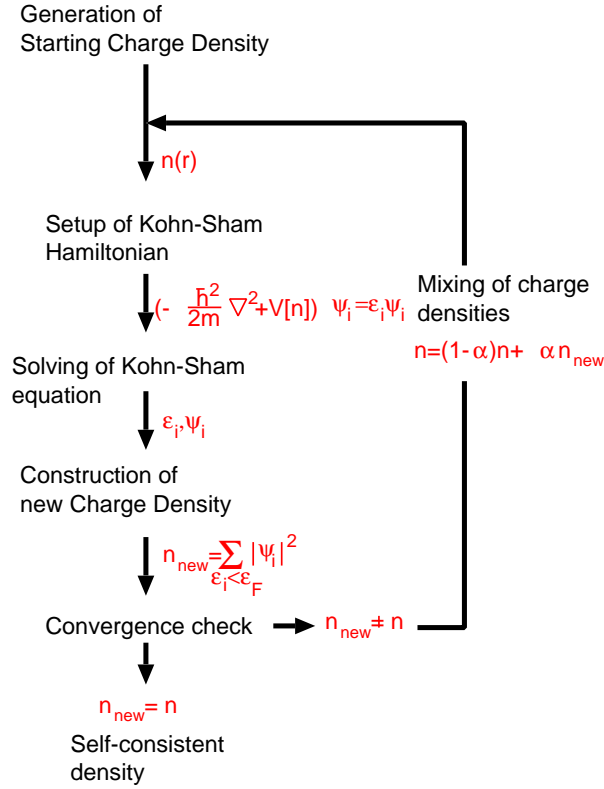


Figure 2.1: The self-consistency iteration process used to solve the Kohn-Sham equations self-consistently.

This equation, which is called the Kohn-Sham equation, has the form of a Schrödinger equation, in which the external potential, the Coulomb interaction and an exchange-correlation potential form an effective potential for some non-interacting particles. This exchange-correlation potential is connected to the exchange-correlation energy functional of the previous section by a functional derivative

$$V_{xc}(\vec{r}) = \frac{\delta E_{xc}[n]}{\delta n(\vec{r})}. \quad (2.7)$$

Thus, the minimization process corresponds to the determination of the solution of Eq. (2.6) with respect to the constraints

$$\int |\Psi_i(\vec{r})|^2 d^3\vec{r} = 1, \quad (2.8)$$

which leads to the introduction of the Lagrange multipliers ϵ_i . Since the potentials in Eq. (2.6) depend on the electron-density, which in turn depends on the one-particle wave-functions Ψ_i by Eq. (2.5) the Kohn-Sham equation has to be solved self-consistently.

This self-consistent solution is obtained in an iteration process as shown in Fig. 2.1.

At this point I would like to discuss the significance of the single particle states Ψ_i and of the corresponding energies ϵ_i . Strictly speaking, these energies do not possess any physical significance. Similarly, the eigenvectors of equation (2.6) do not have any meaning. It is, however, quite common to interpret the single particle energies ϵ_i as excitation energies of electrons and also to use the states Ψ_i as corresponding one-particle wave-functions in this way. It is known [Jan78, Per83] that the Fermi energy of this independent particle system, e.g. the energy ϵ_N of the highest occupied state, is indeed the work function of the system. Furthermore, it is known that for energies ϵ_i which differ substantially from ϵ_N , the energies ϵ_i do not reproduce the excitation energies very well. Especially, in general Koopmann's theorem is not valid for density-functional theory [JG89]. Usually the energies are shifted while their \vec{k} -dependence, i.e. the dispersion of the bands, is described reasonably well. In particular, band-gaps turn out to be generally underestimated. It is a widely used approach to correct these errors by adding an energy-shift to the bands to account for this underestimation. In my calculations corrections of this kind are not necessary, since the tunneling process includes only states near the Fermi-energy. As no band-gap occurs at the Fermi-level in metals, the use of the single particle energies and of the single particle states usually leads to reasonable results for metallic systems.

2.3 The Local Density Approximation

As described so far, density-functional theory contains no approximations. The charge density $n(\vec{r})$ obtained by solving the Kohn-Sham equation (2.6) self-consistently would be the exact ground-state density. However, this solution will only be possible if the exchange-correlation energy E_{xc} is known.

Many ways of approximating this energy have been explored. The most widely used approximation is the Local Density Approximation (LDA) or its spin-dependent version, the Local Spin Density Approximation (LSDA). In this approximation the exchange-correlation energy is chosen to be at every point \vec{r} the exchange-correlation potential of a free electron-gas with a uniform density of $n(\vec{r})$. The exchange-correlation energy therefore is given by

$$E_{xc}[n(\vec{r})] = \int n(\vec{r})\epsilon_{xc}(n(\vec{r})) d^3r, \quad (2.9)$$

where ϵ_{xc} is no longer a functional of the density but just a function. This approximation is therefore exact in the limit of a free electron-gas with uniform density, and one would expect that the approximation also performs reasonably well for a

slowly varying density $n(\vec{r})$. Nevertheless, experience has shown that this approximation also reproduces the main properties of metals quite accurately. Therefore, this approximation can be used to perform calculations on metals with good results. In practice, expression (2.7) is evaluated using an explicit parameterization of $\epsilon_{xc}(n)$. These parameterizations can be obtained by fits to quantum-mechanical many-body calculations. Some parameterizations that are frequently used are the parameterization of v. Barth and Hedin [vBH72] or of Moruzzi, Janak, and Williams [MJW78], which are based on the random phase approximation or the parameterizations of Vosko, Wilk, and Nusair [VWN80] or of Perdew and Zunger [PZ81], which are based on Quantum-Monte-Carlo simulations. In the work presented here the parameterization of Vosko, Wilk and Nusair has been used.

Several attempts have been made to improve this approximation, of which the Generalized Gradient Approximation (GGA) is the most promising at present. This GGA approximation reproduces many experimental quantities with greater accuracy than the LDA. However, in a GGA calculation performed to test whether the GGA is important for the results presented here, it was seen that the changes in the exchange-correlation potential do not strongly effect the STM quantities of the systems investigated here. Therefore, the calculations presented in this work were carried out using the LDA. In tests, applying the GGA to STM calculations of the systems discussed here, no significant difference between the LDA and GGA results were found.

Chapter 3

The FLAPW-Method

In the previous chapter the basic framework of density-functional theory was described. Now, in this chapter implementational details of the **F**ull-potential **L**inearized **A**ugmented-**P**lane-**W**aves (FLAPW) method will be presented with some special emphasis on the calculation of the electronic structure in the vacuum which is of fundamental interest when it comes to the interpretation of STM and STS images.

A detailed review of the method can be found in the book by Singh [Sin94] and in [Kur97, Pen96].

One approach to solve a differential equation like the Kohn-Sham equation consists of the introduction of a basis set into function-space and of the transformation of the differential-equation into a matrix-eigenvalue problem. The wave-function expanded into these basis-functions ϕ_i is written as

$$\Psi_{\vec{k},\nu} = \sum_i c_{\vec{k},\nu}^i \phi_i, \quad (3.1)$$

where \vec{k} and ν denote the quantum numbers labeling the wave-function, i.e. the Bloch-wave-vector \vec{k} and the band index ν in the case of a crystal, and the index i will loop over all basis-functions ϕ_i . Many methods use plane-waves as basis-functions

$$\phi_{\vec{G}}(\vec{r}) = \frac{1}{\sqrt{V}} e^{i\vec{G}\vec{r}}, \quad (3.2)$$

where the prefactor ensures the normalisation over a unit cell of volume V . In those methods the index i labeling the basis-functions will correspond to the wave-vector \vec{G} of the plane-wave, which will be chosen from the reciprocal lattice to ensure translational symmetry. The \vec{k} -dependence of the Bloch-wave will then be included into the Hamiltonian. Plane-waves are orthogonal and normalized. Hence,

the Kohn-Sham equation can be written as a matrix eigenvalue problem after the introduction of the basis set

$$\left(H_{\vec{k}}^{\vec{G}\vec{G}'} - \epsilon_{\vec{k},\nu} \right) c_{\vec{k},\nu}^{\vec{G}'} = 0, \quad (3.3)$$

where $H_{\vec{k}}^{\vec{G}\vec{G}'} = \langle \phi_{\vec{G}} | H_{\vec{k}} | \phi_{\vec{G}'} \rangle$ denote the matrix elements of the Hamiltonian of the Kohn-Sham equation.

This transformation of the differential equation into a matrix eigenvalue problem shows very clearly how the numerical approximations come in. Any basis set in function-space would be infinitely large, giving rise to an infinitely large matrix. Such a matrix cannot be diagonalized in general and therefore one has to introduce a cutoff and restrict the number of basis-functions. It is very obvious that both the number of basis-functions used and the actual form of the basis-functions is of importance when it comes to the accuracy of the solution. If one could choose the eigenfunctions of the matrix as basis-functions, for example, one would obtain correct results for the eigenvalues and eigenvectors described by these functions.

These general considerations make it rather obvious that pure plane-waves are a bad choice for the basis-functions. The wave-functions oscillate strongly near the positions of the atoms and so a huge number of plane-waves would be necessary to describe this behavior. This large basis set would lead to a huge matrix problem which could not be handled. Therefore, two approaches are frequently used. Either the potential is modified near the nuclei to change this oscillatory behavior of the wave-functions which makes them accessible to an approximation by plane-waves. This idea, which leads to the pseudo-potential methods, will not be applied in this work.

The second successful idea is to modify the basis-functions. Not simple plane-waves are used but a set of functions is constructed which is better adapted to describe the wave-functions. This idea leads to the group of **A**ugmented **P**lane-**W**aves (APW) based methods of which one very accurate realization is used in this work.

3.1 The FLAPW Basis set inside the crystal

I will now describe the full-potential linearized augmented-plane-waves method as implemented in the FLEUR-code used for the calculations presented here. In this method the space is divided into several regions. To treat bulk systems the unit-cell is divided into two regions: Spheres around the atom positions, the so-called muffin-

tin spheres and the region between these muffin-tin spheres, the so called interstitial region (Fig. 3.1).

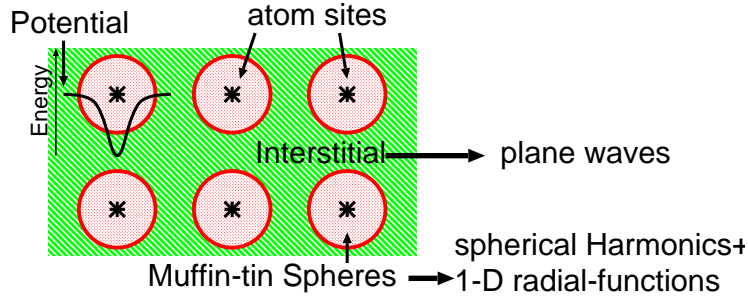


Figure 3.1: The APW setup a unit-cell. The muffin-tin spheres around the atoms and the interstitial region are shown

In the muffin-tin spheres the potential is dominated by the large Coulomb potential of the nucleus

$$V_{nucl} \propto -\frac{Ze}{r}, \quad (3.4)$$

where r denotes the distance from the nucleus and Z is the atomic number. Thus, the differential equation in this region looks very much like an atomic spherically symmetric potential and one would expect the wave-functions also to be similar to atomic-wave-functions. Hence, the goal of using functions in the basis which describe the physical eigenfunctions with great accuracy can be reached by using a product of spherical harmonics $Y_{lm}(\hat{r})$, where \hat{r} is the direction unit-vector, and radial wave-functions $u_l(r)$ which solve the spherically symmetric problem. As known from any quantum-mechanics textbook (see for example [LLP79]), the radial part $u_l(r)$ of the Schrödinger equation of a particle in a spherically symmetric potential is the solution of the following one-dimensional differential equation

$$\left\{ -\frac{\hbar^2}{2m} \frac{\partial^2}{\partial r^2} + \frac{\hbar^2}{2m} \frac{l(l+1)}{r^2} + V_{eff}(r) - \epsilon_l \right\} r u_l(r) = 0. \quad (3.5)$$

From this differential equation the functions $u_l(\epsilon_l, r)$ are determined using an energy-parameter ϵ_l and the spherically averaged potential $V_{eff}(r)$. The functions $u_l(\epsilon_l, r)$ will only approximate the radial part of the correct unknown wave-function reasonably well, if the energies ϵ_l correspond to the band energies $\epsilon_{\vec{k}, \nu}$ of the problem. Since these energies are not known in advance, this imposes a significant additional problem. This is one of the central problems of the augmented plane-waves method, which uses the approach presented so far to construct the basis-functions. Since the band-energies are not known, these energies have to be determined iteratively in each step of the self-consistence cycle used to find the solution of the Kohn-Sham

equation. This produces a significant additional problem.

In the Linearized Augmented Plane-Waves method LAPW, which was suggested by Andersen, Arbman, and Koelling [And75, KA75], this problem is overcome by introducing a linearization of this energy dependence of the $u_l(\epsilon_l)$ around the energy parameters ϵ_l

$$u_l(\epsilon) = u_l(\epsilon_l) + \dot{u}_l(\epsilon_l)(\epsilon - \epsilon_l), \quad \dot{u}_l = \frac{\partial u_l}{\partial \epsilon}. \quad (3.6)$$

In the interstitial region on the other hand the potential is much flatter than near the nuclei. Therefore plane-waves should form a rather good basis set in this region.

Concluding, the basis-function in the interstitial region and in the muffin-tin spheres have the following form

$$\phi_{\vec{G}}(\vec{k}, \vec{r}) = \begin{cases} e^{i(\vec{k}+\vec{G})\vec{r}} & , \text{ interstitial region} \\ \sum_{lm} \left[A_{lm}^{\alpha\vec{G}}(\vec{k}) u_l^\alpha(r_\alpha) Y_{lm}(\hat{r}_\alpha) + B_{lm}^{\alpha\vec{G}}(\vec{k}) \dot{u}_l^\alpha(r_\alpha) Y_{lm}(\hat{r}_\alpha) \right] & , \alpha^{th} \text{ muffin-tin} \end{cases} \quad (3.7)$$

where the basis-functions are labeled by the vectors \vec{G} from reciprocal space. In this expression the normalization has been omitted for simplicity and the index α of the coordinates r and \hat{r} should indicate that these coordinates are relative to the center of the α^{th} muffin-tin sphere. The coefficients $A_{lm}^{\alpha\vec{G}}$ and $B_{lm}^{\alpha\vec{G}}$ are determined by the condition that each of the basis-function and its first radial derivative are continuous across the muffin-tin boundary.

When one uses these basis-functions to expand the eigenfunctions of the Kohn-Sham equation one notices that the basis-functions are not orthogonal with respect to each other. Therefore, the Kohn-Sham problem is not transferred into a simple matrix eigenvalue problem, but into a generalized eigenvalue problem. In this problem an additional so-called overlap matrix $S_{\vec{k}}^{\vec{G}\vec{G}'} = \int \phi_{\vec{G}}(\vec{k}, \vec{r})^* \phi_{\vec{G}'}(\vec{k}, \vec{r}) d\vec{r}$ appears. This generalized eigenvalue problem can be written in the form

$$\left(H_{\vec{k}}^{\vec{G}\vec{G}'} - \epsilon_{\vec{k},\nu} S_{\vec{k}}^{\vec{G}\vec{G}'} \right) c_{\vec{k},\nu}^{\vec{G}'} = 0, \quad (3.8)$$

where $H_{\vec{k}}^{\vec{G}\vec{G}'}$ denotes the Hamilton-matrix of the Kohn-Sham equation.

3.2 A full-potential method

Bandstructure methods apply a shape restriction to the potential. The true potential is approximated by a spherical potential inside the muffin-tin spheres and a constant

potential in the interstitial region between the spheres.

$$V(\vec{r}) = \begin{cases} V_I = \text{const} & , \text{ interstitial region} \\ V_{MT}(|\vec{r}|) & , \text{ muffin - tins} \end{cases} \quad (3.9)$$

This approximation simplifies the computer program, speeds up the calculation and leads to reasonable results for closed packed systems, such as cubic metals. For open systems with low symmetry or surfaces it is too crude when it comes to accuracy.

In the FLAPW-method [Ham79, WKWF81], as implemented in the FLEUR-code, no restriction regarding the shape of the potential or the charge density is made. Inside the muffin-tin spheres the potential and the charge density are expanded into lattice symmetry adapted spherical harmonics $K_\nu^\alpha(\hat{r})$. In the interstitial region these quantities are expanded into symmetrized plane-waves, the so called star-functions $\Phi_s(\vec{r})$. (For more details on star-functions see next chapter.) Thus the potential and analogously the charge density are written as

$$V(\vec{r}) = \begin{cases} \sum_\nu V_\nu^\alpha(r) K_\nu^\alpha(\hat{r}) & , \alpha^{th} \text{ muffin - tin} \\ \sum_s V_s \Phi_s(\vec{r}) & , \text{ interstitial region} \end{cases} \quad (3.10)$$

This full-potential method is of great accuracy and overcomes previous limitations of the LAPW-method at the expense of a higher computational effort in the setup of the Hamiltonian and the construction of the charge density.

3.3 FLAPW in film geometry

The FLAPW method as described so far can be used to calculate bulk properties. If one wants to calculate surface properties, two questions arise: (i) how to deal with the breaking of the three-dimensional translational symmetry normal to the surface and (ii) how to deal with the vacuum region. A first idea would be to extend the interstitial region into the vacuum. Since codes in solid state physics normally exploit the three-dimensional translational symmetry of a crystal, this leads to some super-cell approach in which a slab of bulk-material is repeated with some extended interstitial region in between, mimicking the vacuum (Fig. 3.2a)). In this idea a three-dimensional translational symmetry will still be used. This approach obviously has some disadvantages. First, in this approach the periodicity in z-direction is artificial and one has to be very careful to make the separation of the slabs sufficiently large in order to avoid the interaction of slabs across the vacuum.

Secondly, and this is quite important for the calculation of STM images, the basis-functions in the vacuum region are numerically not well adapted to describe the wave-function sufficiently accurate. The wave-function will decay exponentially at large distance from the surface. This behavior cannot be approximated very well with plane-waves as used in the interstitial region. To calculate STM and STS properties a different approach is more suitable.

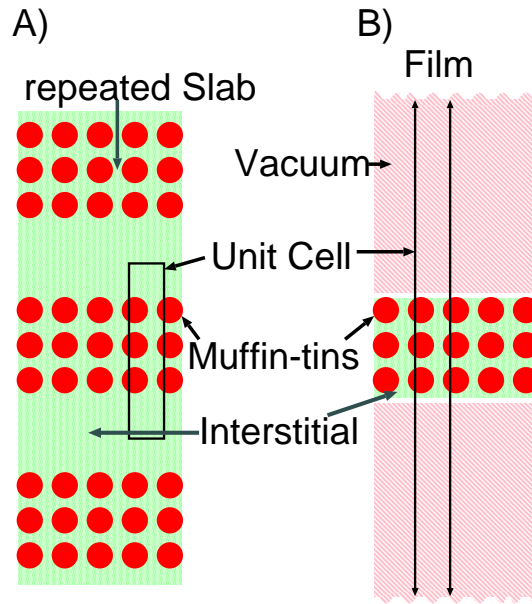


Figure 3.2: a) shows a unit-cell as used in a super-cell geometry. The slabs are repeated in z -direction separated by an interstitial region. b) shows the unit-cell as used in the FLEUR-code. The vacuum-regions are not repeated and the basis-functions are modified within the vacuum to describe the decay of the wave-functions

The FLEUR-code used in this work has the option to be used as a bulk code as well as a film code [KPF97]. This means that two vacuum regions at both sides of a finite film are introduced. These vacuum regions are semi-infinite with correct boundary conditions at both plus and minus infinity. Thus the three-dimensional symmetry is broken and one uses a truly two-dimensional translational symmetry. The latter means that only two-dimensional Bloch-vectors \vec{k}_{\parallel} , which are chosen from the two-dimensional surface Brillouin zone, are used.

In this approach the LAPW basis set as described so far is modified and extended. The vacuum forms a third region in space (Fig. 3.2b)) with a different representation of the potential, the charge density and the wave-functions, i.e. another form of the basis-functions is chosen in the vacuum region. These basis-functions in the vacuum can be written as a product of a z -dependent function $\tilde{u}(z)$ and an r_{\parallel} -dependent part. Since the vacuum potential inhibits the periodicity of the surface unit-cell

the r_{\parallel} -dependent part simply consists of two-dimensional plane-waves parallel to the surface. The z -dependent part $\tilde{u}_{\vec{G}_{\parallel}\vec{k}_{\parallel}}(z)$ has to describe the decay of the wave-functions into the vacuum. Similarly to the muffin-tin radial functions $u(r)$ which are obtained by solving a radial one-dimensional Schrödinger equation, the z -dependent functions $\tilde{u}_{\vec{G}_{\parallel}\vec{k}_{\parallel}}(z)$ are obtained from the solution of the one-dimensional equation

$$\left\{ -\frac{\hbar^2}{2m} \frac{d^2}{dz^2} + V_{vac}(z) - \epsilon_{vac} + \frac{\hbar^2}{2m} (\vec{G}_{\parallel} + \vec{k}_{\parallel})^2 \right\} \tilde{u}_{\vec{G}_{\parallel}\vec{k}_{\parallel}}(z) = 0 \quad (3.11)$$

where V_{vac} is the planar averaged vacuum potential of the system. Similar to the energy-parameters used in the differential equation for the basis-functions inside the muffin-tin, the energy-parameter ϵ_{vac} should be chosen to be the energy of the band. Since this energy is not known in advance, the same linearization strategy as for the functions $u(r)$ is used. ϵ_{vac} is used as an energy-parameter in the vacuum and the function $\tilde{u}(\epsilon_{vac}, z)$ is linearized around ϵ_{vac} :

$$\tilde{u}(\epsilon, z) \sim \tilde{u}(\epsilon_{vac}, z) + \dot{\tilde{u}}(\epsilon_{vac}, z) \times \epsilon, \quad (3.12)$$

where $\dot{\tilde{u}} = \frac{\partial \tilde{u}}{\partial \epsilon}$. $\dot{\tilde{u}}$ is calculated as the solution of a differential equation derived by differentiating Eq. (3.11)

$$\left\{ -\frac{\hbar^2}{2m} \frac{d^2}{dz^2} + V_{vac}(z) - \epsilon_{vac} + \frac{\hbar^2}{2m} (\vec{G}_{\parallel} + \vec{k}_{\parallel})^2 \right\} \dot{\tilde{u}}_{\vec{G}_{\parallel}\vec{k}_{\parallel}}(z) = \tilde{u}_{\vec{G}_{\parallel}\vec{k}_{\parallel}}(z). \quad (3.13)$$

The extension of equation (3.7) leads to the basis-functions in the FLEUR-code which have the following form:

$$\phi_{\vec{G}_{\parallel}G_{\perp}}(\vec{k}_{\parallel}, \vec{r}) = \begin{cases} e^{i(\vec{k}_{\parallel} + \vec{G}_{\parallel})\vec{r}_{\parallel}} \times e^{iG_{\perp}z} & , \text{ interstitial} \\ \sum_{lm} \left[A_{lm}^{\alpha\vec{G}}(\vec{k}_{\parallel}) u_l^{\alpha}(r_{\alpha}) Y_{lm}(\hat{r}_{\alpha}) + B_{lm}^{\alpha\vec{G}}(\vec{k}_{\parallel}) \dot{u}_l^{\alpha}(r_{\alpha}) Y_{lm}(\hat{r}_{\alpha}) \right] & , \alpha^{th} \text{ muffin - tin} \\ \left[a^{\vec{G}_{\parallel}}(\vec{k}_{\parallel}) \tilde{u}_{\vec{G}_{\parallel}\vec{k}_{\parallel}}(z) + b^{\vec{G}_{\parallel}}(\vec{k}_{\parallel}) \dot{\tilde{u}}_{\vec{G}_{\parallel}\vec{k}_{\parallel}}(z) \right] e^{i(\vec{k}_{\parallel} + \vec{G}_{\parallel})\vec{r}_{\parallel}} & , \text{ vacuum} \end{cases} \quad (3.14)$$

The coefficients $a^{\vec{G}_{\parallel}}(\vec{k}_{\parallel})$ and $b^{\vec{G}_{\parallel}}(\vec{k}_{\parallel})$ are determined to let the function and its first derivative be continuous across the vacuum border. Because of the breakdown of three-dimensional translations symmetry, the wave-vectors of the interstitial are replaced by a two-dimensional wave-vector $\vec{k}_{\parallel} + \vec{G}_{\parallel}$ chosen from the surface Brillouin zone and the two-dimensional reciprocal space and a z -dependent plane-wave with wave-number G_{\perp} .

Chapter 4

Theory of the STM

4.1 The Scanning Tunneling Microscope

Since its invention by Binnig and Rohrer in 1982 [GBW82a, GBW82b] the Scanning Tunneling Microscope (STM) has become a frequently used tool in surface science. Its setup basically consists of a sharp metal tip which in the ideal case has only a single apex atom, i.e. it is mono-atomically sharp (Fig. 4.1). Using piezo-crystals this tip can be moved in all three dimensions on a 0.01 \AA scale. If the tip is moved

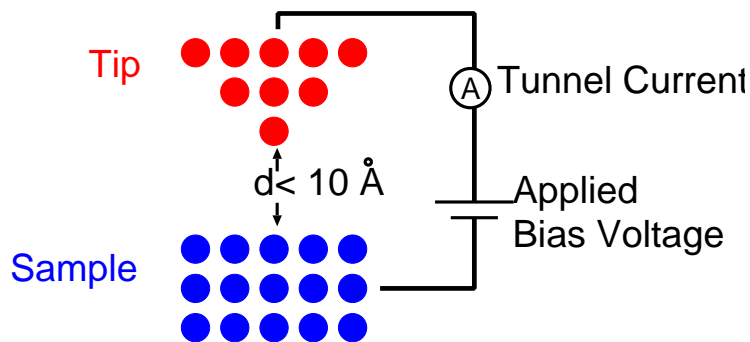


Figure 4.1: Setup of an STM.

close to the sample (up to a distance in the range of a couple of \AA only) electrons can tunnel through the vacuum barrier from the tip into the surface and vice versa. In the case of a conductive sample material and with an applied bias voltage this effect can lead to a current of electrons tunneling between the systems. This current is the basic quantity measured in an STM experiment. Two different modes of operation of the STM will be discussed in this work: First, one can scan the tip position over the surface and obtain a two-dimensional map of the tunneling current. In practice, this mode is normally realized by keeping the current fixed and by varying

the tip-sample distance d accordingly (Fig. 4.2). This so called constant-current mode ensures that the tip does not touch the surface while being scanned over the sample. The experimental quantity measured in the constant-current mode is no longer the tunneling current but the corrugation of the tip.

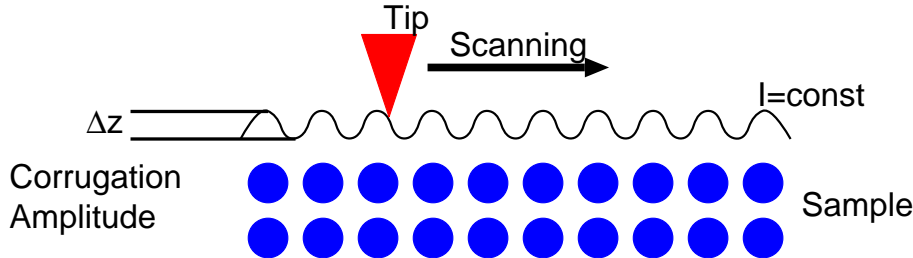


Figure 4.2: Constant-current mode. The tip is scanned along the line of constant tunneling current. This leads to a corrugation of the tip position with a corrugation amplitude Δz .

In the analysis presented in this work I will frequently refer to the corrugation amplitude (Fig. 4.2). This quantity is defined as the difference between the largest and smallest tip-sample distance in a constant current experiment. Due to the exponential dependence of the tunneling current on the width of the barrier, i.e. of the tip-sample distance, this experimental setup allows a high resolution vertical to the surface. Combined with the high accuracy of the positioning of the tip parallel to the surface, images with an extremely high resolution can be obtained. Steps and islands can be mapped easily and if the experimental setup is stable enough one can reach atomic resolution with this method. In these STM images with atomic resolution, single ad-atoms on a surface and single defects can be observed. However, as I will show in this work, the interpretation of atomically resolved STM images is not always simple.

The second main mode of operation of an STM is the spectroscopic mode in which the applied bias voltage is varied and the change in the tunneling current resulting from this change is measured. This mode allows a local investigation of the electronic structure.

4.2 Basic theory of tunneling

The tunneling process is a complicated many electron problem. A proper theoretical approach to this problem would describe the tunneling of an electron by the probability $P_{i,f}$ of the system changing its state from some initial multi-electron state Ψ_i

into a final multi-electron state Ψ_f . In this picture, the states Ψ_i and Ψ_f describe two states which differ with respect to their charge distribution in the sample and the tip

$$\begin{aligned}\Delta q &= \int_{Tip} \langle \Psi_i | \hat{Q} | \Psi_i \rangle - \langle \Psi_f | \hat{Q} | \Psi_f \rangle \\ &= \int_{Sample} \langle \Psi_f | \hat{Q} | \Psi_f \rangle - \langle \Psi_i | \hat{Q} | \Psi_i \rangle\end{aligned}\quad (4.1)$$

where \hat{Q} is the electron-charge density operator. It is known from basic quantum-mechanics that the probability $P_{i,f}$ is given by $P_{i,f} = | \langle \Psi_i | \Psi_f \rangle |^2$. Thus, this approach makes it necessary to calculate the many particle time-dependent wave-functions of the entire system. This is a very difficult task which cannot be solved in general. Therefore, one has to make some approximations.

As a first approximation a single electron approach to the tunneling problem will be used. This is already a very important simplification since it allows to use single particle wave-functions obtained from the Kohn-Sham equation as described in the previous chapter. Of course, a description in terms of single particle wave-functions implies that one cannot describe effects which will occur by multi-electron tunneling. These effects include electron-electron scattering effects or effects occurring from the potential variation in the barrier region if several electrons tunnel at the same time. However, since the tunneling current in STM experiments is very low in general one will expect these effects to be of minor importance only. As described above, the tunneling process is due to transitions in which states with different charge localization are involved. In the single particle picture this could be understood as transitions from single particle states which are localized on one side of the vacuum barrier into states which are localized on the other side. This directly gives some motivation to describe the single particle state ψ in terms of eigenfunctions of two separate systems.

4.3 The Bardeen approach to tunneling

The following description of the tunneling process is based on Bardeen's approach to tunneling which first applies time dependent perturbation theory to the problem and then makes some additional approximations. The system is thought to consist of two independent systems: one for the tip and one for the sample.

This total separation of the tip and the sample system leads to two independent Schrödinger equations for the two systems

$$(T + U_S)\psi_S = \epsilon_S\psi_S$$

$$(T + U_T)\psi_T = \epsilon_T\psi_T \quad (4.2)$$

where T denotes the operator of the kinetic energy of a single electron and U_T and U_S are the potentials of the tip and sample system respectively. The single particle wave-function of the entire system is determined by the total Hamiltonian $H = T + U_S + U_T$.

Now one can apply time dependent perturbation theory to describe the tunneling of an electron from the sample to the tip. The case of an electron tunneling from the tip to the sample may be treated completely analogously. The initial state of the tunneling process is localized in the sample. So there will be no influence from the tip. Therefore, there exists an eigenstate ψ_S^μ of the sample system with $|\psi(t \rightarrow -\infty)\rangle = |\psi_S^\mu\rangle$. The time dependence of the state $|\Psi(t)\rangle$ is governed by the Hamiltonian of the whole system.

$$i\hbar\frac{\partial}{\partial t}|\psi(t)\rangle = H|\psi(t)\rangle. \quad (4.3)$$

The tunneling probability is given by the overlap of this time-dependent wave-function with a tip wave-function $|\psi_T^\nu\rangle$. Multiplying Eq. (4.3) from the left with $|\psi_T^\nu\rangle$ leads to

$$\langle\psi_T^\nu|\left(i\hbar\frac{\partial}{\partial t}|\psi(t)\rangle\right) = \langle\psi_T^\nu|H|\psi(t)\rangle. \quad (4.4)$$

Using the Schrödinger equation for the tip state one obtains

$$\begin{aligned} i\hbar\frac{\partial}{\partial t}\langle\psi_T^\nu|\psi\rangle &= \langle\psi_T^\nu|H|\psi\rangle - \langle\psi_T^\nu|H_T|\psi\rangle \\ &= \langle\psi_T^\nu|U_S|\psi\rangle \end{aligned} \quad (4.5)$$

Substituting $|\psi(t \rightarrow -\infty)\rangle = |\psi_S^\mu\rangle$ for $|\psi\rangle$ at the right hand side of Eq. (4.5) leads to first order perturbation theory

$$i\hbar\frac{\partial}{\partial t}\langle\psi_T^\nu|\psi\rangle = \langle\psi_T^\nu|U_S|\psi_S^\mu\rangle. \quad (4.6)$$

Even though this equation looks familiar one has to emphasize that this is not a result obtained by standard time-dependent perturbation theory. The states $|\psi_S\rangle$ and $|\psi_T\rangle$ are eigenstates of the Hamiltonians H_S and H_T respectively. Therefore, they do not form a complete orthogonal basis of the eigenspace of the total Hamiltonian $H = T + U_S + U_T$ and the matrix elements at the left side of Eq. (4.6) are not sufficient to determine the total time dependence of $|\psi\rangle$. This is a basic weakness of Bardeen's approach. However many applications [HBP⁺98, HAB⁺99, VSB⁺97, LYB⁺99] of this formalism have shown that Bardeen's approximation produces re-

liable results for systems which are well separated, i.e. systems where the overlap of the two wave-functions ψ_T and ψ_S is small.

Since the potential U_S is not small in the sample region, the question arises whether one is allowed to use perturbation theory at all. However, it can be seen from Eq. (4.6) that the quantity which in fact determines the strength of the perturbation of the initial state is $\langle \psi_T | U_S | \psi_S \rangle$. Since the final wave-function $|\psi_T\rangle$ is localized in the tip region in which the sample potential U_S is very weak this perturbation might still be regarded as a small perturbation and thus time depended perturbation will lead to reasonable results.

By separating the time-dependence of the states $|\psi_S^\mu\rangle = e^{i\epsilon_\mu t} |\Psi_S^\mu\rangle$ and $|\psi_T^\nu\rangle = e^{i\epsilon_\nu t} |\Psi_T^\nu\rangle$, integrating Eq. (4.6) and performing the limit $t \rightarrow \infty$, one obtains an expression for the tunneling-probability per time interval

$$P_{\mu\nu}^{ST} = \lim_{t \rightarrow \infty} \frac{1}{t} \frac{1}{\hbar^2} \int_0^t | \langle \psi_T^\nu | U_S | \psi_S^\mu \rangle |^2 \quad (4.7)$$

$$= \lim_{t \rightarrow \infty} \frac{4}{\hbar} \frac{\sin^2 \left(\frac{\epsilon_\nu - \epsilon_\mu}{2\hbar} t \right)}{(\epsilon_\nu - \epsilon_\mu)^2 t} |M_{\mu\nu}^{ST}|^2, \quad (4.8)$$

where the matrix element $M_{\mu\nu}^{ST}$ is given by the stationary-state matrix element of the potential

$$M_{\mu\nu}^{ST} = \langle \Psi_T^\nu | U_S | \Psi_S^\mu \rangle. \quad (4.9)$$

Assuming a continuous range of energy levels ϵ_μ (or ϵ_ν) the limit of Eq. (4.8) can be evaluated directly [Sch93]. One obtains

$$P_{\mu\nu}^{ST} = \frac{2\pi}{\hbar} \delta(\epsilon_\nu - \epsilon_\mu) |M_{\mu\nu}^{ST}|^2. \quad (4.10)$$

This result is similar to the well known 'Golden Rule' Fermi obtained for standard time-dependent perturbation theory. It describes elastic tunneling from a sample state with energy ϵ_μ into a tip state with energy $\epsilon_\nu = \epsilon_\mu$ only. Formally this condition is taken care of by the δ -function in Eq. (4.10).

To evaluate this matrix element Bardeen introduced an additional approximation. He assumed the potential U_S to be zero in the tip region of space. Similar the tip potential should be zero in the sample region. More formal he introduced a separation surface S which separates the regions in which the two potentials differ from zero. This can be written down by the condition $U_S U_T = 0$ for any point in space. Figure 4.3 shows the setup as used in this additional approximation.

Of course, this approximation will become better if the potentials U_S and U_T are

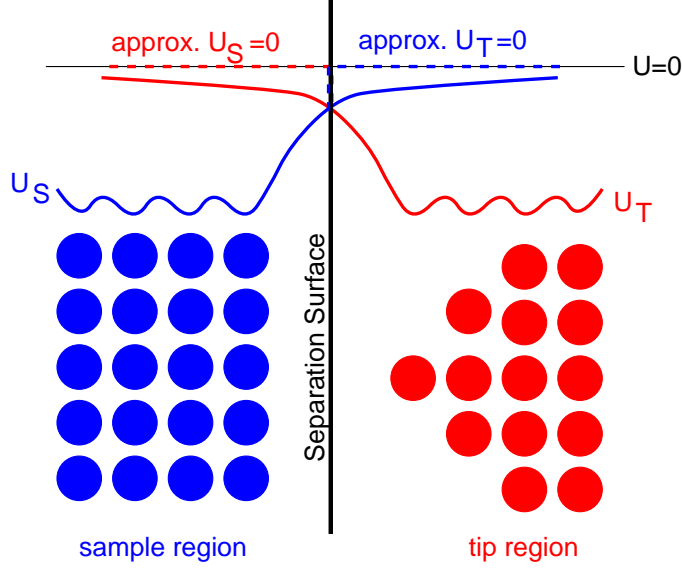


Figure 4.3: Setup used in the Bardeen approach to tunneling. The space is divided into a tip and a sample region separated by a Separation Surface in between. The tip (sample) potential U_T (U_S) is then assumed to be zero in the sample (tip) region.

reasonably small at and beyond the separation surface. This will be the case if the separation surface is located far out in the vacuum. Therefore one will expect that Bardeen's approximation is valid for tunneling processes through a wide barrier i.e. at large tip-sample distances while the results of this approach will become invalid for very small tip-sample distances.

Using the Schrödinger equation for the sample wave-function and having in mind that the potential U_S is zero in the tip-region one can now rewrite the matrix element as an integral over the sample region only

$$M_{\mu\nu}^{ST} = \int_{sample} \Psi_T^\nu(\vec{r})^* \left(\epsilon_\mu + \frac{\hbar^2}{2m} \vec{\nabla}^2 \right) \Psi_S^\mu(\vec{r}) dV \quad (4.11)$$

which can be written in a more symmetric form

$$\begin{aligned} M_{\mu\nu}^{ST} &= \int_{sample} \left\{ \Psi_T^\nu(\vec{r})^* \epsilon_\nu \Psi_S^\mu(\vec{r}) + \Psi_T^\nu(\vec{r})^* \frac{\hbar^2}{2m} \vec{\nabla}^2 \Psi_S^\mu(\vec{r}) \right\} dV \\ &= \int_{sample} \left\{ \Psi_T^\nu(\vec{r})^* \overleftarrow{(T + U_T)} \Psi_S^\mu(\vec{r}) + \Psi_T^\nu(\vec{r})^* \frac{\hbar^2}{2m} \vec{\nabla}^2 \Psi_S^\mu(\vec{r}) \right\} dV \\ &= -\frac{\hbar^2}{2m} \int_{sample} \left\{ \Psi_S^\mu(\vec{r}) \vec{\nabla}^2 \Psi_T^\nu(\vec{r})^* - \Psi_T^\nu(\vec{r})^* \vec{\nabla}^2 \Psi_S^\mu(\vec{r}) \right\} dV \end{aligned} \quad (4.12)$$

In these transformations in the first step the eigenvalue ϵ_μ was substituted by ϵ_ν because energy conservation requires the calculation of matrix elements with $\epsilon_\mu = \epsilon_\nu$ only. In the second step the Schrödinger equation for the tip-state was used (the arrow indicates the wave-function the operators act on). The integration area is the

sample region. Since the potential U_T is assumed to be zero in this region, it was dropped in the last step. Using Green's theorem and the boundary condition that the tip wave-function is zero at infinite distance from the tip this integral can be transformed into an integral over the separation surface

$$M_{\mu\nu}^{ST} = -\frac{\hbar^2}{2m} \int_{surface} \left(\Psi_S^\mu(\vec{r}) \vec{\nabla} \Psi_T^\nu(\vec{r})^* - \Psi_T^\nu(\vec{r})^* \vec{\nabla} \Psi_S^\mu(\vec{r}) \right) dS. \quad (4.13)$$

4.4 The tunneling current

So far only an expression for the probability of the transition of an electron from a sample state into a tip state was obtained. Slightly modifying Eq. (4.10) this probability can be written as

$$P_{\mu\nu}^{ST} = \frac{2\pi}{\hbar} \delta(\epsilon_\mu^S - \epsilon_\nu^T - eV) |M_{\mu\nu}^{ST}|^2, \quad (4.14)$$

where the additional term eV is introduced to account for the bias voltage V applied between the tip and the sample. To calculate the tunneling current one has to sum over all different possible tip and sample states and one has to keep in mind that the electrons might tunnel from the tip into the sample as well as from the sample into the tip. The total current therefore is given by

$$\begin{aligned} I &= I^{S \rightarrow T} - I^{T \rightarrow S} \\ &= 2e \sum_{\mu\nu} f(\epsilon_\mu) (1 - f(\epsilon_\nu + eV)) P_{\mu\nu}^{ST} - 2e \sum_{\mu\nu} (1 - f(\epsilon_\mu)) f(\epsilon_\nu + eV) P_{\nu\mu}^{TS} \\ &= 2e \sum_{\mu\nu} (f(\epsilon_\mu) - f(\epsilon_\nu + eV)) P_{\mu\nu}^{ST} \end{aligned} \quad (4.15)$$

where $f(\epsilon)$ denotes the Fermi-distribution function which is introduced to ensure that only tunneling from occupied to unoccupied states can occur. The factor 2 is introduced to account for the two spin channels. In Eq. (4.15) the symmetry of the tunneling probability $P_{\mu\nu}^{ST} = P_{\nu\mu}^{TS}$ which can easily be deduced from Eq. (4.13) was used. The sum in Eq. (4.15) has to be performed over all tip states labeled by ν and all sample states labeled by μ . To evaluate the current these sums have to be calculated and therefore the matrix-elements $M_{\mu\nu}^{ST}$ have to be evaluated. It will be shown how the matrix elements can be calculated analytically when additional assumptions regarding the tip orbitals are made.

4.5 Tersoff-Hamann's model

The task of calculating Bardeen's matrix element $M_{\mu\nu}^{ST}$ from *ab initio* results can be extremely simplified if one makes some assumptions regarding the tip. This scheme was suggested by Tersoff and Hamann [TH83] and is probably the approach most widely used in the interpretation of STM images (see also [Hei97]). Tersoff and Hamann suggested the replacement of the unknown electronic structure of the tip by a simple model system. In this system the wave-function of the outermost tip atom is assumed to be an atomic *s*-wave-function. Since the tunneling current depends on the overlap of the wave-functions of the tip and the sample as one can see from Eq. (4.13) and since the wave-function decays exponentially into the vacuum only the orbitals localized at this outermost tip atom will be of importance for the tunneling process. However the assumption that these orbitals are *s*-wave-functions is of course questionable. I will come back to this point later.

Assuming that the tip wave-function ψ_ν^T has the following form

$$\Psi_\nu^T(\vec{r} - \vec{r}_0) = \frac{C}{\kappa_\nu |\vec{r} - \vec{r}_0|} \exp(-\kappa_\nu |\vec{r} - \vec{r}_0|) \quad (4.16)$$

which is the general form of an atomic *s*-orbital with a vacuum-decay constant of κ_ν . This function can be related to the Green's function of the vacuum Schrödinger equation which is defined by

$$(\nabla^2 - \kappa_\nu^2) G_\nu(\vec{r} - \vec{r}_0) = \delta(\vec{r} - \vec{r}_0) \quad (4.17)$$

and is therefore given by

$$G_\nu(\vec{r} - \vec{r}_0) = \frac{\kappa_\nu}{4\pi C} \Psi_\nu^T(\vec{r} - \vec{r}_0). \quad (4.18)$$

The sample wave-function also is a solution of the vacuum Schrödinger equation in the region of the tip. If the energies of the tip and sample state are the same the decay constant in this Schrödinger equation for the sample wave-function will be the same as in Eq. (4.16)

$$\kappa_\nu = \kappa_\mu = \kappa. \quad (4.19)$$

Using Green's theorem to transform the integral in the expression for $M_{\mu\nu}^{ST}$ back

into an integral over the tip region of space one obtains

$$\begin{aligned}
M_{\mu\nu}^{ST} &= -\frac{\hbar^2}{2m} \int_{tip} \left(\Psi_\nu^T(\vec{r})^* \vec{\nabla}^2 \Psi_\mu^S(\vec{r}) - \Psi_\mu^S(\vec{r}) \vec{\nabla}^2 \Psi_\nu^T(\vec{r})^* \right) dV \\
&= -\frac{2\pi\hbar^2}{2m\kappa} C \int_{tip} \left(G_\nu(\vec{r} - \vec{r}_0) \kappa^2 \Psi_\mu^S(\vec{r}) - \Psi_\mu^S(\vec{r}) (\kappa^2 G_\nu(\vec{r} - \vec{r}_0) - \delta(\vec{r} - \vec{r}_0)) \right) dV \\
&= -\frac{2\pi\hbar^2}{2m\kappa} C \Psi_\mu^S(\vec{r}_0)
\end{aligned} \tag{4.20}$$

Substituting this expression for the matrix-element into Eq. (4.15) and replacing the summation over the eigenvalues by an integration over the energy one obtains

$$I \propto \int_{-\infty}^{\infty} (f(\epsilon) - f(\epsilon + eV)) n_T(\epsilon + eV) n_S(\epsilon, \vec{r}_0) d\epsilon \tag{4.21}$$

where n_T denotes the density of states (DOS) of the tip and

$$n_S(\epsilon, \vec{r}_0) = \sum_{\mu} |\Psi_{\mu}^S(\vec{r}_0)|^2 \delta(\epsilon - \epsilon_{\mu}) \tag{4.22}$$

is the local density of the sample at the position \vec{r}_0 of the tip apex atom. Equation (4.21) gives an easy tool for the interpretation of STM images. The basic quantity which is imaged is the local density of states of the sample states. In addition, to simplify the interpretation even further one normally assumes the density of states for the tip n_T to be a constant. This is the so called Tersoff-Hamann model of STM which is widely used.

Even though this model has been very successful it fails in some cases. Most important, it turns out that the corrugation amplitude of closed packed metal surfaces predicted by this model is by far too small to explain observed atomic resolution. I will show in the next section how this problem can be dealt with by an extension of the model.

Another problem lies in the restriction to small bias voltages V . The use of high voltages will lead to different decay-constants for the vacuum wave-functions of the tip and the sample. This will lead to a breakdown of the derivation (Eq. (4.19)). This is, however, not so serious for the application presented here, since STM experiments on metal surfaces with atomic resolution mostly operate with very low bias voltages in the mV range. These voltages are much smaller than the undisturbed vacuum barrier of typically 4-6 eV. Furthermore, even Bardeen's approximation does not hold for larger voltages because the basic assumption of the separation of the potentials in a way that the tip potential is zero in the sample region and vice versa becomes

questionable with high applied bias voltages and the vacuum barrier is therefore ill described by this model at higher bias voltages.

Thus this model can only be trusted for low bias voltages below 1 V. To make the discussion clearer and to allow an easier identification of electronic structure effects I will present corrugation amplitude plots in a wider voltage range later on. However, one has to be very careful in the interpretation of effects occurring in these plots at higher bias voltage.

4.6 Chen's extensions to the Tersoff-Hamann model

As noted before, the corrugation amplitude predicted for close-packed metal surfaces by the Tersoff-Hamann model turns out to be too small compared with experimental values. Chen pointed out [Che90, Che92, Che93] that this is due to the restriction to s -like tip orbitals only.

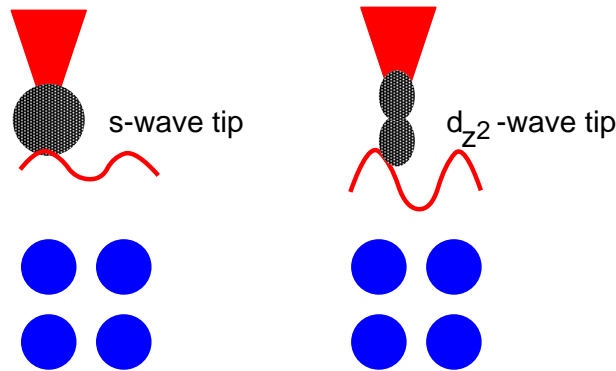


Figure 4.4: Simple picture of an increase of the corrugation by a 'sharper' d_{z^2} -wave tip orbital as compared to an s -wave tip orbital

As Fig. 4.4 shows, it is quite intuitive to assume that a more directed tip-state like a d_{z^2} -state pointing towards the sample might lead to higher values of the corrugation amplitude. This idea can be used to extend the Tersoff-Hamann model for other tip-states than the s -wave tip assumed in the previous section.

Chen showed that other tip states can also be related to the Green's function of the vacuum-Schrödinger equation. This formalism finally leads to Chen's 'derivative rule' which give a simple dependence of the matrix-element $M_{\mu\nu}^{ST}$ from the tip orbital. The matrix elements derived from this rule are listed in Table (4.1) for some tip orbitals other than an s -wave tip. The sample wave-functions essentially have the form

$$\Psi_{\mu}^S \propto \exp(-\kappa_{\mu}z) \quad (4.23)$$

Tip wave-function orbital type	Matrix element according to Chen $M_{\mu\nu}^{ST} \propto$
s	$\Psi_{\mu}^S(\vec{r}_0)$
p_x	$\frac{\partial}{\partial x} \Psi_{\mu}^S(\vec{r}_0)$
p_y	$\frac{\partial}{\partial y} \Psi_{\mu}^S(\vec{r}_0)$
p_z	$\frac{\partial}{\partial z} \Psi_{\mu}^S(\vec{r}_0)$
$d_{z^2-r^2/3}$	$\left(\frac{\partial^2}{\partial z^2} - \frac{\kappa_{\mu}^2}{3}\right) \Psi_{\mu}^S(\vec{r}_0)$

Table 4.1: Some matrix elements as obtained by Chen's derivative rule. In the case of a $d_{z^2-r^2/3}$ -orbital the vacuum decay constant κ_{μ} has to be used to obtain the matrix element.

where z is the coordinate perpendicular to the surface. Hence one easily realizes that the inclusion of tip-orbitals which are directed towards the sample, like the p_z or $d_{z^2-r^2/3}$ -orbital, lead to a matrix element which is still proportional to the wave-function at the position of the tip. However, the prefactor changes, leading to a higher current. Therefore, the inclusion of different tip states into the models explains the experimentally observed high corrugation amplitude. Furthermore, it can be deduced from this discussion that the results obtained by the Tersoff-Hamann approximation while being quantitatively too small will still be correct qualitatively.

Since the absolute value of the corrugation amplitude is a value which depends on quantities like the actual tip state or the tip sample distance which are not controllable in the experimental setup, I will not present any results with different assumed tip orbitals while having in mind that the actual corrugation amplitude observed in experiments will in general be larger than the calculated corrugation.

4.7 'Technical' Aspects

In this section I will shortly describe how the results from the FLEUR-code are used to obtain quantities which can be compared to experiments, i.e. how the theory described so far is actually used.

For calculations based on the Tersoff-Hamann model the basic quantity which has to be known is the local density of states in the vacuum at the tip position. As stated before, this quantity is easily obtained by the formula

$$n(\vec{r}, \epsilon) = \sum_{\mu} |\Psi_{\mu}^S(\vec{r})|^2 \delta(\epsilon - \epsilon_{\mu}) \quad (4.24)$$

which is directly evaluated by the FLEUR-code.

4.7.1 Calculation of the corrugation-amplitude

Since STM is mostly used in constant-current mode, not the tunnel-current but the corrugation of the tip is the quantity which is most suitable to make contact with the experiment. Therefore, I will shortly describe how one can calculate this quantity from the results obtained so far.

The tunnel-current is a function of the tip-sample distance

$$I(\vec{r}_{\parallel}, z) \propto \exp(-2\kappa z) \quad (4.25)$$

where z is again the tip coordinate perpendicular to the surface and the subscript $_{\parallel}$ “ denotes components parallel to the surface. In constant current mode, the current has to fulfil

$$\begin{aligned} 0 &= dI(\vec{r}_{\parallel}, z) \\ &= \frac{\partial I}{\partial z}(\vec{r}_{\parallel}, z) dz + \vec{\nabla}_{\parallel} I(\vec{r}_{\parallel}, z) d\vec{r}_{\parallel} \end{aligned} \quad (4.26)$$

which can be solved for dz

$$dz = -\frac{\vec{\nabla}_{\parallel} I(\vec{r}_{\parallel}, z) d\vec{r}_{\parallel}}{\frac{\partial I}{\partial z}(\vec{r}_{\parallel}, z)}. \quad (4.27)$$

This equation determines the corrugation of the tip dz . To obtain the corrugation amplitude one has to integrate Eq. (4.27) over a path in the surface unit cell which connects the point of maximal $\vec{r}_{\parallel}^{max}$ and minimal current $\vec{r}_{\parallel}^{min}$ in the surface unit cell. For the corrugation at an averaged distance of z_0 one obtains to first order

$$\Delta z(z_0) = \left| \int_{\vec{r}_{\parallel}^{min}}^{\vec{r}_{\parallel}^{max}} \frac{\vec{\nabla}_{\parallel} I(\vec{r}_{\parallel}, z_0)}{\frac{\partial I}{\partial z}(\vec{r}_{\parallel}, z_0)} d\vec{r}_{\parallel} \right| \quad (4.28)$$

An additional approximation is applied to calculate the corrugation amplitude. The expression in the denominator is dominated by the \vec{r}_{\parallel} independent contribution to the current. This basically means that the change in the tunnel current for different tip positions in the surface unit-cell is small with respect to the total current. Furthermore, one can assume that the states contributing to the current basically decay like $\exp(-\kappa z)$ where κ is the work-function. This leads to

$$\Delta z(z_0) = \left| \frac{I(\vec{r}_{\parallel}^{max}, z_0) - I(\vec{r}_{\parallel}^{min}, z_0)}{2\kappa \bar{I}(z_0)} \right| \quad (4.29)$$

where \bar{I} denotes the average of the current over the unit-cell.

4.7.2 Star representation of the corrugation-amplitude

The tunneling current in the model of Tersoff and Hamann is proportional to the local density of states of the sample. This quantity is invariant under all symmetry operations which leave the lattice invariant, i.e. it possesses the same symmetry as the lattice. This fact can be used to expand the local density of states and therefore also the tunneling current into so called star-functions. A star-function is formed by a simple linear combination of all plane-waves with reciprocal lattice vectors that can be mapped into each other by the symmetry operations of the lattice. A simple example might illustrate this. For a lattice with no other symmetry than inversion symmetry the plane-waves with wave-vector \vec{G} and $-\vec{G}$ are obviously equivalent by symmetry. In an plane-wave expansion of the local density of states

$$n(\vec{r}) = \sum_{\vec{G}} n_{\vec{G}} e^{i\vec{G}\vec{r}} \quad (4.30)$$

the coefficients $n_{\vec{G}}$ and $n_{-\vec{G}}$ therefore will be the same and this local density of states can be expanded into star-functions $\Phi_i(\vec{r}) = e^{i\vec{G}_i\vec{r}} + e^{-i\vec{G}_i\vec{r}}$ instead:

$$n(\vec{r}) = \sum_i n_i \Phi_i(\vec{r}). \quad (4.31)$$

This expansion obviously has the advantage of being less memory consuming. In the context of STM experiments, however, another point should be stressed.

The expansion into plane-waves and therefore also the expansion into star-functions can be used to determine which states do contribute most to the local density of states in the vacuum.

Writing a wave-function of the sample $\Psi_{\vec{k}_{\parallel}}(\vec{r})$ as a two-dimensional Bloch-wave one obtains

$$\Psi_{\vec{k}_{\parallel}}(\vec{r}) = e^{i\vec{k}_{\parallel}\vec{r}_{\parallel}} \sum_{\vec{G}_{\parallel}} d_{\vec{G}_{\parallel}}^{\vec{k}_{\parallel}}(z) e^{i\vec{G}_{\parallel}\vec{r}_{\parallel}} \quad (4.32)$$

where the subscript „ \parallel “ denotes the vector components parallel to the surface and z is the coordinate perpendicular to it. The sum has to be performed over the reciprocal lattice vectors.

A WKB-approximation (see for example [LLP79]) gives the following expression for the z -dependent functions $d_{\vec{G}_{\parallel}}^{\vec{k}_{\parallel}}(z)$

$$d_{\vec{G}_{\parallel}}^{\vec{k}_{\parallel}}(z) \propto \exp\left(-z\sqrt{2m|\epsilon|/\hbar^2 + (\vec{k}_{\parallel} + \vec{G}_{\parallel})^2}\right) \quad (4.33)$$

where ϵ is the energy of the state with respect to the vacuum level. One immediately can see from Eq. (4.33) that wave-functions from the $\bar{\Gamma}$ -point of the two-dimensional Brillouin-zone, e.g. wave-functions $\Psi_{\vec{k}_{\parallel}}$ with $\vec{k}_{\parallel} = 0$, will decay more slowly into the vacuum than wave-functions from other \vec{k}_{\parallel} -points. Furthermore, one can deduce that the $\vec{G}_{\parallel} = 0$ component will dominate for large distances. With the help of the definition of the local density of states this statement can be transferred to the local density of state. The $\vec{G}_{\parallel} = 0$ component, i.e. the zeroth star component, of the local density of states will dominate the total density of states far from the surface and this contribution will be mostly due to states with $\vec{k}_{\parallel} = 0$. This statement describes the intuitive facts that the local density of state will become 'flat' at large distances from the surface and that only states without a momentum parallel to the surface will spread out far into the vacuum.

However this formalism allows to make some further deductions. Substituting Eq. (4.32) into (4.22) gives

$$\begin{aligned} n(z, \epsilon) &= \sum_{\vec{k}_{\parallel}} \delta(\epsilon - \epsilon_{\vec{k}_{\parallel}}) \sum_{\vec{G}_{\parallel}} d_{\vec{G}_{\parallel}}^{\vec{k}_{\parallel}}(z)^* e^{-i\vec{G}_{\parallel}\vec{r}_{\parallel}} \sum_{\vec{G}'_{\parallel}} d_{\vec{G}'_{\parallel}}^{\vec{k}_{\parallel}}(z) e^{i\vec{G}'_{\parallel}\vec{r}_{\parallel}} \\ &= \sum_{\vec{k}_{\parallel}} \delta(\epsilon - \epsilon_{\vec{k}_{\parallel}}) \sum_{\vec{G}_{\parallel}\vec{G}'_{\parallel}} d_{\vec{G}_{\parallel}}^{\vec{k}_{\parallel}}(z)^* d_{\vec{G}'_{\parallel}}^{\vec{k}_{\parallel}}(z) e^{i(\vec{G}'_{\parallel}-\vec{G}_{\parallel})\vec{r}_{\parallel}} \end{aligned} \quad (4.34)$$

where the first sum has to be performed over all eigenstates labeled by \vec{k}_{\parallel} and the second sum is again the sum over all reciprocal lattice vectors. (The additional band-index of the eigenstates, which also has to be summed over, has been omitted.) Together with Eq. (4.33) this expression can be used to determine which states contribute most to the coefficients of the star decomposition of the local density of states. These coefficients are given by

$$n_i(z) = \sum_{\vec{k}_{\parallel}} \delta(\epsilon - \epsilon_{\vec{k}_{\parallel}}) \sum_{\Delta\vec{G}_{\parallel}^i} \sum_{\vec{G}_{\parallel}} d_{\vec{G}_{\parallel}}^{\vec{k}_{\parallel}}(z)^* d_{(\Delta\vec{G}_{\parallel}^i-\vec{G}_{\parallel})}^{\vec{k}_{\parallel}}(z), \quad (4.35)$$

where the second sum has to be performed over all plane-wave-vectors $\Delta\vec{G}_{\parallel}^i$ of the i -th star-function.

As I will use simple square unit-cells later on, I will shortly describe the results this analysis gives for this symmetry: The first star is formed by plane-waves with $\Delta\vec{G}_{\parallel} = (1, 0), (0, 1), (-1, 0)$ and $(0, -1)$. The second star by waves with $\Delta\vec{G}_{\parallel} = (1, 1), (-1, 1), (-1, -1)$ and $(1, -1)$. Since the values for $d_{\vec{G}_{\parallel}}^{\vec{k}_{\parallel}}(z)$ become neglectably small for higher \vec{G}_{\parallel} values only the lowest \vec{G}_{\parallel} contributions to the sum in Eq. (4.35) do contribute. It can be seen quite easily that for the first star contribution these

lowest \vec{G}_{\parallel} contributions are dominated from states with $\vec{k}_{\parallel} = (0.5, 0)$ or symmetry equivalent points. Thus, states at the \bar{X} -point of the surface Brillouin-zone dominate the first star contribution to the local density of states in a square lattice. Completely analogously, the second star component is dominated by points at the \bar{M} -point. Figure 4.5 shows this different contribution to the star coefficients for the Brillouin-zone of a square lattice.

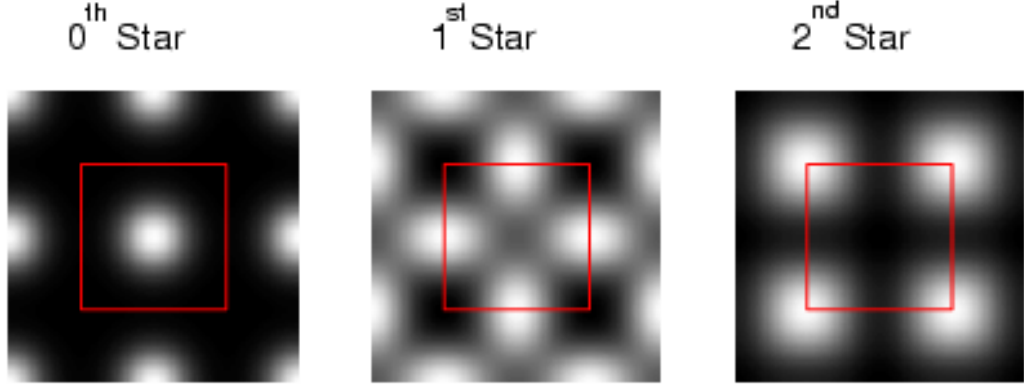


Figure 4.5: The different contributions of states to the star coefficients of the local density of states. The plots show the reciprocal space. The Brillouin-zone of a square lattice is marked. For the different star contributions different regions in the Brillouin-zone contribute most in the vacuum.

Having expanded the local density of states into star-functions this expansion also holds for the tunneling current in the Tersoff-Hamann model (Eq. (4.21)). This can be used to write the corrugation amplitude in terms of star-functions. Substituting Eq. (4.31) into Eq. (4.29) yields

$$\Delta z(z_0) \propto \left| \frac{\sum_i n_i \left\{ \Phi_i(\vec{r}_{\parallel}^{max}, z_0) - \Phi_i I(\vec{r}_{\parallel}^{min}, z_0) \right\}}{\kappa n_0(z_0)} \right|. \quad (4.36)$$

The denominator of Eq. (4.29) contains only the zeroth star coefficient as all other contributions will have zero average over the unit-cell.

Chapter 5

STM of the $c(2 \times 2)$ MnCu/Cu(100) surface alloy

In this chapter I will use the theory described before to calculate STM images of a surface alloy.

If one deposits Mn onto the clean Cu(100) surface the formation of an ordered surface alloy can be observed [FHW92, WGB93, WKFG93, vdKvK95, RVW⁺97, FJW97a, FJW97b]. The Mn atoms are incorporated into the surface Cu-layer and a highly ordered structure can be found at a Mn coverage of 0.5 monolayer. LEED [FHW92, WGB93, WKFG93] as well as STM experiments [NHDJ⁺94, vdKvK95, WJFB96] show that a $c(2 \times 2)$ superstructure is formed. This superstructure consists of a two-dimensional alloy in the surface layer in which every second Cu atom is replaced by a Mn atom. This alloy possesses a surprising degree of stability at room temperature and it was even found to be stable for temperatures up to 400K [WGB93]. The formation of this alloy will be particularly surprising if one realizes that no ordered Mn-Cu bulk alloy exists.

5.1 Review of experimental results

In Ref. [FHW92] Wuttig *et al.* report on experiments demonstrating the formation of a $c(2 \times 2)$ surface alloy of Mn on Cu(100). In their LEED results the refraction pattern clearly indicates the formation of a superstructure on the surface. This result was confirmed by *ab initio* calculations [WGB93] showing that it is energetically favorable for the system to form an ordered surface alloy. The structure of this alloy can be seen in Fig. 5.1.

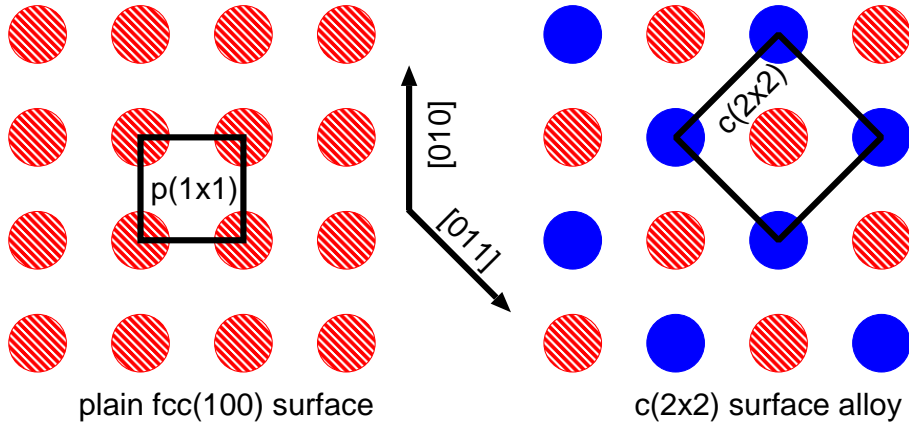


Figure 5.1: Structure of the $c(2\times 2)$ surface alloy on a fcc(100) surface. The left part of the picture shows a clean (100) surface of a fcc-crystal. The $p(1\times 1)$ surface unit-cell is marked. In the right half of the picture every second surface atom is replaced by another element. This checkerboard type alloy structure is called a $c(2\times 2)$ surface alloy. The unit-cell of this structure is rotated and enlarged by a factor of 2 with respect to the $p(1\times 1)$ unit-cell.

The energy gain by the formation of the ordered surface alloy was attributed to a magnetical driven buckling of the surface. In the *ab initio* calculations it turned out that the magnetic moment of the Mn atoms induce a relaxation of the alloy in which the Mn atoms are displaced outwards with respect to the Cu surface atoms. This relaxation was identified to be due to magnetic effects since it only occurs in magnetic calculations while treating the Mn atom without any moment did not lead to any relaxation. It was concluded that the relaxation leads to a reduction of the overlap between the Mn orbitals and those of the next-neighbor Cu atoms which increases the magnetic moment of the Mn atoms towards the free-atom limit. This increased moment is thought to explain the energy gained by the relaxation and to be responsible for the observed stability of the alloy.

The relaxation of the Mn atoms found in the *ab initio* calculations are of the order of 14% (0.25 Å) of the interlayer distance in a LDA-calculation [WGB93]. I/V-LEED confirmed this value with a slightly bigger relaxation of 16.6% (0.3 Å) [Blü96]. This difference in theory and experiment is probably mostly due to the use of the LDA. The remaining difference is due to the improper description of the magnetic moment in the calculation. The magnetic moment of $3.84 \mu_B$ as obtained in the calculation is probably too small [OT95]. I will come back to this issue in Section 5.5. At this stage, however, it must be emphasized that the relaxation found both by the *ab initio* theory and I/V-LEED experiments is very large and these results are in good agreement.

Since this alloy consists of atoms of two different elements in the surface layer and

because of the large relaxation of the Mn atoms this alloy was subject to several STM studies [NHDJ⁺94, vdKvK95, WJFB96]. As expected, STM images with atomic resolution clearly show the $c(2\times 2)$ structure of the surface. The chemical contrast in these images, i.e. the difference of the current at the Mn and at the Cu-positions of the surface was found to be very high. Thus, only the $c(2\times 2)$ unit-cell could be resolved and the $p(1\times 1)$ surface cell was not observed in these pictures (e.g. Fig. 5.13). There has, however, been considerable discussion over the interpretation of the observed corrugation amplitude. While in the publication of Noh *et al.* [NHDJ⁺94] a corrugation amplitude of only 0.1 Å was reported, the group of van der Kraan and van Kempen [vdKvK95], found a higher corrugation amplitude of 0.3-0.4 Å which seemed more consistent with the LEED results.

Wuttig *et al.* [WJFB96] also performed an STM study of single Mn defects incorporated into the Cu(100) surface layer. A line scan across this single atom revealed a corrugation of 0.3 Å between the Mn position and the Cu surface. Since this is too small to be the protrusion produced by a single Mn ad-atom on the surface it was concluded that this single Mn atom was incorporated into the surface and that the corrugation amplitude found here was in perfect agreement with the relaxation found in the LEED experiment. At this point the question arises whether the relaxation of a single Mn impurity is expected to be the same as the relaxation of Mn in the $c(2\times 2)$ MnCu surface alloy. It is, however, quite reasonable to assume that the relaxations may at least be very similarly. In the $c(2\times 2)$ alloy Mn does already only has Cu atoms as nearest neighbors. Hence, to a good approximation Mn atoms in the $c(2\times 2)$ alloy can already be considered to be Mn impurities. A decrease of the concentration of the Mn atoms in the surface changes the magnetic moment only slightly from $3.85 \mu_B$ in the $c(2\times 2)$ alloy to $4.05 \mu_B$ in the $p(2\times 2)$ alloy. Since the relaxation of Mn is basically controlled by the magnetic moment, the relaxation therefore also should change little between the $c(2\times 2)$ alloy, the $p(2\times 2)$ alloy, and a single Mn impurity.

At this point it should be emphasized that in the interpretation of the STM images it was always assumed that the surface relaxation contributes most to the observed corrugation amplitude measured in STM. In other words, the protrusions in the STM images were always attributed to the Mn positions, while the Cu atoms were thought to be at the sites shown as depressions of the $c(2\times 2)$ pattern. This could not be motivated by direct experimental evidence since no further feature which allows a distinction of the atoms is available in the $c(2\times 2)$ alloy case. Since the alloy consists of an equal number of Mn and Cu atoms especially no information regarding this question can be obtained from experiments at different coverages of Mn. At lower

coverages of Mn, the ordered surface alloy is not formed. This identification of the protrusions in the STM image as Mn sites suggests the interpretation of the corrugation amplitude as a measure of the geometric surface relaxation. From this Noh *et al.* [NHDJ⁺94] directly concluded that the observed corrugation amplitude seemed to be too small to agree with the LEED results for the relaxation.

In the following sections it will be shown that this interpretation of the STM images is misleading. This is done by comparing *ab initio* calculations of the STM images with the experimental results.

5.2 $c(2\times 2)$ MnCu alloy on the Cu(100) surface

Two configurations were used to calculate STM images: First the unrelaxed alloy in which all atoms are placed according to the ideal Cu lattice sites. This system should allow the identification of effects which are due to the electronic structure of the system. To investigate the effect of the lattice relaxation on the STM image I used a second configuration where the Mn atoms and the Cu atoms of the surface layer were replaced according to the relaxation found by Wuttig *et al.* [WKFG93]. A direct comparison between the two systems shows that many results do not depend strongly on the amount of surface relaxation and therefore it is not necessary to repeat the *ab initio* calculations of the relaxation of the structure.

As described in Chapter 3 the surfaces are modeled in the film geometry. The film used here consists of a total of 11 layers including two alloy layers on each side of the film. The experimental lattice constant ($a_0=3.61$ Å) and the local spin-density approximation to the exchange correlation potential are used. Comparing the results with calculations using a thicker film (21 layers) or the GGA exchange correlation potential shows no significant influence on the results.

The system is converged using 36 special \vec{k}_{\parallel} -points [Cun74] in the irreducible wedge of the two-dimensional surface Brillouin zone. The FLAPW-basis in these calculations consisted of ~ 100 basis-functions per atom ensuring fully converged results with respect to the basis-cutoff. To increase the accuracy of the local density of states used to obtain the corrugation amplitude, the number of \vec{k}_{\parallel} -vectors is increased to 91 in these calculations to describe the bands with low dispersion more accurately.

As described in Section 4.7.2 the local density of states and the corrugation amplitude are expressed in terms of star coefficients and star-functions. I will therefore shortly describe at this point the first three star-functions for a $c(2\times 2)/fcc(100)$

unit-cell. As one can see from Fig. 5.1 the lattice possesses a square symmetry. This leads to the following symmetry invariant groups of \vec{G}_{\parallel} -vectors: the smallest \vec{G}_{\parallel} vector is $(0, 0)$ which is the generating vector of the zeroth star-function. The first star-function is formed by four plane-waves with the wave-vectors \vec{G}_{\parallel} of $(1, 0)$, $(-1, 0)$, $(0, 1)$, and $(0, -1)$ (in units of $\frac{2\pi}{a_0}$) and the second star-function consists of four plane-waves with $\vec{G}_{\parallel} = (1, 1)$, $(-1, 1)$, $(1, -1)$, and $(-1, -1)$. Therefore these star-functions Φ_i have the following form:

$$\Phi_0 = \text{const.} \quad (5.1)$$

$$\Phi_1(\vec{r}_{\parallel}) = \frac{1}{2}(\cos x + \cos y) \quad (5.2)$$

$$\Phi_2(\vec{r}_{\parallel}) = \frac{1}{2}(\cos(x + y) + \cos(x - y)) \quad (5.3)$$

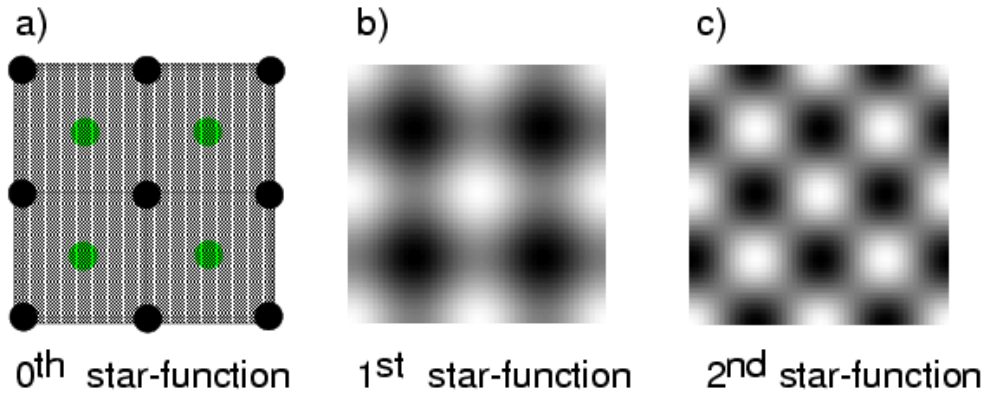


Figure 5.2: First three star-function for a square surface unit-cell. The zeroth star-function is constant throughout the unit-cell and therefore the atom-positions of a $c(2 \times 2)$ alloy are shown in a). b) and c) show the first and second star-function respectively.

As one can see in Fig. 5.2 the first star-function shows the $c(2 \times 2)$ surface structure, i.e. one atom site is seen as protrusions while the other is seen as depression. Therefore, this contribution to the local density of states and to the corrugation amplitude determines the amount of this $c(2 \times 2)$ structure seen in the STM image i.e. this contribution determines the chemical contrast. In the following discussion a sign convention for the corrugation amplitude plots is used. The Mn-position in the two-dimensional unit-cell is always the $(x_{Mn}, y_{Mn}) = (0, 0)$ position. Thus, a positive coefficient of the first star contribution to the corrugation amplitude shows the Mn atoms as protrusions in the STM image and a negative coefficient refers to an images showing the Mn as depressions and the Cu-positions as protrusions.

The second star contribution allows the distinction of the atom positions and the hollow sites of the surface as one can see from Fig. 5.2. Thus, this star coefficient determines the amount of the $p(1 \times 1)$ unit-cell seen in the STM image and therefore

does not lead to any chemical contrast. The following sign convention is chosen: a positive second star coefficient leads to an STM image showing the atom positions as protrusions and the hollow sites as depressions. In plots of the total corrugation amplitude the sign convention of the first star contribution is used. Of course, this is only meaningful if the total corrugation amplitude is dominated by the first star contribution. At bias-voltages where this contribution becomes very small the sign of the total corrugation amplitude becomes meaningless and discontinuities can occur, in which the sign of the corrugation amplitude changes. However, as one will see later, in general the first star contribution is much larger than the second star contribution which in turn is much larger than higher star coefficients.

Because of their rapid decay into the vacuum all star contributions higher than the second one could be neglected in the following discussion of the surface alloys. Equation (4.36) therefore simplifies to

$$\Delta z(z_0) \propto \left| \frac{\sum_i n_i(z_0) \left\{ \Phi_i(\vec{r}_{\parallel}^{max}) - \Phi_i(\vec{r}_{\parallel}^{min}) \right\}}{\kappa n_0(z_0)} \right| \quad (5.4)$$

$$\sim \left| \frac{n_1 \left\{ \Phi_1(\vec{r}_{\parallel}^{max}) - \Phi_1(\vec{r}_{\parallel}^{min}) \right\} + n_2 \left\{ \Phi_2(\vec{r}_{\parallel}^{max}) - \Phi_2(\vec{r}_{\parallel}^{min}) \right\}}{\kappa n_0(z_0)} \right| \quad (5.5)$$

5.2.1 Corrugation of the unrelaxed $c(2 \times 2)$ MnCu surface alloy

The calculated corrugation amplitude (Fig. 5.3) of the STM image of the unrelaxed surface alloy shows several interesting features. First, it can be seen that the first star contribution dominates the total corrugation amplitude. This agrees with the experimental observation of a distinct $c(2 \times 2)$ pattern with protrusions at one atom type and depressions at the other. For bias voltages smaller than 1 V, as usually used in experiments, the corrugation amplitude is negative. With the sign convention introduced in the previous section, Fig. 5.3 can be interpreted. It shows that the protrusions are at the Cu positions of the surface. Furthermore this strong contribution of the $c(2 \times 2)$ pattern to the STM image is dominated by the minority spin electrons, as one can conclude from the graphs for the different spins in Fig. 5.3. Interestingly, the corrugation amplitude due to the minority spin electrons only is larger than the total one. The majority spin contribution reduces the corrugation observable in STM. Hence, a spin-polarized STM would show either a very strong corrugation with protrusions at the Cu sites or a smaller corrugation with protrusions at Mn sites depending on the magnetization of the tip.

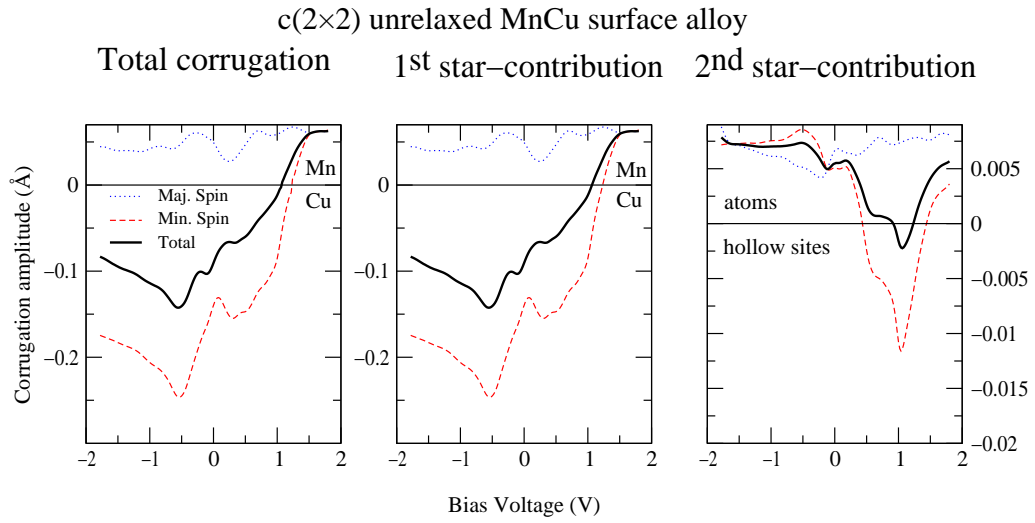


Figure 5.3: Calculated corrugation amplitude for the $c(2\times 2)$ MnCu surface alloy with all surface atoms at ideal Cu positions. (a) shows the total corrugation amplitude as calculated from the first three star coefficients, (b) the corrugation amplitude resulting from only the first star contribution and (c) the corrugation amplitude resulting from only the second star contributions. In all plots both spin contributions and the resulting total corrugation amplitude are shown.

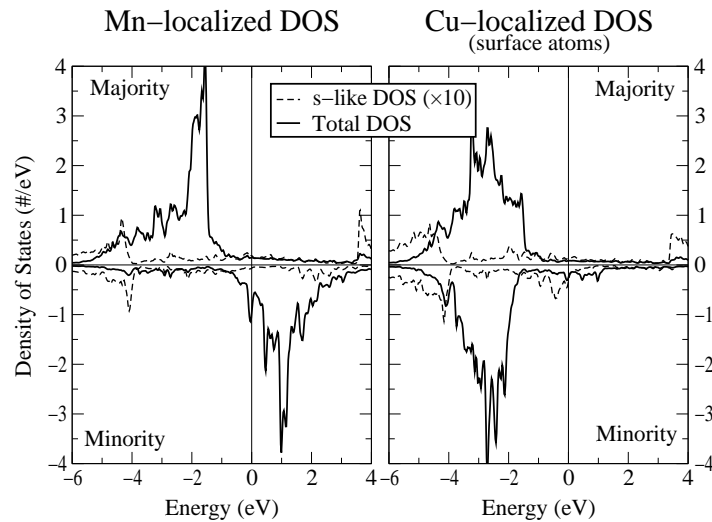


Figure 5.4: Density of states of the surface alloy. The left plot shows the local density of states inside the Mn muffin-tin sphere and the right plot the local density of states inside the surface-Cu muffin-tin sphere. Both, the total DOS for the minority and majority spin and contribution of s -like states are plotted. The s -contribution is magnified by a factor of ten.

The origin of the strong corrugation amplitude can be traced back to the electronic structure of the alloy. Figure 5.4 shows the local density of states inside the muffin-tin spheres of the surface atoms.

Please note, that in this and in all following sections all energies are measured with respect to the Fermi-energy. Thus, the Fermi-energy will be at 0 eV. The surface Cu localized density of states, as shown in Fig. 5.4, is dominated by the Cu d -bands around -2 eV. These states are well below the Fermi energy and do not contribute to the tunneling current at all. Therefore, only Cu s -bands are involved in the tunneling process. The majority d -bands of Mn are also well below the Fermi-energy and do not contribute. Because of the magnetic exchange splitting, the minority d -bands, however, lie just above the Fermi-energy and a small tail of the d -band density of states reaches down to the Fermi-energy. This gives a first indication why the minority spin contribution to the corrugation amplitude dominates the total corrugation amplitude. However, it must be noticed that the minority spin current not only determines the total corrugation amplitude but also shows the Cu positions as protrusions which is somehow surprising for Mn localized states. To find the states responsible for these protrusions in the STM images, one has to investigate the electronic structure in greater detail.

The band-structure (Fig. 5.5) of the system confirms the findings of the density of states plots. The Cu and Mn d -bands can easily be identified. Furthermore, one notices some occupied Mn-localized minority states at the \bar{X} -point of the surface Brillouin zone. In Section 4.7.2, a discussion of the contribution of states from different points in the surface Brillouin-zone was presented. In the special case of a square symmetry the first star contribution is dominated by states from the \bar{X} -point of the surface Brillouin-zone and the second star contribution is dominated by states from the \bar{M} -point of the surface Brillouin zone. Thus, some states must exist at the \bar{X} -point which spread out far into the vacuum, because the corrugating part of the local density of states is dominated by the first star contribution.

Fig. 5.6 displays both, a part of the majority and minority band-structure and a plot of the first star coefficient to the local density of states. One can identify several flat bands stretching from the \bar{X} - to the \bar{M} -point in the band-structure, which correspond to peaks in the first star contribution to the local density of states. Most obviously, flat minority bands just below the Fermi-energy and at -0.4 eV which have a high d -like localization at the Mn-surface atoms are the origin of the negative peaks in the local density of states. The unoccupied Mn-localized bands above 1 eV on the other hand correspond to positive peaks in the local density of states contribution of the minority spin. The majority bands on the other hand do not contribute much

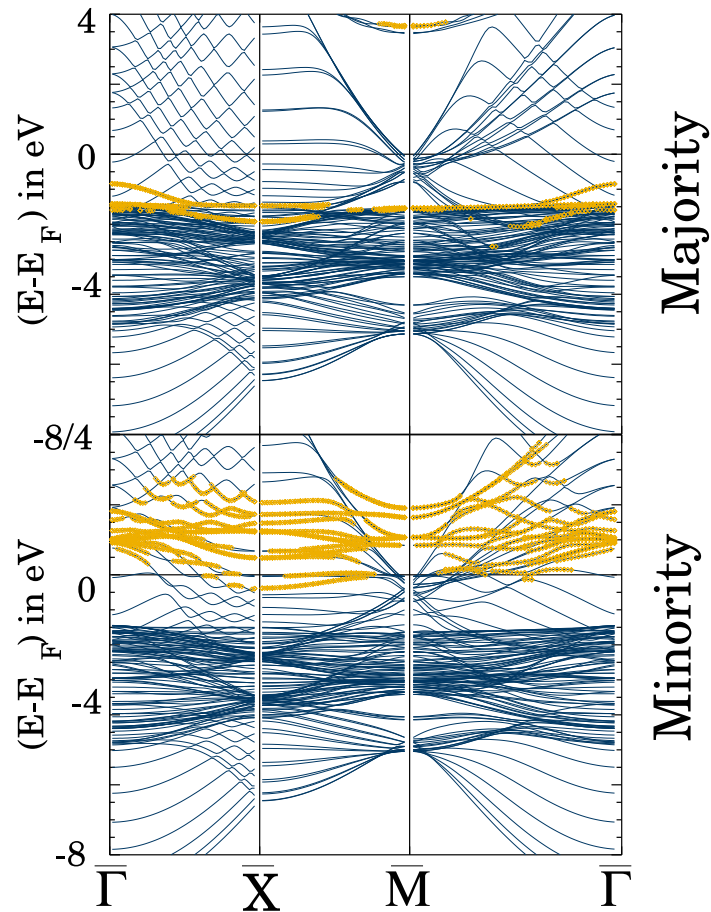


Figure 5.5: Band-structure of the Mn/Cu(100) surface alloy. The upper part shows the bands of the majority spin and the lower the bands of the minority spin. States with a d -charge localized to more than 40% of in the Mn muffin-tin spheres are highlighted.

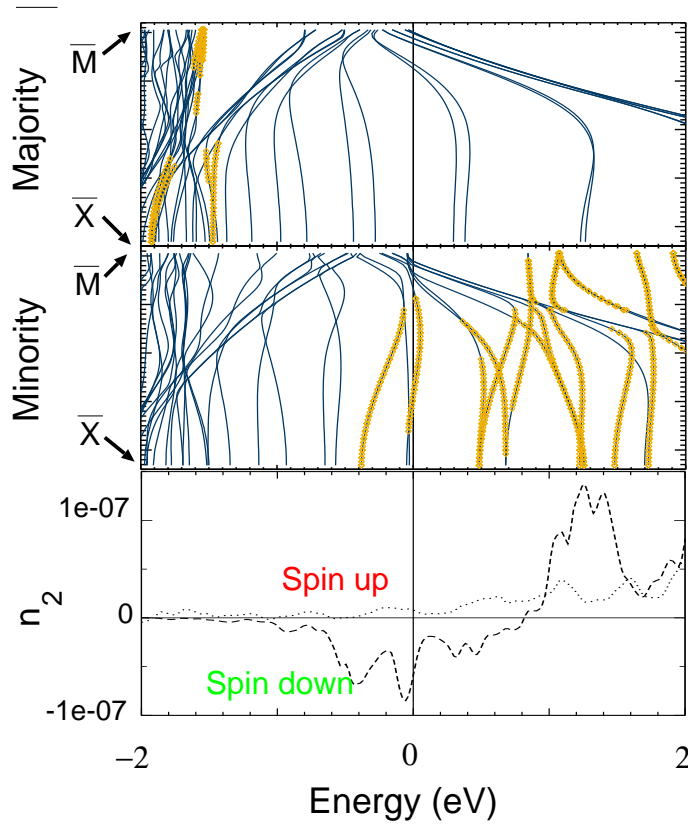


Figure 5.6: Contribution of the bands to the local density of states in the vacuum. The upper two panels show the majority and minority bands along the line from \bar{X} to \bar{M} . The lower part of the plot shows the first star contribution to the local density of states split into minority spin and majority spin contribution.

to the first star coefficient. This means that these states do not generate a strong first star contribution to the local density of states which is not surprising if one has in mind that these majority bands are mostly s -like bands and that, consequently, these states will not distinguish as strongly between Cu and Mn atoms as the Mn d -states do.

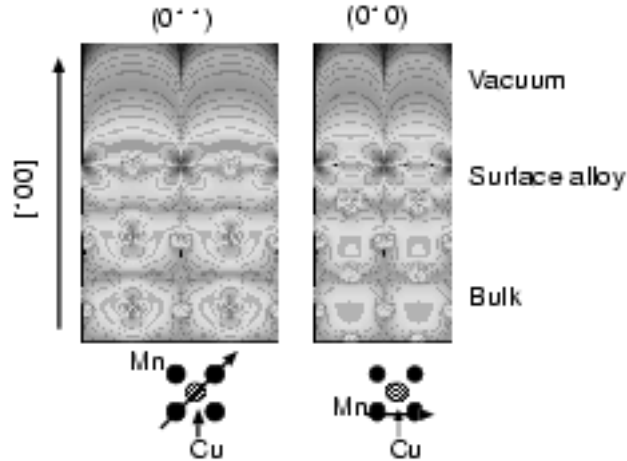


Figure 5.7: Charge density plot in real space of one single minority state just below the Fermi energy at the \bar{X} -point. Two slices along different directions are shown. One in the (011)-plane showing the diagonal of the surface unit-cell with both the Mn and the Cu atom and one in the (010)-plane showing only the Mn surface atoms. The colors indicate the different levels. Red corresponds to the highest density of states, black and violet the lowest.

Having identified the states which dominate the first star contribution to the local density of states, these states can be visualized in real space. Fig. 5.7 shows the contribution to the local density of states by one of the the states at $E = -0.09$ eV and at the \bar{X} -point. This state, while being predominantly localized as a $d_{(x,y)z}$ -state at the Mn atoms, hybridizes with presumable Cu p_z electrons and thus stretches out into the vacuum above the Cu-positions. Therefore, the STM will show the Cu atoms as protrusions, even though the states which dominate the local density of states are mainly localized at Mn positions. At this point I would like to emphasize already that the formation of these states is characteristic for the $c(2 \times 2)$ MnCu surface alloy only. In particular, the formation of these states seem to depend strongly on the nearest-neighbor Mn-Mn interaction along the [010] direction in this alloy. In a more dilute $p(2 \times 2)$ MnCu surface alloy, with a larger nearest-neighbor Mn-Mn distance, these states are absent, even though the distance between the Mn atoms along the [011] direction is unchanged in this $p(2 \times 2)$ alloy.

This result is similar to the theoretically and experimentally found anti-corrugation of the Fe(001) surface [Gen]. At a tip-sample distance of ~ 5 Å the STM shows the

hollow sites as protrusions at small bias voltages. This is due to Fe d -states which bridge over the hollow sites into the vacuum.

5.3 The relaxed surface alloy

Since all the results discussed up to now are obtained using an unrelaxed surface alloy and since the measured buckling of the alloy would favor the Mn positions in STM, I performed calculations for the relaxed $c(2\times 2)$ surface alloy. In this relaxed structure the atom positions are used according to Ref. [WKFG93]. The Mn atoms are displaced by $\Delta_{Mn} = 0.3 \text{ \AA}$ into the vacuum. The Cu surface atom is also moved slightly. Further details on the structure can be found in Fig. 5.8.

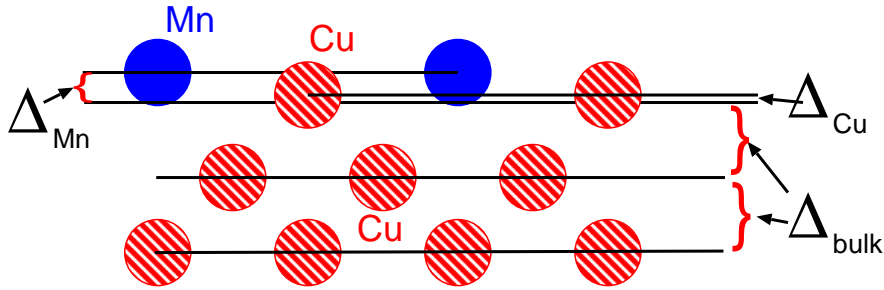


Figure 5.8: Surface relaxation as found in [WKFG93]. The bulk interlayer spacing of $\Delta_{bulk}=1.81 \text{ \AA}$ is enhanced for the surface layer. The surface Cu atoms are displaced by only $\Delta_{Cu}=0.02 \text{ \AA}$ outwards while the relaxation of the Mn-surface atoms is considerably larger $\Delta_{Mn}=0.30 \text{ \AA}$.

As mentioned before, this relaxation will decrease the overlap of the Mn-orbitals with Cu states which in turn will lead to an enhancement of the magnetic moment. In the calculations presented here the moment was found to increase from $3.70 \mu_B$ to $3.85 \mu_B$.

Because of the large relaxation, it was expected that the STM image will show a $c(2\times 2)$ structure with protrusions at the Mn atoms. This would correspond to a positive first star contribution to the corrugation amplitude according to the sign convention for the corrugation amplitude plots. Fig. 5.9 shows the corrugation amplitude of the relaxed structure. Most strikingly, the total corrugation amplitude remains negative for small bias voltages. Instead of a shift of 0.3 \AA in the first star coefficient, as one would anticipate from the large outwards buckling of the Mn atoms, the corrugation amplitude shifts only by 0.05 \AA as one can see by comparing the corrugation amplitudes in Fig. 5.3 with Fig. 5.9, which show the results for the unrelaxed and relaxed structure respectively. Obviously, structural changes cannot

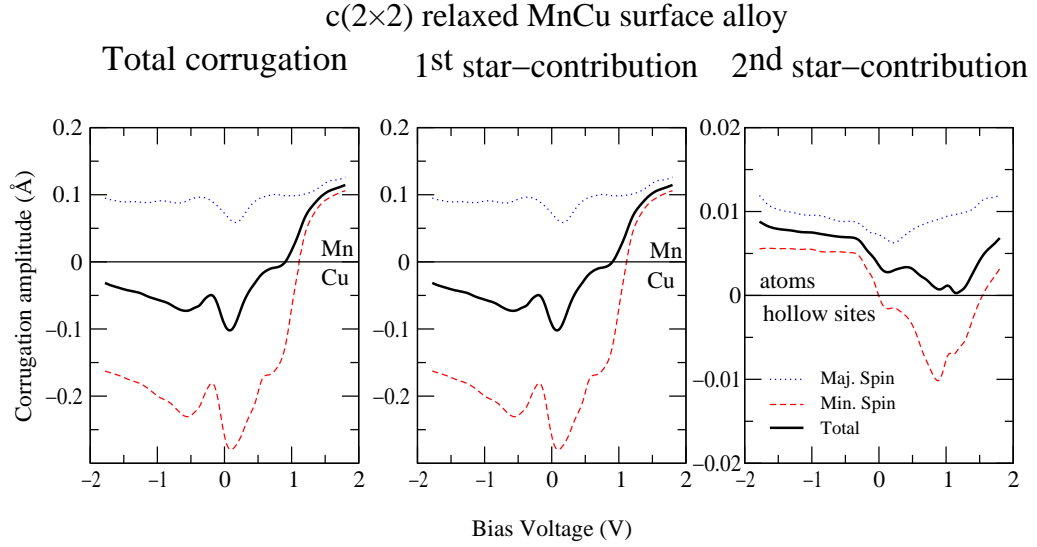


Figure 5.9: Calculated corrugation amplitude for the relaxed c(2×2)MnCu surface alloy. This figure shows a shift in the first star contribution compared to Fig. 5.3.

simply be superimposed in the STM images calculated without relaxation. The surface relaxation reduces the electronic contribution to the STM image, but the corrugation does not change sign and the STM images remain dominated by the electronic structure of the alloy.

As one can see from Fig. 5.10 the muffin-tin localized density of states remains largely unaffected from the relaxation. The increase of the magnetic moment is a clear indication that the exchange splitting of the *d*-like Mn-states is slightly

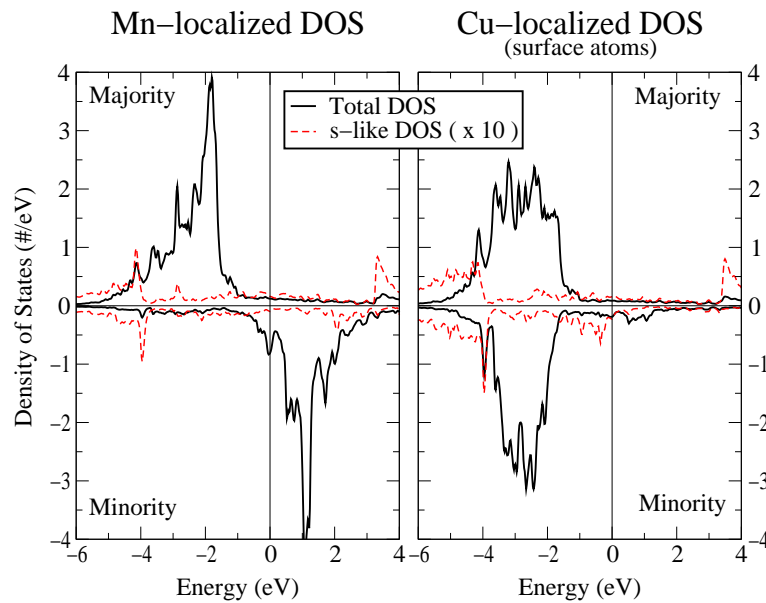


Figure 5.10: Density of states of the relaxed surface alloy (compare to Fig. 5.4).

increased. However, at and just below the Fermi level a considerable amount of minority Mn d -states still contribute to the density of states. A closer look reveals that the states described in the previous section at the \bar{X} -point of the Brillouin-zone remain unaffected from the relaxation. As Fig. 5.11 shows, these states still span the Cu surface sites and therefore they still dominate the local density of states and the corrugation amplitude.

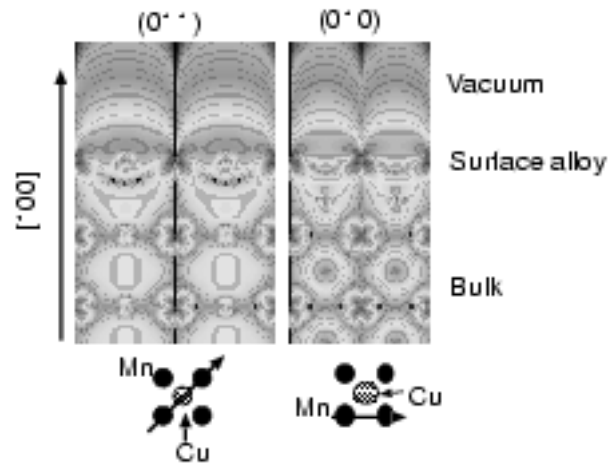


Figure 5.11: Charge density of a single state (compare to Fig. 5.7). The surface buckling is visible by comparing the atom positions in the surface layer. Note however, that the local density of states in the vacuum still is higher at the Cu positions than at the Mn positions.

This strong dependence of the STM image on the electronic structure gives some indication why different experimental groups found contradicting results for the corrugation amplitude in their experiments. It is not the surface relaxation that was directly observed, but the electronic effect on the local density of states was the origin of the chemical contrast in these STM images. Therefore, it was impossible to deduce the surface relaxation from these STM based experiments. The argument over the surface relaxation in the papers by Noh *et al.* [NHDJ⁺94] and Wuttig *et al.* [WJFB96], which is based on the assumption that this corrugation amplitude can be related to the surface relaxation is unjustified from this point of view. The difference in the observed corrugation amplitude in [NHDJ⁺94] and [vdKvK95] is probably due to the tunneling conditions e.g. the tip-sample distance and the electronic configuration of the tip. It cannot be related to the surface buckling.

5.3.1 $p(2\times 2)$ MnCu alloys on the Cu(100) surface

The discussion in the previous sections led to the conclusion that it is impossible to determine the surface relaxation of the $c(2\times 2)\text{MnCu}/\text{Cu}(100)$ alloy from the

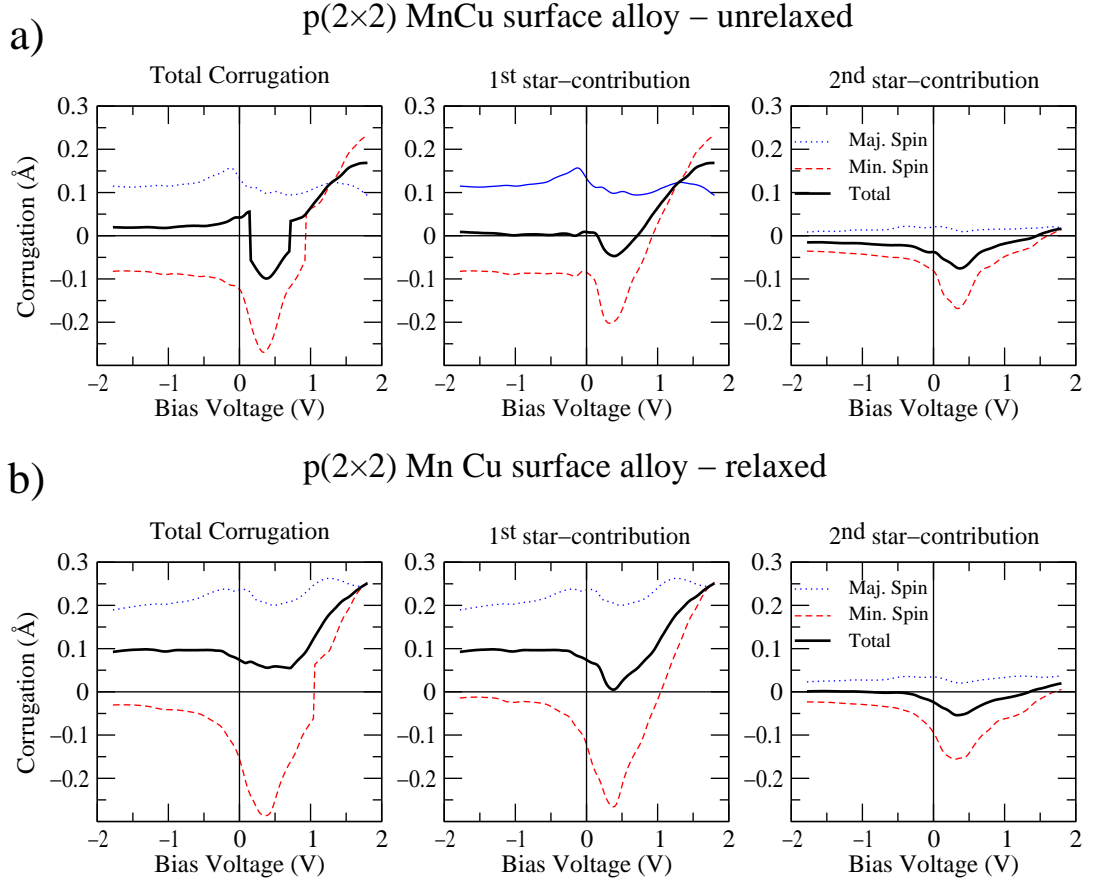


Figure 5.12: Calculated corrugation amplitude for the unrelaxed (a) and relaxed (b) p(2×2) surface alloy. For both configurations, the total, the first and second star contribution are plotted. The first star coefficient does lead to the chemical contrast between the Cu and the Mn sites, while the higher star coefficients do not distinguish between the Cu and Mn surface positions.

STM corrugation amplitude directly. The question remains whether the approach of Wuttig *et al.* [WJFB96], who scanned over a single Mn-defect on the surface, will lead to results related to the surface relaxation. To check this approach I performed calculations on a more dilute alloy.

As the FLEUR-code allows one only to calculate periodic structures, I have chosen the p(2×2) cell with one Mn and three Cu atoms per unit-cell to model a single Mn atom. The Mn next-neighbor distance is increased by a factor of $\sqrt{2}$ in this geometry. It turned out that this increase is sufficient to destroy the state discussed in the c(2×2) alloy case which spans over the Cu atoms into the vacuum. Again calculations for the unrelaxed, ideal surface and for a surface, where the Mn atoms are displaced by 0.3 Å into the vacuum, have been performed.

Fig. 5.12a) shows the corrugation amplitude plot for the unrelaxed system. In this geometry the star contributions have to be interpreted slightly differently than in the

$c(2\times 2)$ unit-cell. The first star-function which still shows the difference between the middle and the corners of the unit-cell now distinguishes between the Mn-position and the Cu atoms at the next-nearest neighbor sites. The second and third star-function show the difference between these positions and the Cu atoms being nearest neighbor atoms to Mn and the difference between all surface atoms and the hollow-sites, respectively. Thus, the first star contribution determines the chemical contrast seen in STM images, while the third star contribution determines the amount of the $p(1\times 1)$ surface unit-cell (compare also Fig. 5.16).

From Fig. 5.12a) it can be seen that for small bias voltages normally used in STM of metal surfaces the total corrugation amplitude of the unrelaxed system is no longer dominated by the first star contribution. In terms of an STM image this means that the chemical contrast between the two different atom sites is rather weak. One can see however, that the two individual spin contributions lead to a considerable chemical contrast. In the total corrugation amplitude these two contributions nearly exactly cancel each other and an STM would detect no or at least only very weak chemical contrast between Mn and Cu.

Fig. 5.12b) presents the corrugation amplitude for a $p(2\times 2)$ system in which the Mn atoms are displaced outwards by 0.3 \AA . Similar to the $c(2\times 2)$ case discussed before the first star contribution to the corrugation amplitude is shifted. However, since there is no chemical contrast in the unrelaxed case the corrugation amplitude now reflects the surface relaxation. If one assumes that the relaxation for a single Mn atom will be the same as for the $c(2\times 2)$ MnCu surface alloy this means that Wuttig *et al.* [WJFB96] took a suitable approach to determine the surface relaxation of the $c(2\times 2)$ alloy by STM by scanning over a single Mn atom included into a Cu surface.

5.4 Comparison with the experiments

If the analysis presented so far is correct, I have shown that the interpretation of the STM images in the works of [NHDJ⁺94] and [WJFB96] for the $c(2\times 2)$ alloy was incorrect. Not the Mn-positions but the Cu-positions in the surface unit-cell are imaged as protrusions. This of course makes it impossible to interpret the corrugation obtained in STM studies of this alloy as the surface buckling.

An experimental finding supporting this new interpretation can be found in Fig. 5.13. The STM image shows a Cu(100) surface covered by half of a monolayer of Mn. A step-edge separates two terraces. On both terraces a square pattern of bright spots is clearly visible. From the size of this pattern which is two times larger than the

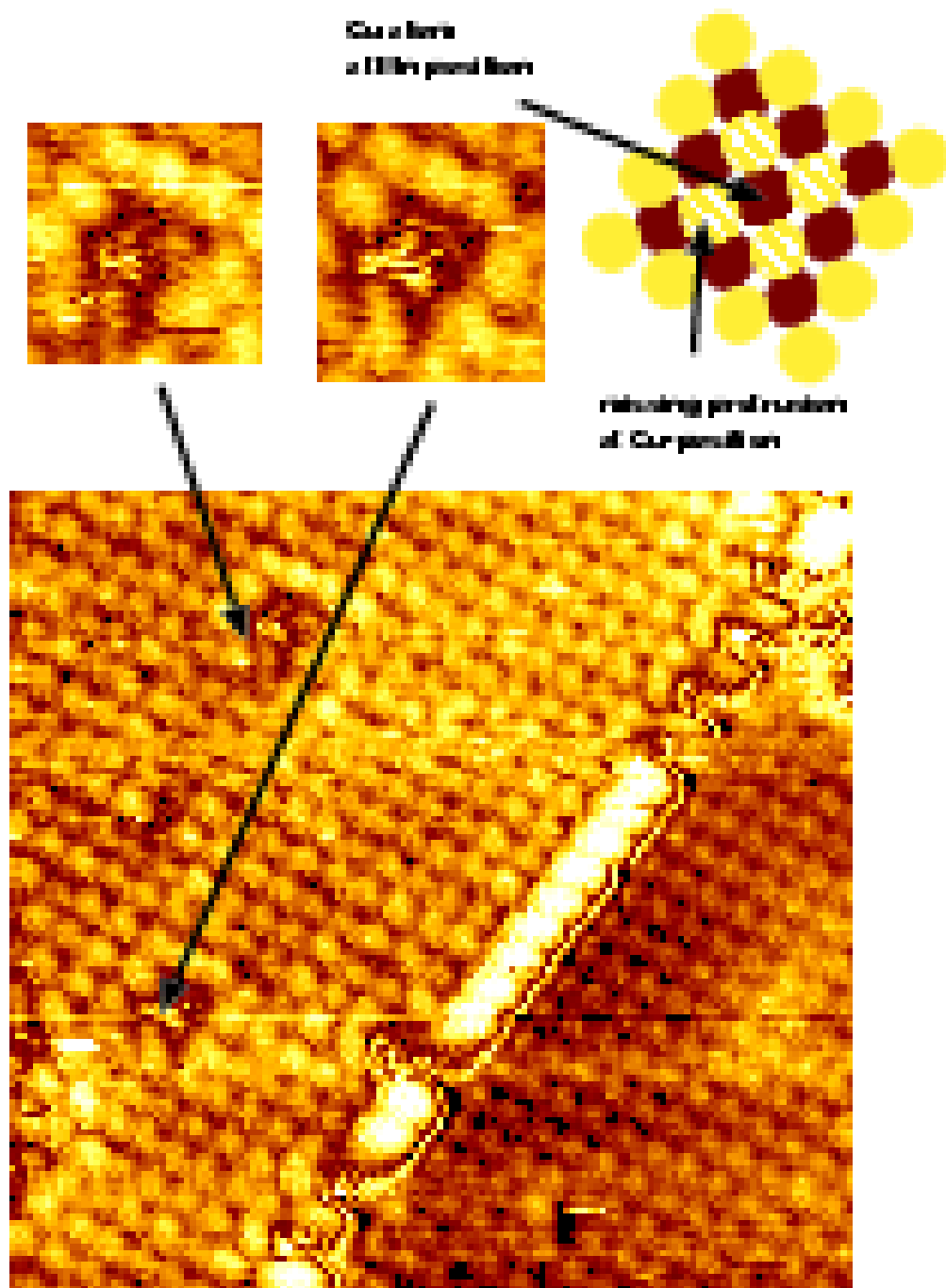


Figure 5.13: STM image of the $c(2 \times 2)$ MnCu alloy. Please note the two defects. STM image from [vdKvK95]. I would like to thank Prof. H. van Kempen for the permission to reproduce it.

surface unit-cell of Cu(100), one can deduce that it corresponds to the $c(2\times 2)$ unit-cell and not to the $p(1\times 1)$ cell. Obviously, a high chemical contrast is observed. Only one type of atoms is visible as protrusions while the atoms of the other type are located at the dark spots of the square pattern. So far, this corresponds perfectly to the results presented here. Of course, the question whether the Cu or the Mn positions are shown as protrusions cannot be answered from these observations.

At this point special attention should be given to the two defects on the left terrace. These defects consist of four missing bright spots of the $c(2\times 2)$ pattern and they are observed to move with time. According to the results presented here, these defects are probably due to one missing Mn atom in the surface alloy. An anti-site defect, a Mn atom which failed to substitute a Cu atom during the growth process, would be one possible example of such a missing Mn atom. If one of the Mn atoms of the alloy is replaced by a Cu atom, the results obtained from the $p(2\times 2)$ MnCu surface alloy suggest that the states bridging over the Cu atom and the increased local density of states over the four nearest-neighbor Cu sites will disappear. This looks then like a defect of four missing bright spots as observed in this STM image. The alternative interpretation would have to assume that these defects are formed by four missing Mn atoms. However, since these defects are observed to move, this interpretation seems extremely unlikely. Therefore, these defects give a clear indication in favor of the interpretation given here.

5.5 Effect of an increased exchange splitting

All results presented so far rely on the fact that some of the minority Mn d -bands cross the Fermi-level near the \bar{X} -point. The states in these bands spread out far into the vacuum and these states create the $c(2\times 2)$ structure in the STM images. This of course raises the question, whether this important feature of the band-structure is described correctly. If these bands are only an artificial result of the LDA exchange-correlation potential used here, the conclusions drawn in the previous sections would be highly questionable.

It is known that the local density approximation used here tends to underestimate the magnetic moments. This obviously indicates that the exchange-splitting between the majority and minority bands could be too small. Therefore, the minority states could be expected to lie a little higher in energy which could also affect the bands at the Fermi-level. To check this, I artificially increased the exchange splitting and recalculated the corrugation amplitude. In order to do this an additional potential

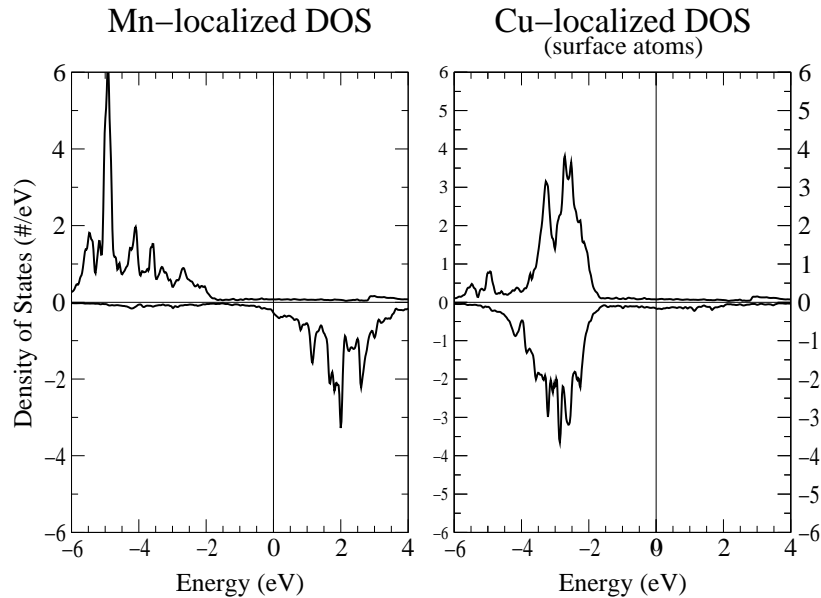


Figure 5.14: Density of states in the muffin-tin spheres of the surface atoms. The exchange splitting of the Mn d -bands is increased.

term was added to the Hamiltonian:

$$H = H_{LDA} \pm |d_{\sigma} \rangle U \langle d_{\sigma}|. \quad (5.6)$$

The additional potential term U lowers the energy contribution of the Mn-localized d -minority spin states while increasing the energy contribution of the majority spin states. This approach can be interpreted in terms of a simple implementation of the LDA+ U method [SLP99].

Figure (5.14) shows the density of states in the muffin-tin region as obtained by introducing an additional potential $U = 1.5$ eV. The exchange splitting is largely increased and definitely too large in this calculation. The main contribution of the majority d -bands of Mn to the density of states lie now below the Cu d -states at around -5 eV. Because of this shift a much larger hybridisation with Cu d -states can be observed leading to a broadening of the Mn d -like density of states. Furthermore the minority Mn d -states are shifted to higher energies. The main peaks now lie above 2 eV and this minority band is also broadened. This broadening is probably due to interactions with s -states. However, and this is the essential result of this calculation, the minority density of states at the Fermi-level remains quite unaffected by this large perturbation. There still exists a considerable amount of minority Mn d -states around the Fermi level. Thus, one expects that the main conclusions

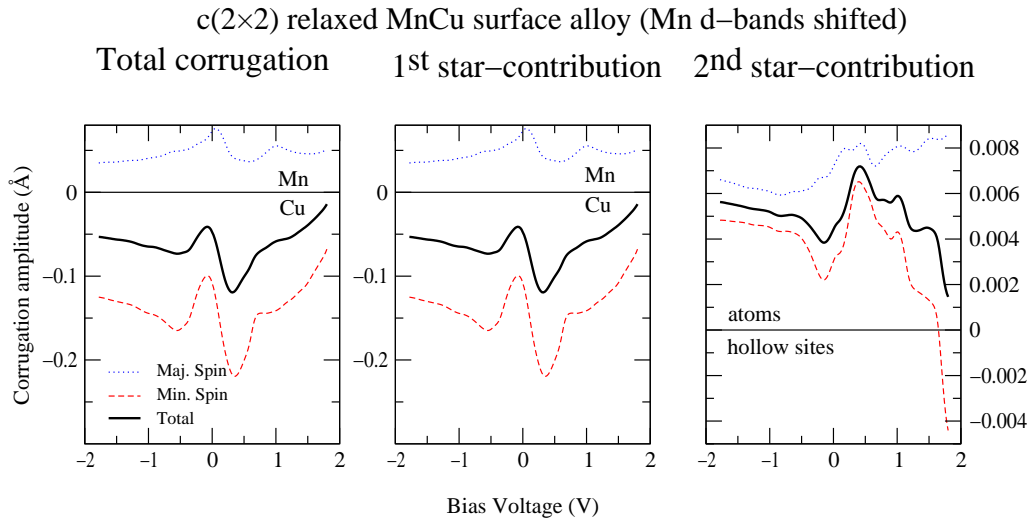


Figure 5.15: Corrugation amplitude for the $c(2\times 2)$ MnCu surface alloy, obtained with an increased exchange splitting of the Mn d -states.

drawn in the previous sections remain valid. This is confirmed by the corrugation amplitude one obtains for this system (Fig. 5.15). The bias voltage dependence of the corrugation amplitude changes slightly, the position of the peaks is a little different, but the total corrugation amplitude remains dominated by the first-star, minority spin contribution and is still negative. Thus, one will still observe the Cu-positions as protrusions in STM images.

The increased exchange-splitting produced by the additional potential is definitely too big, but nevertheless does not alter the results. Consequently, one can safely conclude, that the possible underestimation of the magnetic moment of the Mn atoms and the underestimation of the exchange-splitting in the density of states will not affect the main conclusions drawn in the previous sections.

5.5.1 Anti-ferromagnetic ordering

As a last test the possibility of different magnetic ordering of the surface alloy was investigated. Total energy calculations [RGC⁺97] determined the ferromagnetic ordering of the Mn moments, which was assumed in the results presented so far, to be the energetically favorable configuration. Experiments [OZT93, RGC⁺97] confirmed a high magnetic moment for the Mn but no long range magnetic ordering could be found. Since the Curie temperature of a ferromagnetic system was estimated to be below 50K, these experiments were not capable of distinguishing between a ferromagnetic and an anti-ferromagnetic structure. Even though the *ab initio* calculations as well as analogies with other systems [OZT93] support the ferromagnetic order used

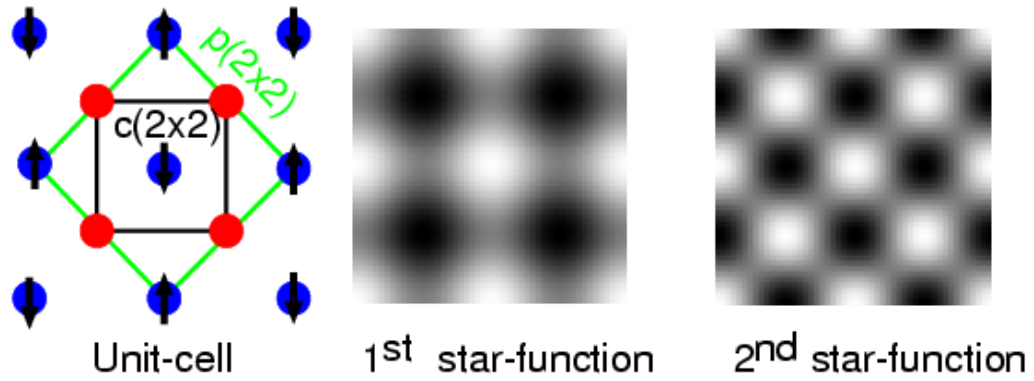


Figure 5.16: $p(2\times 2)$ unit-cell used for the calculation of the anti-ferromagnetic calculation. The first star-functions now shows the difference between the Mn atoms with different spin orientation.

here, an anti-ferromagnetic structure cannot be ruled out completely.

The unit-cell of the chemical $c(2\times 2)$ alloy has to be enlarged to a $p(2\times 2)$ cell to take the two different spin directions of the chemically and structurally equivalent, but magnetically inequivalent, Mn atoms into account. This leads to the simple anti-ferromagnetic structure shown in Fig. 5.16, in which the nearest neighbor Mn atoms couple anti-ferromagnetic. In this unit-cell the ordering of the star-functions is changed as compared to the $c(2\times 2)$ based calculations of the ferromagnetic alloy. The first star coefficient determines the corrugation difference between the two Mn sites and the second star-function corresponds to the first star-function of the $c(2\times 2)$ unit-cell.

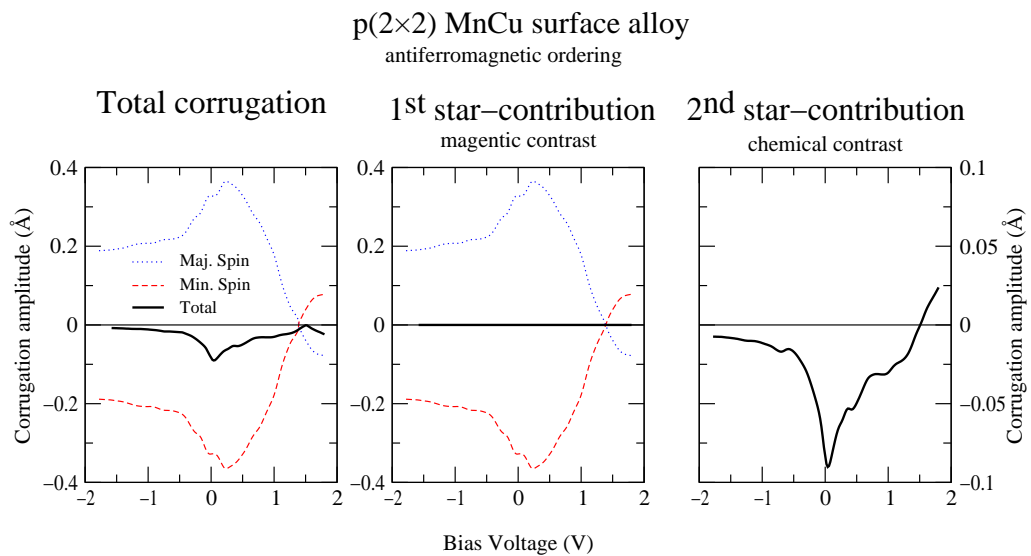


Figure 5.17: Corrugation amplitude obtained for an anti-ferromagnetic ordered $c(2\times 2)$ MnCu surface alloy. The magnetic unit-cell of the system is a $p(2\times 2)$ cell.

In Fig. 5.17 the corrugation amplitude obtained for a relaxed anti-ferromagnetic alloy is plotted. As one would expect, the two different spins strongly contribute to the first star contribution. Using a spin-polarized STM, a technique used in only very few groups [WGG⁺90, Alv95, BGW98], one might be able to detect the $p(2\times 2)$ magnetic structure. This might be possible because of the very strong contribution of up to 0.4 Å of the first star to the corrugation amplitude which distinguishes between the two different Mn positions in the unit-cell.

In the total spin corrugation amplitude summed over both spin contributions, however, these contributions cancel exactly and the second star contribution becomes dominant. Thus, normal STM does not obtain magnetic contrast and the two Mn atoms are indistinguishable. As a comparison with Fig. 5.3 shows, the second star contribution, which shows the $c(2\times 2)$ pattern, agrees with the first star coefficient of the ferromagnetic case. Only at fairly large bias voltages of $U < -0.5$ V or $U > 0.5$ V differences can be found. Thus one can safely conclude that the results presented so far will not be obsolete if an anti-ferromagnetic ordering occurs. This results indicates that one can not deduce the magnetic structure of the alloy from STM images of the $c(2\times 2)$ alloy if a non-magnetic tip is used.

5.6 STS of the $c(2\times 2)\text{MnCu}$ surface alloy

As mentioned in Chapter 4 a scanning tunneling microscope can be used in Scanning Tunneling Spectroscopic (STS) mode as well as in the constant current mode analyzed so far. In spectroscopic mode the applied bias voltage U between tip and sample is varied and the subsequent change in the tunneling current I is measured. In experiments the derivative of the current with respect to the bias voltage is obtained in STS mode. Starting from Eq. (4.21) for the tunneling current in the model of Tersoff and Hamann, one easily obtains the following expression for this derivative of the current

$$\frac{dI}{dU}(U, \vec{r}_0) \propto n_S(eU, \vec{r}_0), \quad (5.7)$$

where again the local density of states of the tip was assumed to be constant.

According to this simple equation, the derivative of the tunneling current with respect to the bias voltage should be proportional to the local density of states of the sample n_S at the position of the tip \vec{r}_0 . Thus, an STS can measure directly the local density of states of the sample. In principle, the STS results are also obtained with a high spatial resolution. However, no atomic resolution can be reached in these experiments due to principle limitations. If the spatial resolution is of the order of

a unit-cell, the uncertainty in reciprocal space must become significant

$$\Delta r \Delta k > \frac{\hbar}{2}. \quad (5.8)$$

This uncertainty in \vec{k} leads to a corresponding energy uncertainty. This effect of the uncertainty principle will substantially reduce the possibility to obtain a detailed image of the local density of states in real space. Because of the small size of the $c(2\times 2)$ surface unit-cell it will not be of any practical significance to include any other than the zeroth star contribution of the local density of states when applying Eq. (5.7) to predict STS images of this surface alloy.

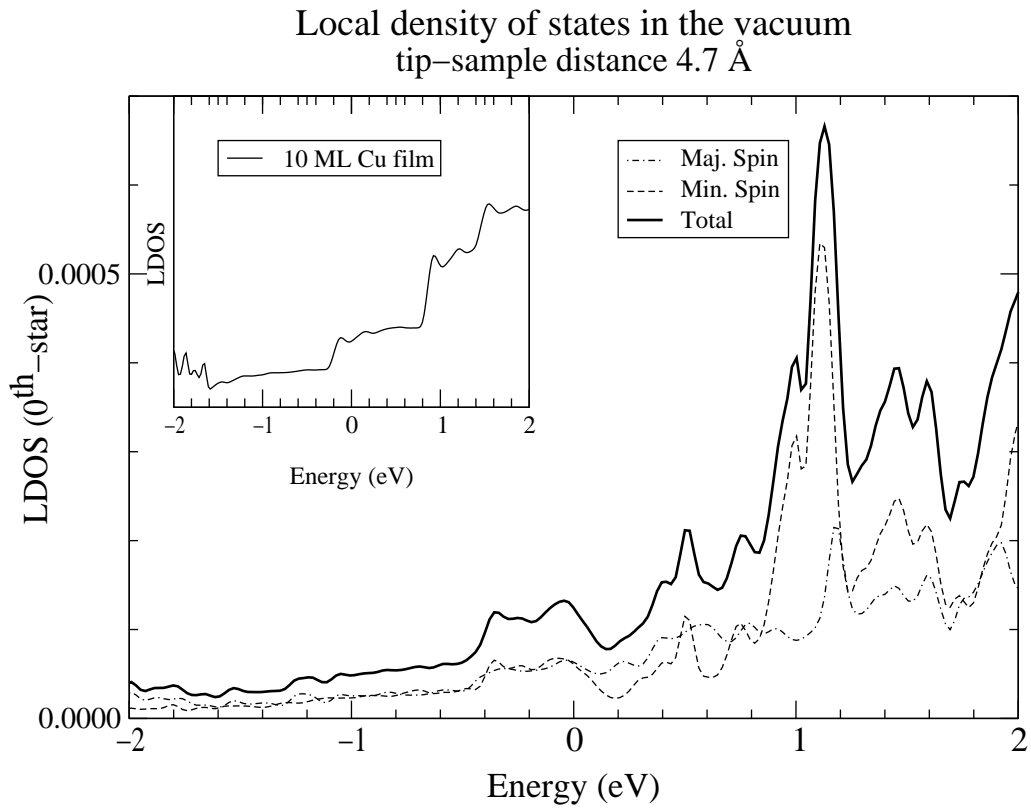


Figure 5.18: Local density of states of the relaxed $c(2\times 2)$ MnCu/Cu(100) surface alloy in the vacuum. The inset shows the local density of states as obtained for a clean Cu surface.

Figure (5.18) shows the local density of states in the vacuum at an assumed tip-sample distance of 4.7 Å. The local density of states increases as the energy of the states involved becomes higher since states with a higher energy will decay slower into the vacuum due to the lower barrier height for these states (remember that the zero of energy was chosen to be the Fermi-level). The exponential increase of the local density of states with higher energy is a rather general feature in these plots.

In an experiment one will measure the same exponential increase for both signs of the applied bias voltage since at higher bias voltages the argument concerning wave-functions which will decay slower into the vacuum will apply to tip states as well as for the sample states. This exponential decay can also be discussed in terms of the change of the barrier which will obvious be symmetric with respect to the applied bias voltage (Fig. 5.19).

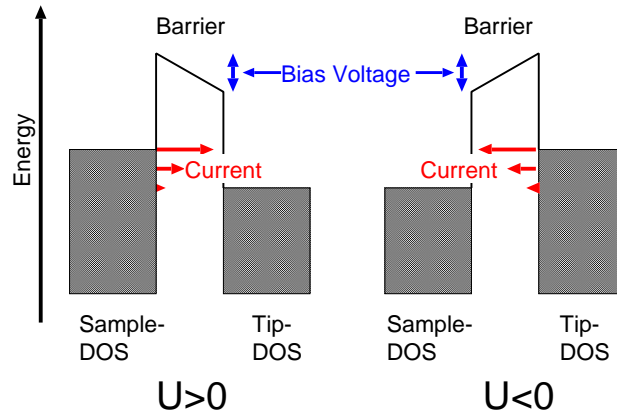


Figure 5.19: Schematic sketch of the vacuum barrier at a positive and a negative bias voltage. The increase of the tunnel current will be roughly symmetric with respect to the bias voltage.

However, since the tip electronic structure is not modeled within the Tersoff-Hamann approach, the increase at negative bias voltages is not described correctly. Furthermore, the general limitations of the Tersoff-Hamann model have to be applied here. The model will become more unreliable at higher bias voltages.

To identify features in the plot which are produced by the alloy one can compare the local density of states for the surface alloy with the corresponding plot for a clean Cu surface as shown in the inset of Fig. 5.18. The local density of states for the clean Cu surface is rather featureless with the exception of several steps at approximately $U = 0$ eV, 1 eV, and 1.5 eV. These steps correspond to the lower edge of Cu s -bands at the $\bar{\Gamma}$ -point of the surface Brillouin-zone. According to the discussion in Section 4.7.2 this \vec{k}_{\parallel} -point will contribute most to the local density of states. These discrete Cu s -bands are a result of the finite film thickness. In a semi-infinite system these levels would be continuous and the local density of states for a plane Cu surface would be smooth without any steps or peaks. This will be discussed in greater detail in the next Chapter.

In contrast to this, the local density of states of the surface alloy shows one very sharp peak at an energy of approximately 1.1 eV. This peak has its origin in the minority spin channel of the local density of states and it can easily be related to

the minority Mn-bands. Thus these calculations indicate that one might be able to resolve the minority spin peak of the Mn-localized density of states in STS. Such an experiment can therefore determine the energy of these states.

The peak does also occur in the STS spectrum of the anti-ferromagnetic structure discussed before even though it is less pronounced. Hence, similarly to the STM results, STS does not depend on the magnetic configuration of the alloy.

Chapter 6

Buried magnetic alloys

Quantum well states in STM and STS

In this chapter some calculations of a buried magnetic two-dimensional alloy will be presented. While the $c(2\times 2)$ alloy discussed in the last chapter was a surface alloy, this chapter will try to answer the question whether it is possible to detect magnetic structures underneath the surface.

While it is well known that defects, especially charged defects, in semiconductors can be detected by STM even if they are buried more than 50 Å below the surface, in metals one normally assumes that the screening by the nearly free electrons is very effective and that defects a few layers below the surface become not detectable by STM. Therefore, it was quite surprising that some recent publications [SHV96, AMC97, ACM98, HAB⁺99] claimed to be able to detect buried structures.

Most experimental groups worked on single defects or defects without any ordering. However, there exist several interesting results of STM and STS experiments on systems showing relatively ordered structures [AMC97, ACM98, HAB⁺99]. In this context the results of Altfeder *et al.* [AMC97, ACM98] are extremely surprising. This group presented STM and STS images in which they claimed to detect the (7×7) surface reconstruction of the Si(111) surface through as much as 100 Å of Pb.

This chapter will be split into three main sections. First calculations of the corrugation amplitude for the surface and the subsurface alloys will be presented. In that section the alloy will be covered by up to three monolayers of Ag. Then, the STS results of these systems will be discussed shortly. In the last section, which is the longest, the STM corrugation amplitudes for systems containing a deeply buried

alloy will be presented and a interpretation of these results in terms of quantum wells will be discussed.

6.1 Buried $c(2\times 2)$ MnAg alloys

In this section a buried $c(2\times 2)$ two-dimensional alloy will be studied. It will be investigated whether it is possible to detect a similar alloy, as the previously investigated $c(2\times 2)$ MnCu/Cu(100) surface alloy, with the STM even if it is no longer a surface alloy but covered with additional monolayers of bulk material.

The system used for this investigations is not the Mn/Cu(100) system discussed in the previous chapter, but the Mn/Ag(100) system. Experimental findings are quite similar to the Mn/Cu(100) case. At a coverage of 0.5 monolayer of Mn the formation of a $c(2\times 2)$ structure was reported by [SKHG97, SKHG98, SKMC⁺99]. However, this system seems to be instable as a surface alloy [SKHG97]. The Mn tends to diffuse into the substrate. Previous FLEUR results from R. Abt [AB98] indicated that the alloy might indeed be more stable when covered by additional Ag layers. If at all possible, it will of course be extremely difficult to create a buried two-dimensional $c(2\times 2)$ MnAg/Ag(100) alloy. However, this system can be used as an extremely instructive example on how the STM might be able to detect ordered buried interface structures. Thus the careful investigation of this systems will give important ideas how to interpret STM images of buried structures.

As in the last chapter, all calculations presented here are obtained by using 36/91 \vec{k}_{\parallel} -points in the irreducible wedge of the two-dimensional Brillouin zone. Again the local spin density approximation is used and the basis set contains approximately 100 functions.

6.1.1 The $c(2\times 2)$ MnAg surface alloy on Ag(100)

Since silver and copper are isoelectronic, one might expect little differences in the MnAg system compared to MnCu. As one can see from Fig. 6.1, the corrugation amplitude for both alloy systems shows the same features. Again the first star contribution dominates the total corrugation amplitude and again this is due to the minority spin contribution. The first star contribution is negative and consequently not the Mn but the Ag positions will be imaged as protrusions in the STM. The corrugation amplitude as shown in Fig. 6.1 does already take the surface relaxation into account which is very small in this system. Unlike the Mn atoms in the

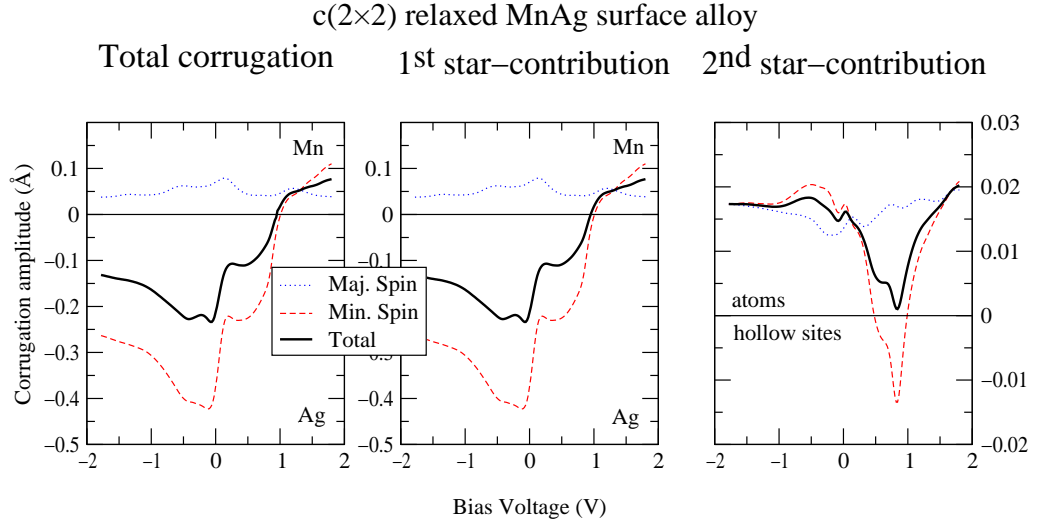


Figure 6.1: Corrugation amplitude of the $c(2 \times 2)$ MnAg/Ag(100) surface alloy at a tip sample distance of 4.6 Å.

$c(2 \times 2)$ MnCu/Cu(100) alloy, the Mn atoms in this MnAg alloy are located nearly at their ideal lattice positions. The Mn-relaxation has been calculated by R. Abt [Abt] to be only -0.04 Å in this system. The minus sign means, that the Mn atoms relax inwards in this alloy. This is due to the increased Ag lattice constant of 4.01 Å as compared to 3.61 Å for Cu. The Mn atoms are already well separated at their ideal lattice positions. An additional relaxation leads hardly to any further increase of the magnetic moment and a lower energy. This also can be deduced from the higher magnetic moment of $4.1 \mu_B$ obtained here as compared to $3.84 \mu_B$ for the MnCu alloy.

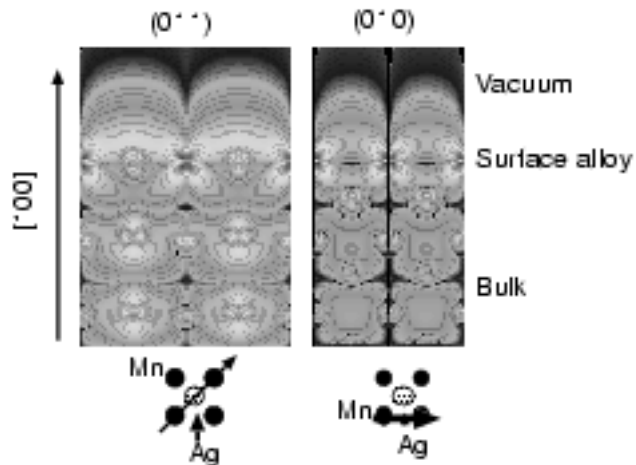


Figure 6.2: Local density of states of a single minority spin state. The state is chosen from a band just below the Fermi-energy (-0.07 eV) at the \bar{X} -point of the two-dimensional Brillouin zone.

The electronic structure of the system is analogous to the MnCu system. Figure 6.2 shows the local density of states for a single state. A comparison of this figure with Fig. 5.11 reveals that the discussion of the Mn-localized states spanning over the adjacent substrate atom of the surface presented in the last chapter remains valid for this system as well. The very same states at the \bar{X} -point of the surface Brillouin zone just below the Fermi energy exist and these states are responsible again for the high chemical contrast in STM.

6.1.2 Subsurface MnAg alloys

The calculated corrugation amplitude as obtained by covering the surface alloy by additional layers of Ag is displayed in Fig. 6.3. In these calculations the total film thickness remains constant at 11 layers. The position of alloy layers at both sides of the film was changed from the subsurface layer to deeper positions.

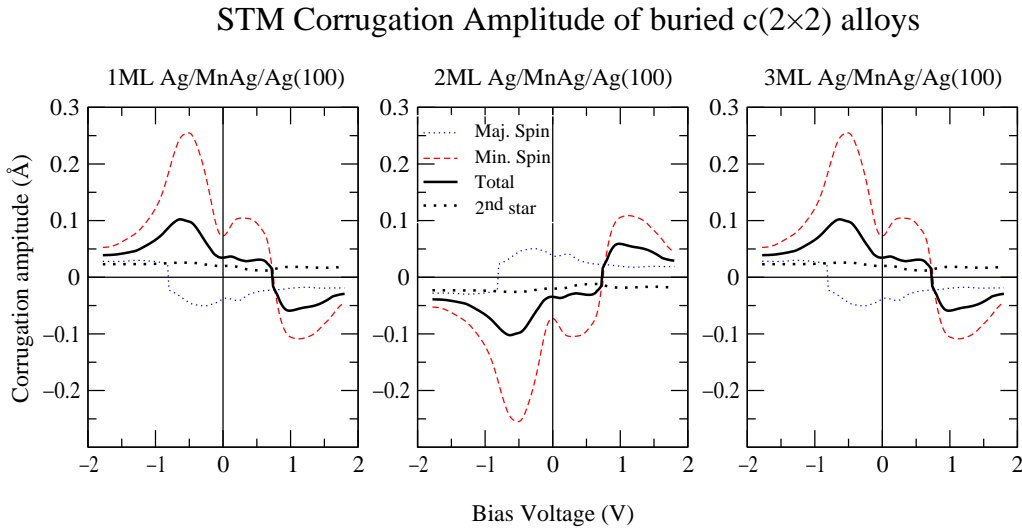


Figure 6.3: Corrugation amplitude as obtained for buried $c(2\times 2)$ MnAg alloy layers. The plot at the left shows the corrugation for a subsurface alloy, the plot in the middle the corrugation for the alloy in the third layer and the plot at the right the corrugation for the alloy buried under three layers of Ag. In all plots the total contribution of the second star is indicated by the dotted line.

Two most striking observations can be made: (i) the value of the total corrugation amplitude does not become much smaller with increasing thickness. (ii) the corrugation amplitude remains dominated by the first star contribution. This means that an STM image of such a buried alloy will in fact not show the $p(1\times 1)$ surface unit-cell but a clear $c(2\times 2)$ pattern will still be visible in STM images. This does not correspond to conventional wisdom which always assumes that the local density of states will essentially follow the nuclear charge of the surface atoms and that

therefore only the surface can be imaged in STM. In this system the local density of states seems to be dominated by states which strongly break the symmetry of the surface.

At this point a short discussion of this symmetry breaking will be useful. In the $c(2\times 2)$ unit-cell of the alloy mirror planes through the Mn atoms exist. For $\vec{k}_{\parallel} = (0.5, 0)$, i.e. for the \bar{X} -point of the Brillouin zone, the Hamiltonian is symmetric with respect to this mirror plane if one also takes the translational symmetry into account. Therefore the eigenstates can be classified to be either odd or even with respect to this mirror plane. Because of the additional translational periodicity the odd state will be zero at all Mn positions and it will have a maximum in between, i.e. at Ag positions (strictly speaking, this is only true for its square, which however is the quantity of importance here), the even state on the other hand will have a maximum at the Mn positions. If one now assumes the alloy layer to be absent, i.e. if one looks at a pure Ag crystal, these two states will be degenerate. The additional translational symmetry of the $p(1\times 1)$ unit-cell of the pure Ag(100) surface transforms an odd into an even state and therefore these two states are degenerate. The presence of the Mn in the alloy layer breaks this symmetry and the states are no longer degenerate. Since the odd states give raise to a negative contribution to the first star coefficient of the local density of state and the even states to a positive, a nonzero contribution to the first star coefficient of the local density of states can only occur if these two states are not degenerate.

In the case of the $c(2\times 2)$ MnCu/Cu(100) alloy, dealt with in Chapter 5, the states just below the Fermi energy, which induced the large corrugation obviously have odd symmetry with respect to the mirror plane described above. States with even symmetry contribute only at higher energies. These states are responsible for the change in the sign of the corrugation amplitude at higher bias voltages and were responsible for the change of the sign of the corrugation amplitude at higher bias voltage.

Figure 6.3 can now be interpreted in terms of this short symmetry analysis. As stated above, the fact that the first star contribution dominates the corrugation amplitude for these alloys indicates a strong symmetry breaking. Hence, similarly to the situation for the surface alloy, the odd and even states must be different in energy even for the buried alloy. However, the sign of the corrugation amplitude changes with every additional substrate layer. This indicates that the character of the states lower in energy change from symmetric with respect to the mirror plane to anti-symmetric.

Figure 6.4 shows the local density of states for a single state of the subsurface alloy.

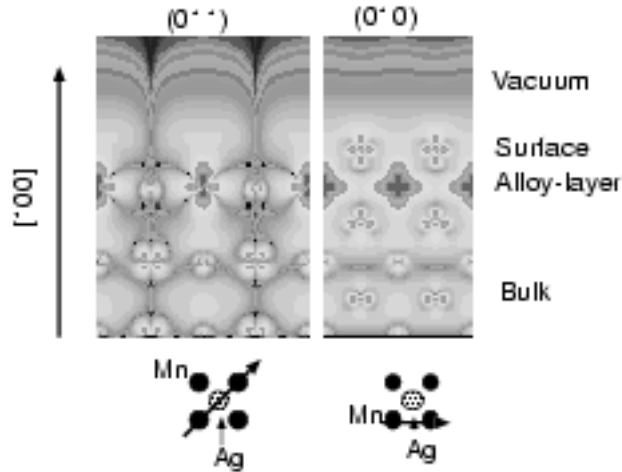


Figure 6.4: Local density of states of a single minority spin state for the subsurface alloy system. Note that the shape of the wave-function changed drastically near the Mn atoms as compared to Fig. 6.3.

The state is chosen from the \bar{X} -point of the surface Brillouin-zone and its energy is slightly smaller than the Fermi-energy (-0.08 eV). It is clearly visible, that in this alloy the state symmetric with respect to a mirror plane through the Mn-positions spreads out far into the vacuum and therefore in this alloy these states dominate the corrugation as observed in STM. Obviously, the additional Ag layer on top of the alloy makes these even states energetically more favorable than the even state.

For the subsurface and perhaps also for the alloy covered with two monolayer of Ag the strong symmetry breaking in the vacuum might be explained in terms of hybridization d -like orbitals of the Mn with Ag orbitals. However, this explanation becomes definitely unsuitable for more deeply buried layers because such effects should decay exponentially with increasing coverage. I will come back to this question of the STM corrugation amplitude of deeply buried alloys in later in this chapter.

6.2 Scanning tunneling spectroscopy of buried alloys

Since the buried alloy layer can be detected in topographic mode, one might expect that the buried alloy also affects the STS spectra.

Figure 6.5 shows the zeroth star contribution to the local density of states for both the surface alloy and the buried alloys. As explained in Section 5.6 this zeroth star contribution is proportional to the signal seen in an STS dI/dV spectrum. The

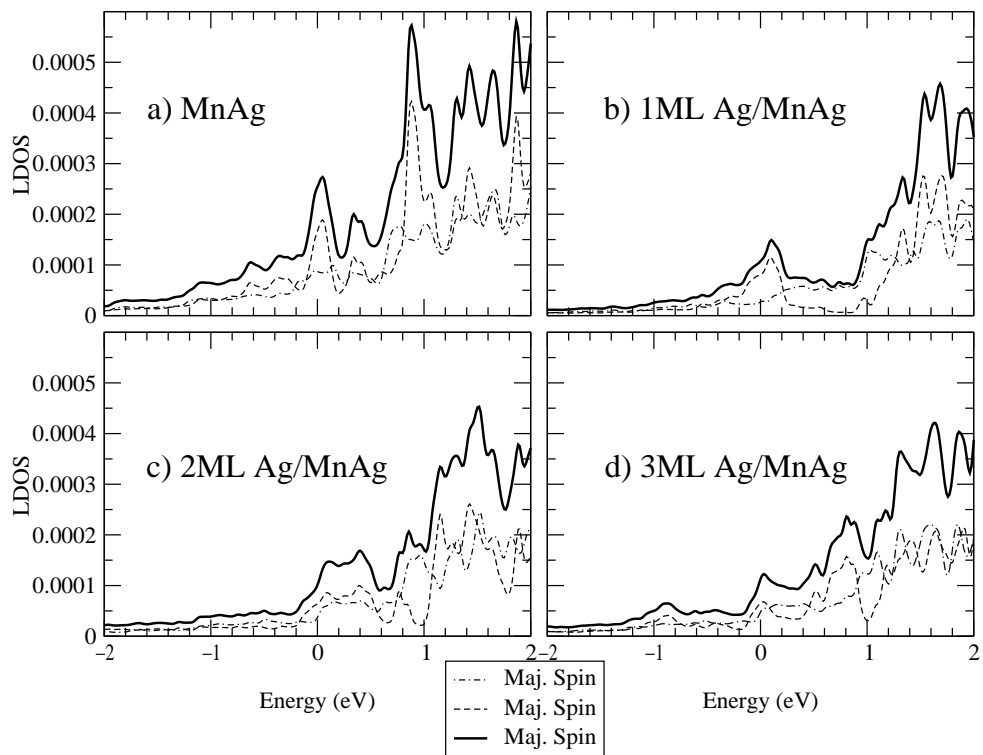


Figure 6.5: STS spectra for MnAg alloys. The upper left (a) plot shows the result for the surface alloy. The upper right (b) the spectrum for the subsurface alloy and the lower plots the spectra as obtained for the alloy buried under 2 (c) and 3 (d) monolayer of Ag.

spectrum of the surface alloy therefore will show two peaks. Some minority states directly at the Fermi level do contribute to a peak at a bias voltage of 0 V in STS. Furthermore, the same peak as calculated for the MnCu surface alloy at a bias voltage of approximately 1 V can be observed. This peak obviously again is due to the minority spin Mn states at these energies.

Comparing the STS spectrum of the surface alloy (Fig. 6.5a) with the spectra for the buried alloys (Fig. 6.5b-d) clearly shows that these two peaks in STS decay rapidly with increasing coverage. The peak at approximately 1 V totally disappears even at a coverage of only one monolayer. In fact, for this coverage the minority spin contribution becomes smaller than the majority one at around 1 V. The peak at small bias voltages is strongly reduced in intensity and this peak disappears at a coverage of two monolayer of Ag. At and above this coverage, the two spin contributions are roughly equivalent, except for small deviations which can neither be called reliable results nor will be detectable in experiments.

Fact that the peak at 1 V can only be detected for the surface alloy while the peak at 0 V can be seen for the subsurface alloy as well can be explained from the electronic structure. The states responsible for these peaks have \vec{k}_{\parallel} -values from different parts in the surface Brillouin zone. This can be deduced from the band-structure of the subsurface system as seen in Fig. 6.6. This band-structure shows that very similarly to the MnCu band-structure discussed in the previous chapter (Fig. 5.5) the bands containing states with a high localization at the Mn atoms lie near the Fermi energy only at higher $|\vec{k}_{\parallel}|$ values, at the $\bar{\Gamma}$ -point these bands lie well above 0.5 eV.

Therefore the peak at 1 V in STS obviously is due to these bands at 1 eV above the Fermi-energy at the $\bar{\Gamma}$ -point. These states are highly localized at the Mn positions. The low dispersion at $\bar{\Gamma}$ shows that the hybridization with Ag states is low and therefore they do not contribute to the STS spectrum if they become buried. The STS peak directly at the Fermi-energy obviously is not due to states from $\bar{\Gamma}$. That explains why the peak is that broad and not very high. This peak is induced by states not from the vicinity of the $\bar{\Gamma}$ point, which no longer have pure Mn *d*-character but already hybridize strongly with the Ag states. Hence, the peak at around the Fermi-energy can be detected for the subsurface as well as for the surface alloy.

The STS result for the alloy covered with two monolayers of Ag will not differ from the results for pure Ag. The STS is not sensitive to the buried $c(2 \times 2)$ MnAg alloy layer. In this respect the STS and STM differ substantially. This will be explained in the next sections by investigating states from the \bar{X} -point of deeply buried alloys which will contribute strongly to the corrugation observed in STM.

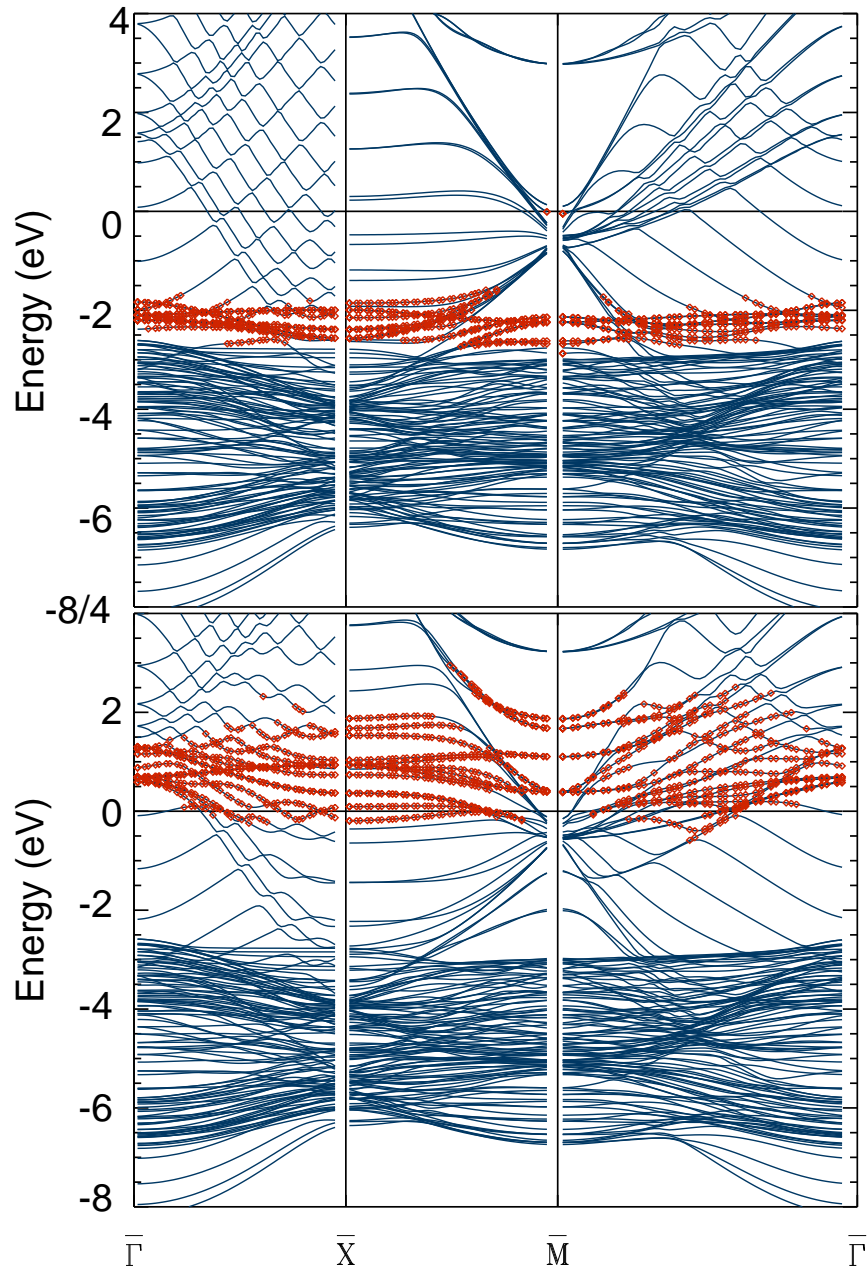


Figure 6.6: Band-structure of the subsurface $c(2 \times 2)\text{MnAg}/\text{Ag}(100)$ alloy. States which are localized by more than 40 % in the Mn muffin tin-spheres are marked.

6.3 Imaging the deeply buried alloy

In the next sections the surprising ability of the STM to resolve buried structures will be investigated further and it will be shown, that the formation of quantum well states leads to the possibility to detect the alloy even under thicker Ag films. In order to investigate this I will first present some general considerations concerning quantum well states and then I will briefly discuss the computational problems which occur when one wants to simulate deeply buried alloys. Afterwards the results will be presented.

6.3.1 Quantum wells

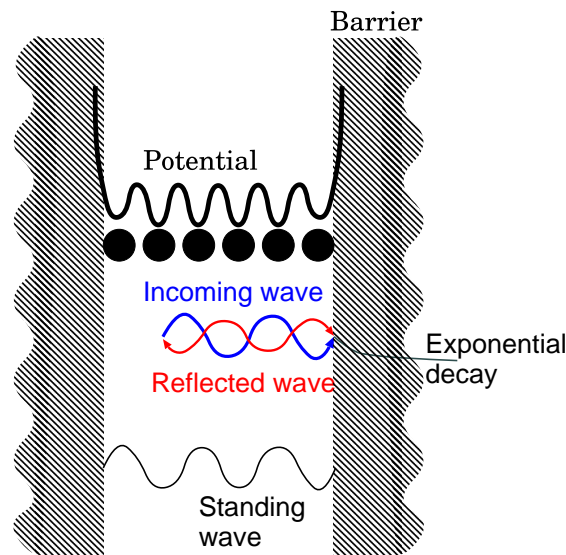


Figure 6.7: Basic setup of an quantum well system. The high potential barriers at both sides restrict the wave-function so that it is localized inside the well. This leads to the formation of standing waves, i.e. to the formation of a set of solutions with discrete energies.

Before further results are presented, I will shortly discuss the formation of states in quantum wells. The basic setup of a quantum well is shown in Fig. 6.7. The systems under consideration in this work can be regarded as two-dimensional quantum well systems. A thin metallic film, in which the electrons can be considered as free, is limited by two potential barriers at either side. These barriers confine the electrons inside the metal in the direction perpendicular to the film (z -direction). The motion of the electrons remains unrestricted in the two other directions of space parallel to the film.

If the barrier potential is fairly localized, the electron wave-functions are known to be composed of two Bloch-waves with $k_{z,1} = -k_{z,2}$, i.e. of an incoming and a reflected wave, forming a standing wave with respect to the z -direction inside the thin metal film. The assumption that the barrier is localized, i.e. that it does not influence the potential inside the film, opens the possibility of determining the energy-levels of the quantum well-states from bulk properties. The conditions of the formation of a standing wave introduces an additional condition on the value of k_z used in the composition of the standing waves. The wave-numbers k_z have to be chosen such that the wave is periodic within the metal-film. For the ideal case of an infinitely high barrier this leads to the condition

$$k_z = \frac{2\pi}{z_0} \times n, \quad (6.1)$$

where z_0 is the thickness of the metal film and n denotes an integer number.

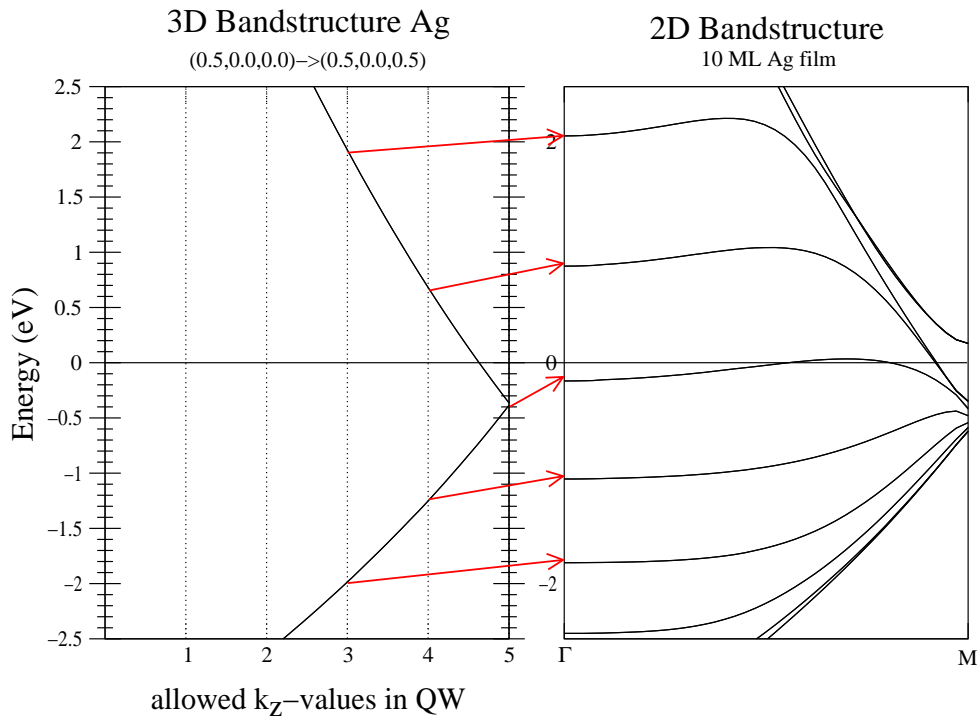


Figure 6.8: Plot of the three-dimensional and two-dimensional Ag band-structure along line from X to M and from \bar{X} to \bar{M} respectively. The three-dimensional bulk unit-cell already contains four atoms, i.e. two layers. Therefore, only the five indicated k_z -values are allowed for a quantum well of ten layers.

Using a bulk band-structure of the metal these k_z -values can be connected to the energy-values of the quantum well states. As Fig. 6.8 shows for the example of a 10 monolayer film, the different allowed k_z -values lead to discrete bands in the two-

dimensional band-structure of the film. The left plot shows a single s -band from the X to the M point of the 3D Brillouin zone. The unit-cell is chosen to be not the primitive but conventional fcc unit-cell with four atoms per unit-cell. Therefore this structure can be easily related to a $c(2 \times 2)$ surface band-structure as shown on the right. The band shown in the left plot is projected onto the \bar{X} -point of the surface band-structure. However, the finite film thickness leads to the formation of quantum well states which can be found at the energies corresponding to the allowed k_z -values marked in the left band-structure shown in Fig. 6.8. The slight shift to higher energies of the actual quantum well-states is probably due to the influence of the vacuum which does not form a perfect impenetrable barrier and also affects the potential of the surface layers. The potential in the surface region will be slightly higher as for the bulk and therefore also the states will have higher energies as compared to their ideal values deduced from the bulk band-structure.

One easily realizes from Eq. (6.1) that the allowed values of k_z become denser in k -space if the film gets thicker. In the limit of an infinitely thick film which would be a bulk material, one obtains a two-dimensional band-structure which is the two-dimensional projection of the three-dimensional one. In this limit the bands in the two-dimensional band-structure are dense.

Applying this simple discussion to the film geometry used in **FLEUR** one realizes that all the surface calculations presented so far, in fact are calculations of a quantum well system, since the film-geometry implements a thin metal film limited by the vacuum barrier at either side. However this thin film will model bulk properties reasonable well if it is thick enough and if therefore the bands become dense enough.

To calculate STM images of a buried structure one now introduces an additional interface into the film. This makes the situation much more complicated. For example, in the MnAg-alloy covered by three monolayers of Ag presented in the last section several quantum well systems could be identified. The whole film of 11 layers obviously is a quantum well of 11 layer thickness. But one could also call the three Ag layers between the surface and the alloy a quantum well, if the reflection of electrons due to the potential variation at the alloy layer is large. Similarly the three remaining substrate Ag layers at the center of the slab could form a quantum well. However, this interpretation assumes that the reflectivity at the alloy layer is sufficiently large.

Because of the possibility of the formation of several quantum wells in the system one has to be very careful about the interpretation of the results to make sure that the effects arising from the finite film thickness can safely assumed to be neglectable for the results. Thus, I will now discuss the different setups used for the calculation

of these deeply buried alloys in which quantum well effects may occur.

6.3.2 Calculation of deeply buried alloys

In the choice of an appropriate setup to calculate the STM properties of deeply buried alloys one has to keep several problems in mind. In particular, the film thickness has to be kept small since the computational effort will increase approximately with the cube of the film thickness if the number of basis-functions per atom is kept constant. Furthermore one has of course try to avoid interactions between the two alloy layers used in a symmetric setup. For example, it is not obvious whether the 11 layer setup presented in Section 6.1.2 will lead to correct results. In this geometry the two alloy layers are separated by only three Ag layers in the center of the film. These three alloy layers are probably no longer a sufficient approximation of a bulk crystal and additional interactions between the MnAg alloy layers may occur, which modify the result.

For thicker Ag films between the alloy and the vacuum the 11 layer setup used so far obviously is no longer sufficient. Two different approaches can be used to obtain results for deeply buried alloys. Only one alloy layer could be used. This layer is positioned in the center of the film. This approach therefore drops the Ag layers which should model the bulk which is justified when the potential in the Ag layers between the alloy and the vacuum is already close to the Ag bulk potential. Since this setup will use only one single alloy layer, no interaction between the alloy layers can occur. The second possible setup still uses two alloy layers with some additional Ag layers in between which model the substrate. This can only be done for the alloy covered by three monolayers, because of the restriction of overall film thickness.

Summarizing, for the investigation, whether it really could be possible to detect the $c(2\times 2)$ alloy covered by an even thicker Ag film, the following setups were used:

1. an 11 layer film with the alloy layer covered by 3 Ag layers and 3 Ag layers in between the alloy (see previous section),
2. a 21 layer film with the alloy layer covered by 3 Ag layers and 13 Ag layers in between the alloy,
3. an 11 layer film with the alloy layer at the center layer, i.e. an alloy layer covered with 5 layers of Ag,

4. a 9 layer film without inversion, the alloy layer covered with 5 layers of Ag at one side and 3 layers at the other side,
and
5. a 21 layer film with the alloy at the center layer, i.e. a alloy layer covered with 10 layers of Ag.

These systems allowed me to check the influence of the film thickness on the results. The STM corrugation amplitude for an alloy covered by three monolayer of Ag was obtained from systems (1), (2), and (4). The comparison of this results should allow one to rule out interaction effect of the two alloy layers.

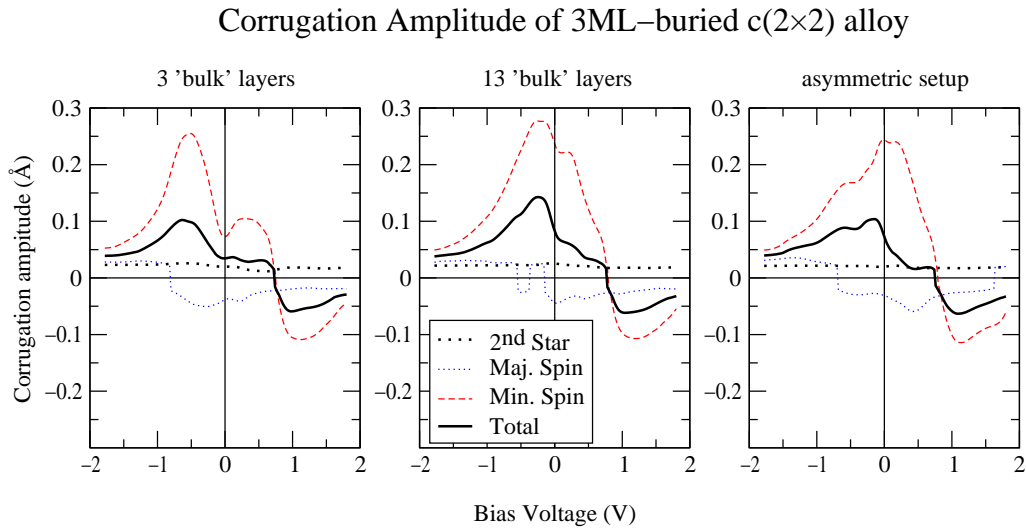


Figure 6.9: Comparison of the the corrugation amplitude obtained by different film setups for a $c(2\times 2)$ MnAg covered by three monolayers of Ag. The left plot shows the results as obtained for setup (1), the plot in the middle the results for setup (2) and the right results are obtained from setup (4).

Figure 6.9 shows the corrugation amplitude as obtained for a $c(2\times 2)$ MnAg alloy buried under three monolayers of Ag. In all setups the corrugation amplitude is dominated by the first star contribution. As one can expect, this first star contribution mainly arises from the influence of the minority spin. The minority spin contribution to the first star coefficient has a positive sign for bias voltages smaller than approximately 0.8 V and changes sign above this voltage. However, both the positions of the peaks and their relative height are different for the four setups. This is a sign of the influence of the different film-thicknesses. Thus, one cannot deduce the exact position and the height of the peaks from these results. In the next section it will be shown that the exact band energy can have a huge influence on

these properties. The band energies depend on the film thickness as discussed in the previous section. However, one has to conclude that two main results are obtained in all setups: the first star coefficient is still dominating the corrugation amplitude and the sign of this contribution is described consistently in all setups.

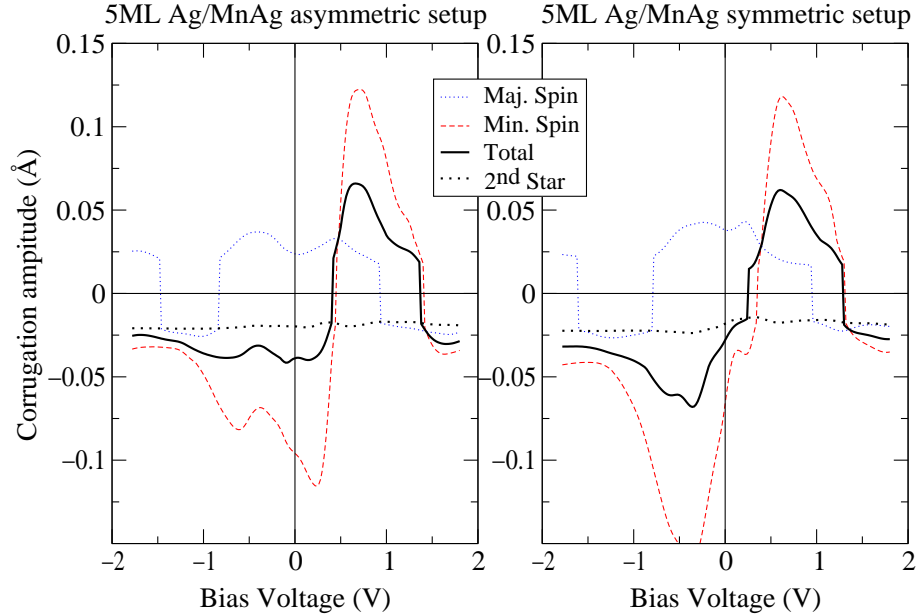


Figure 6.10: Corrugation amplitude for a $c(2 \times 2)$ MnAg covered by 5 monolayers of Ag. The left plot was obtained from setup (4) and the right plot from setup (3).

A comparison of systems (3) and (4) showed how far one could use the symmetric film with the alloy in the middle to investigate the properties of a alloy buried under very thick Ag films.

Obviously, a setup with only one MnAg alloy layer in the center is a very effective setup as far as the aim of limiting to the total number of layers in the film is concerned. Comparing the corrugation amplitude plot for setup (3) with the plot for setup (4) (Fig. 6.10) leads to very few differences. Similarly to the different three layer setups the peak positions are shifted with respect to the bias voltage, but both the sign and the order of magnitude of the corrugation is equivalent in both setups. This result justifies the use of the symmetric setup. The alloy at the center position does not lead to substantially different results compared to a non symmetric position.

6.3.3 The film as a model of the semi-infinite crystal

At this point it is instructive to discuss in some detail how far the film geometry used in the FLEUR program could be used to model the true semi-infinite system as

realized by the surface of a bulk crystal. The aim of this section is to understand, why the peak positions and heights change for the different setups presented in the previous section.

One usually assumes that the film model will be a good approximation to the semi-infinite system if the potential or the electron charge density of the center layers are close to their bulk values. If one considers the self-consistency process as described in Chapter 2 this will ensure that the charge density in the surface region obeys the correct boundary conditions both at the vacuum side and the bulk side. Therefore, most results of the film setup should describe the semi-infinite system sufficiently well if the film is thick enough to ensure a bulk like potential in the center layers.

However, one important point, which will be of central importance for the application of the film setup to the interpretation of STM results as it is done in this work has to be stressed. As described in Chapter 4 the structure of the local density of states in the vacuum is determined by only few single particle wave-functions. As stated above, the film setup implements a quantum well which restricts the wave-vector of the wave-functions perpendicular to the surface. This leads to the quantization of energy levels described above. One has to realize that this quantization of allowed energy levels is artificial. In a true semi-infinite crystal these discrete energy levels become part of a continuous energy range. Thus, for the quantities discussed here, the fact that the charge density becomes bulk-like in the center of the film is not sufficient to ensure that the film-setup models the semi-infinite crystal correctly.

The discrete energy levels sometimes lead to artifacts in the results. An example for this can be found in Fig. 6.11 which was already discussed shortly in Section 5.6. In the STS spectrum of a 10 layer Cu film shown in the lower panel of Fig. 6.11, one can spot steps at approximately -1.4 V, -0.2 V, 0.8 V and 1.5 V. The upper plot of Fig. 6.11 shows the band-structure of the same system in the same energy range along a line from the $\bar{\Gamma}$ -point to the \bar{X} -point of the surface Brillouin-zone. The steps in the STS spectrum always occur at energies at which an additional Cu band start to contribute to the tunneling process. This result is reasonable for a 10 layer Cu film. If one performs STS measurements on the surface of a Cu bulk however, these discrete energy levels will not occur and the STS spectrum will be smoother. It will roughly correspond to the spectrum shown in Fig. 6.11 with the steps smeared out.

This example indicates which results obtained from film calculations cannot be trusted. As soon as the exact position of the bands will be of importance and as soon as an energy smearing of the order of the separation of the bands will de-

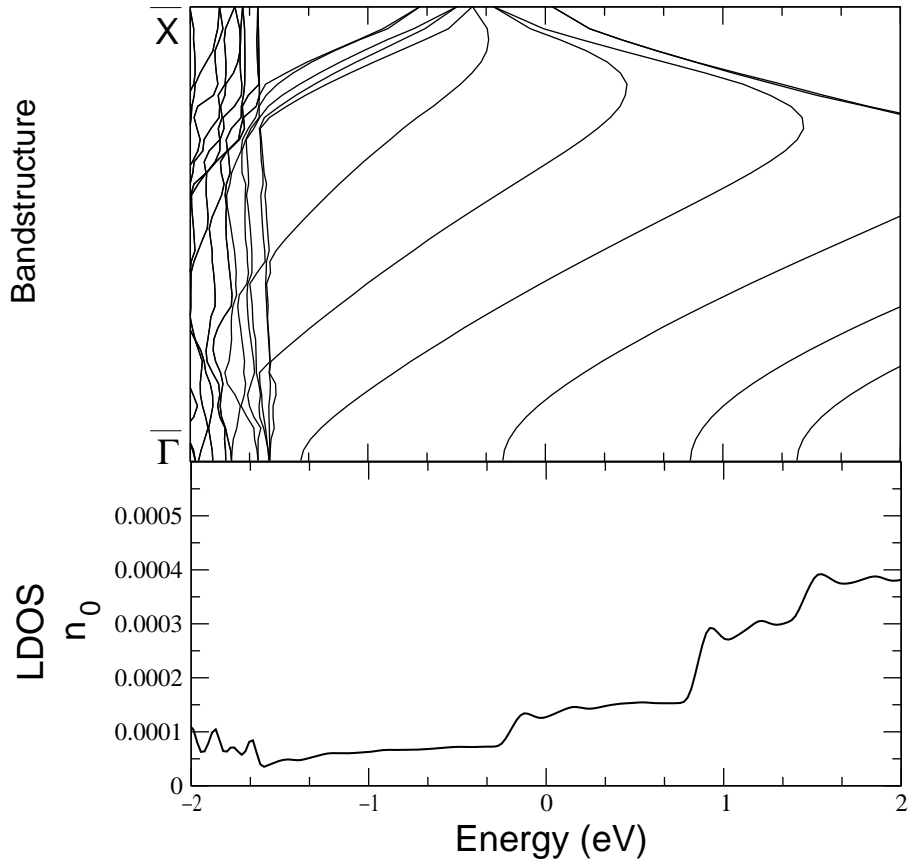


Figure 6.11: The lower part of the plot shows an STS spectrum of an 11 layer Cu(100) film. The upper half of the plot the corresponding part of the band-structure.

stroy the results one has to be very careful and in general one cannot expect these results to be correct for a semi-infinite crystal as well.

The MnCu results of the previous chapter obviously are not affected by the finite film thickness since all effects discussed there were independent on the exact position of the Cu band energies. However, in the discussion of deeply buried structures one has to keep this problem of finite film thickness in mind as the discussion of the majority spin contribution in the next section will show.

6.3.4 STM images of deeply buried $c(2 \times 2)$ MnAg alloys

The first indication that the formation of a quantum well may be the origin of the imaging of the buried $c(2 \times 2)$ alloy layer is the possibility of detecting the alloy even if it is buried under three monolayers of Ag. If this hypothesis of the formation of a quantum well is correct, it should be possible to detect the alloy if it is covered by even more Ag.

If quantum well-states are formed the corrugation amplitude, showing the $c(2 \times 2)$

structure should become independent from the number of Ag layers on top of the alloy. At least no exponential decay should be observed.

In the following two sections the different spin contributions to the local density of states in the vacuum at a distance of approximately 4.7 Å will be discussed in great detail for a $c(2\times 2)$ MnAg alloy layer covered by 10 monolayers of Ag.

6.3.4.1 Majority spin contribution

Figure 6.12 shows a part of the majority band-structure and the first star contribution to the majority local density of states for the $c(2\times 2)$ alloy buried under 10 monolayers of Ag. Most interesting are the pairs of bands which cross the \bar{X} -point at for example -0.2 eV or -0.7 eV. These bands will be degenerate at this point (and along the whole line from \bar{X} to \bar{M}) if no alloy is present. The symmetry breaking induced by the alloy destroys the degeneracy and the two bands become slightly different in energy. One of the bands will contain states which are symmetric with respect to a mirror plane through the Mn atoms and the other band will contain states which are anti-symmetric. These two types of states would be equivalent if no alloy is present, but now these states can contribute to the first star coefficient of the local density of states in the vacuum. It can be seen from this first star contribution in Fig. 6.12 that obviously the two bands contribute with a different sign. This is exactly what is expected. The band which corresponds to symmetric wave-functions with respect to the mirror plane through the Mn atoms will show the Mn positions as protrusions leading to a positive contribution and similar the antisymmetric states will contribute with a negative sign.

However, and this is important to notice at this point, these oscillations in sign will not be observable in an experiment. This small energy-splitting of one degenerate pure Ag band into two bands in the alloy case will occur at every of the Ag bands. In the calculation as presented here, the bands are separated by nearly 0.5 eV. As explained above, these discrete set of bands will turn into a continuous set in the case of a true semi-infinite crystal. Therefore the contribution to the first star coefficient of the local density of states of the bands with different symmetry will cancel. The oscillations seen in the majority spin contribution to the first star coefficient of the local density of states are therefore purely artificial results produced by the finite film thickness.

The majority spin should not lead to a significant contribution to the first star coefficient of the local density of states in the vacuum. This will be an important

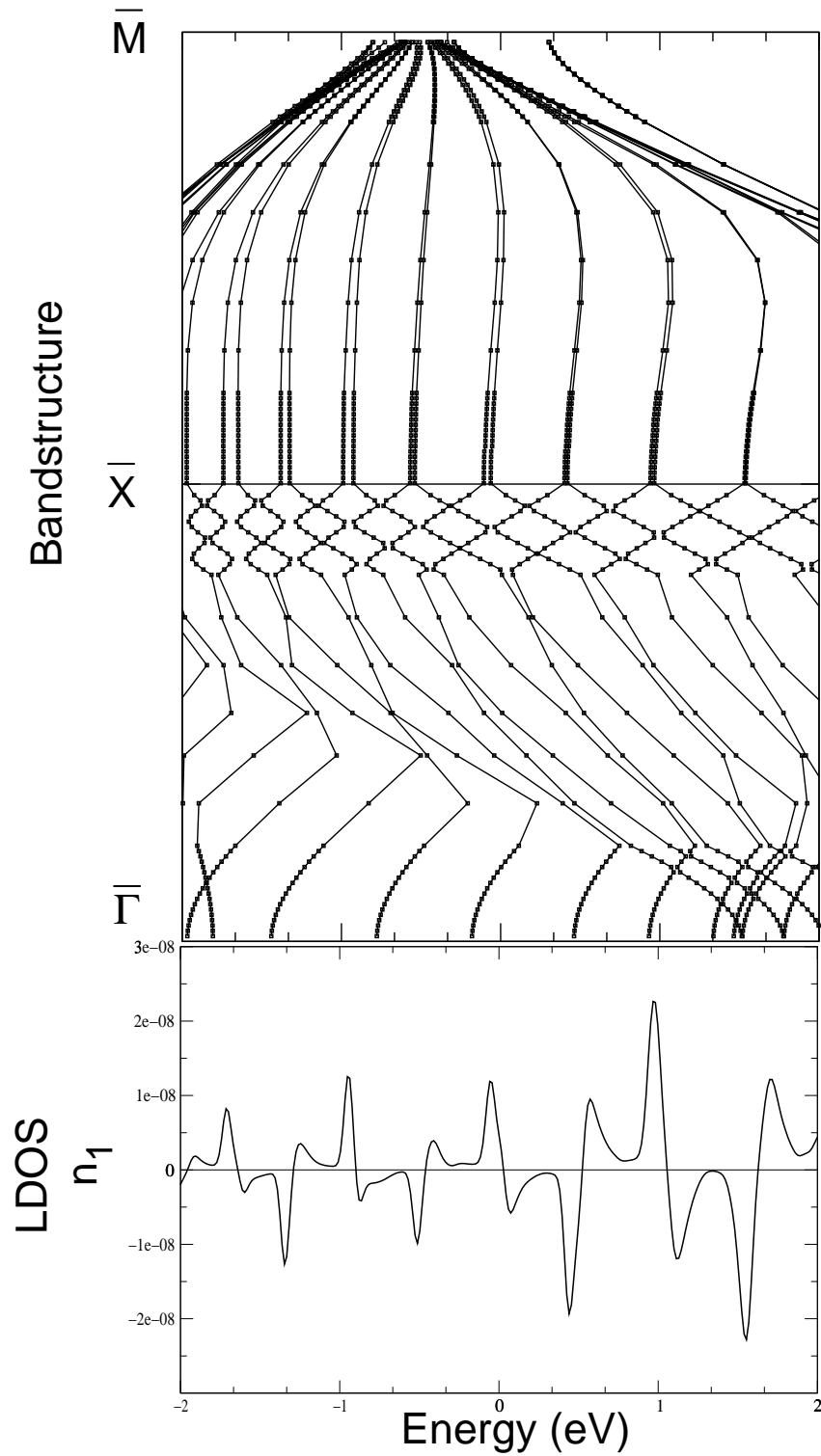


Figure 6.12: Majority band-structure and majority first star coefficient of the local density of states. The first star contribution is dominated by states at the \bar{X} -point in the Brillouin zone. In this context the oscillations in the local density of states can be easily related to the flat bands stretching from \bar{X} to \bar{M} .

result to keep in mind for the discussion of the corrugation amplitude for this buried alloy in Section 6.3.4.3.

6.3.4.2 The minority spin contribution

I will now discuss the minority spin contribution to the local density of states. It will be shown that the strong first star contribution to the local density of states can be explained by the influence of the minority spin and the formation of a quantum well will be identified to be the origin of this.

Figure 6.14 shows the band-structure for the minority spin. The following discussion will focus on the states near the \bar{X} -point of the surface Brillouin-zone since the first star contribution to the corrugation will be investigated and since states from this point will dominate this contribution.

Two different band-structures are displayed in Fig. 6.14. The bold black lines correspond to results obtained for a buried $c(2 \times 2)\text{MnAg}$ alloy covered by 10 monolayers of Ag. The points connected by thin lines describes the band-structure of a film of 10 monolayers of pure Ag, i.e. for a 21 layer system. It will be shown that the contributions of different states of the alloy system to the local density of states in the vacuum and therefore to the corrugation can be interpreted with the help of this second film of 10 monolayers of Ag.

The system describing the buried alloy consists of a total of 21 layers, of which 20 are pure Ag layers. Therefore, the states will be quantum well states of this 21 layer quantum well. In the majority spin band-structure presented in the last section one could easily identify these quantum well states at energy levels of a pure 21 layer Ag film. In that spin contribution the small symmetry breaking effect of the alloy only was visible by very slight energy shifts of the two degenerate 21 layer Ag levels. In the minority spin the splitting of the states is considerable larger. This indicates, that the minority electrons are affected much more strongly by the alloy layer. This can be understood from the muffin tin localized density of states as shown in Fig. 6.13. Completely analogously to the MnCu alloy discussed in the previous chapter, the local density of states at the Mn atoms is dominated by the d -like Mn states lowest in energy. The majority Mn-localized local density of states does not contain any d -contribution and is a pure s -like density of states. The interpretation presented here, assumes that the minority Ag s -electrons can be scattered by the additional d -states. This introduces a significant reflection of minority Ag electrons from the alloy layer.

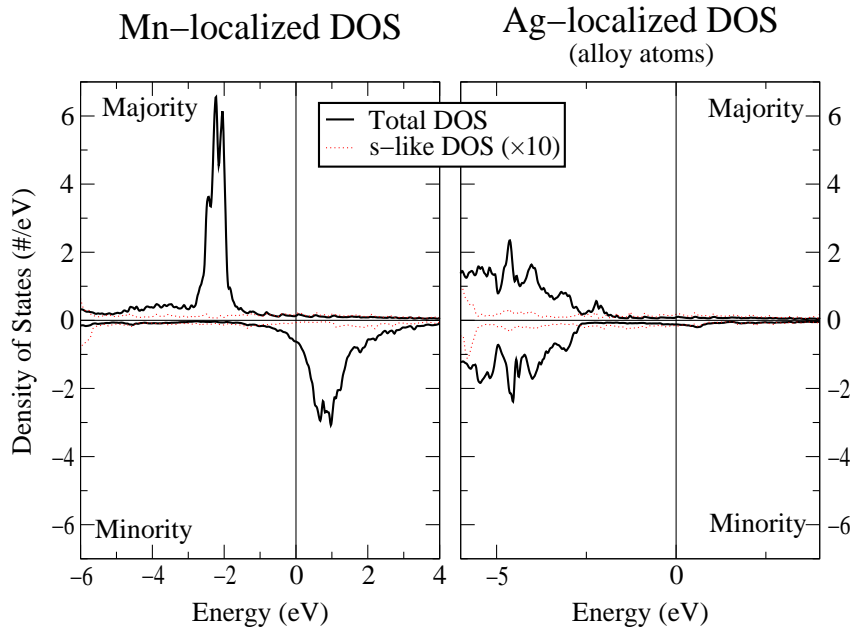


Figure 6.13: Density of states localized in the muffin-tin spheres of the MnAg alloy buried under 10 monolayer of Ag. The left plot shows the local density of states inside the Mn sphere. The right plot shows the corresponding local density of states for the alloy-Ag muffin tin spheres.

This reduced transmission of s -electrons through the alloy layer will lead to the formation of a quantum well state in the 10 monolayer Ag film between the alloy and the vacuum. However, this reflection is of course not perfect and therefore the eigenstates of the system will in fact be a superposition of a quantum well state of formed in the 10 monolayer thick Ag on both sides of the alloy and of a quantum well state confined to the whole 21 layer film.

Since this 21 layer film should be a model of the true semi-infinite crystal one now has to examine carefully which properties of first star contribution to the local density of states are a result of the formation of the 10 layer quantum well system and which properties will origin from the finite film thickness of 21 layers.

Most clearly, the first star contribution (Fig. 6.14) to the local density of states shows some oscillations. Approximately every 0.5 eV the first star contribution changes its sign. As discussed several times already this will correspond to different states having major impact of the local density of states. If the first star component of the local density of states is positive, which corresponds to a protrusion over the Mn atoms, the states involved must be even states with respect to a mirror plane through the Mn atoms in the unit-cell. The negative sign on the other hand corresponds to odd states being most important.

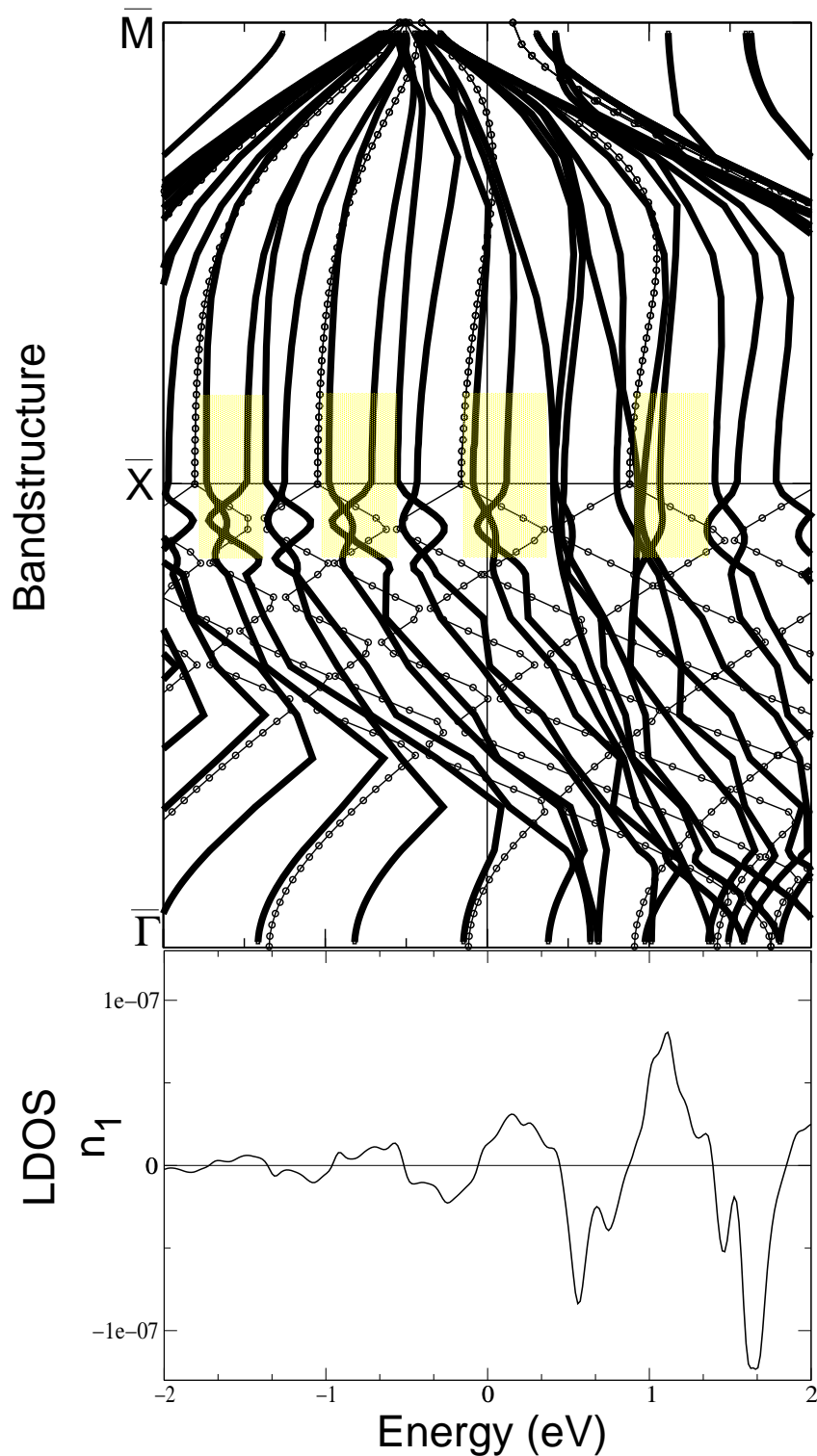


Figure 6.14: Minority band-structure and minority first star coefficient of the local density of states of a MnAg alloy buried under 10 monolayer of Ag on both sides. The thin bands marked with circles show the band-structure of a 10 layer pure Ag quantum well system. The strong oscillations in the first star contribution to the local density of state can be explained by the formation of quantum well states. The energy range in which the first star contribution to the local density of states is positive is marked by gray boxes in the band-structure near the \bar{X} -point.

At this point of the argument one should focus on the bands of the 10 layer perfect quantum well system as included in Fig. 6.14. Along the line from \bar{X} to \bar{M} these bands are twofold degenerate, since both the odd and even bands with respect to the mirror plane must have the same energy because of the additional translational symmetry of the smaller pure Ag $p(1 \times 1)$ unit-cell. At \vec{k}_{\parallel} -values along the $\bar{\Gamma}$ - \bar{X} line which break this symmetry, these two degenerate bands show a very high dispersion with opposite slope.

These quantum well states of an 11 layer Ag film can now be connected to the energies at which the first star contribution to the local density of states changes its sign. All states of the 21 layer setup containing the alloy layer, which are slightly higher in energies than a pure 10 monolayer quantum well state to contain a strong contribution of an even 10 layer quantum well state. Similarly any state with an energy just below an 10 layer quantum well level will hybridize with an odd quantum well state and therefore contain a negative contribution to the local density of states.

This scheme can explain the oscillations of the sign of first contribution the local density of states. The sign of this contribution changes at every energy level of a 10 layer quantum well state and in the middle between these levels. This leads to the different rages in energy which are marked by the gray boxes in Fig. 6.14.

This scheme of interpretation can also be successfully applied to the alloy covered by a film of 5 monolayers of Ag. As Fig. 6.15 shows, in this case both the energy levels of the 5 layer quantum well system and of the 11 layer film are less dense and the distance between two energies with zero first star contribution to the minority local density of states is increased to nearly 1 eV. However, the comparison of the band-structure with the plot of the first star contribution to the local density of states plot reveals, that the oscillations in this case still correspond nearly exactly with the positions deduced from the the 5 layer quantum well states. The only exception can be spotted at about 1 eV. Below that energy range one would expect the first star contribution to the local density of states to be negative. The small maximum at approximately 0.7 eV is unexpected. This is probably due to the influence of states with different \vec{k}_{\parallel} -value, i.e. from states not belonging to the \bar{X} -point. A closer look at the band-structure shows that in fact in this region some bands even cross the band of odd 5 layer quantum well states which will probably lead to an extremely strong hybridization (Fig. 6.15 rectangle). However, the same band crosses the even band at a smaller \vec{k}_{\parallel} value. (Fig. 6.15 circle). These bands furthermore are very flat showing that these states will probably not be Ag s -states but Mn d -localized states and one could therefore expect that the effect of these bands is ill described in the framework of quantum well states.

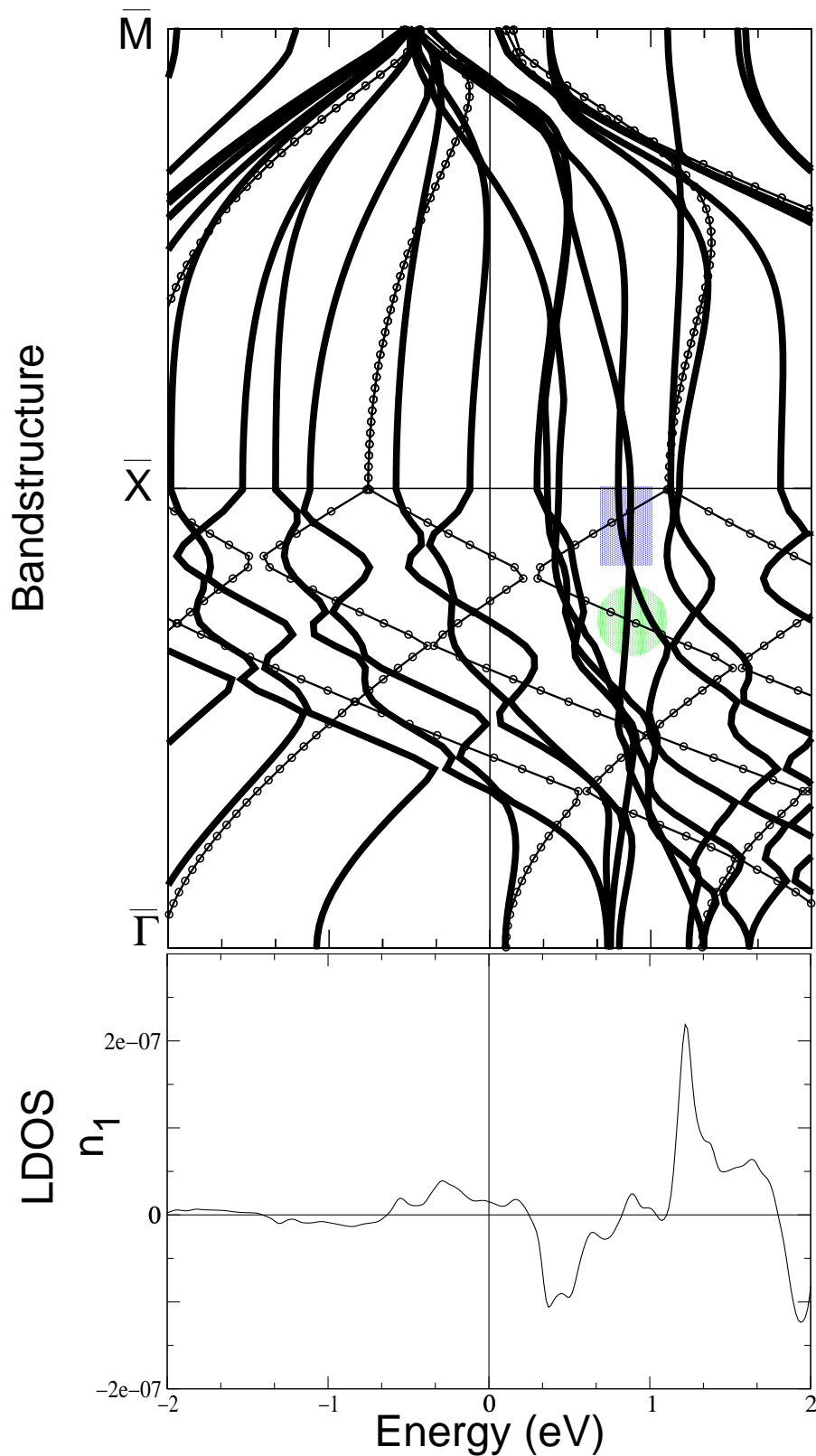


Figure 6.15: Minority band-structure and minority first star coefficient of the local density of states of a MnAg alloy buried under 5 monolayer of Ag on both sides. The thin bands show the band-structure of a perfect 5 layer Ag quantum well system. Two regions in the band-structure are marked for reference.

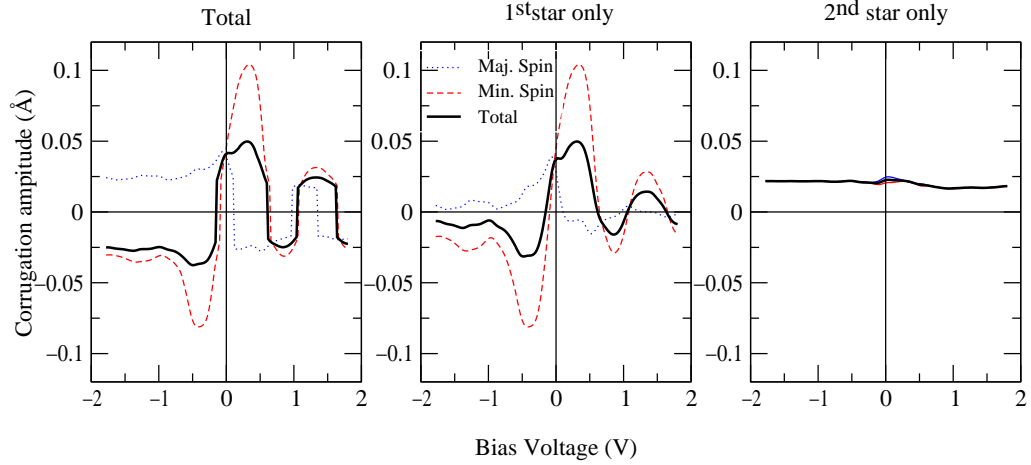


Figure 6.16: STM corrugation amplitude for a MnAg alloy layer buried under 10 monolayers of Ag.

The very high peak at 1.2 eV on the other hand can be related directly to a state which probably will contain a huge contribution of a quantum well state because at this energy a 5 layer Ag quantum well energy corresponds to the the band energy obtained for the 11 layer system. The hybridization between those states will therefore be extremely large. However, this is probably again an example of an artificial result, arising from the correspondence of the energy of the energy of the 10 layer quantum well state with the state calculated in the 21 layer film. In the dense band-structure of a true semi-infinite setup this would not be extraordinary any more.

Concluding, some very strong indications have been presented that show that the main feature, namely the oscillations, in the first star contribution to the local density of state in the vacuum can be successfully related to the formation of a quantum well in the Ag film between the alloy and the surface. These quantum well states break the symmetry of the surface and therefore the local density of states shows the symmetry of the alloy even in the vacuum.

6.3.4.3 Imaging through quantum well states

All the analysis presented so far focussed on the first star contribution to the local density of states in the vacuum. Now the corrugation amplitude as obtained for the deeply buried alloys will be discussed.

The alloy covered with 10 monolayer of Ag will be used as an example of a a deeply buried alloy system. Figure 6.16 shows the corrugation amplitude obtained from setup (4) as introduced in section 6.3.2.

The most important result of Fig. 6.16 is the dominance of the first star contribution. It can be seen that the first star contribution even though it is no longer as large as for the surface alloy still dominates the total corrugation amplitude. The second star contribution is significantly smaller. This means that the corrugation measured in an STM is dominated by the $c(2\times 2)$ contribution, i.e. the STM still shows the $c(2\times 2)$ structure of the alloy and not the $p(1\times 1)$ surface cell.

A closer look at the important contribution of the first star coefficient allows one to make contact to the discussion of the previous sections. The majority spin contribution is relatively small. The minority spin induced corrugation amplitude is large. The minority spin contribution also oscillates strongly. These oscillations are the same oscillations as seen in the local density of states. The amplitude of these oscillations decays rapidly with increased bias voltages because of the energy integration in the Tersoff-Hamann model (Eq. (4.21)).

This results therefore indicate that the formation of a quantum well between the alloy layer and the crystal surface makes it possible to detect the $c(2\times 2)$ structure of the buried alloy at the surface. Quantum well states do break the additional symmetry of the surface and the reduced symmetry of the alloy layer becomes visible in the STM.

In principle this mechanism should be independent from the thickness of the quantum well, i.e. it should not depend on the number of Ag layers which are on top of the alloy. The amplitude of the corrugation showing the $c(2\times 2)$ structure should remain approximately constant.

The period of the oscillation, however, will become shorter and therefore this will introduce a limitation on the maximal Ag film thickness through which the alloy could be detected. Since the energy resolution of an STM could lie in the order of meV this decrease of the oscillation period will not be a limitation until well over 100 monolayer coverage.

In practise, the preparation of the film will introduce a much stricter limitation. As soon as the alloy layer or the surface will not be ideally flat, interference effects will probably destroy the quantum well states since the states, which are important here, have large values of \vec{k}_{\parallel} .

Chapter 7

Summary and Outlook

In this work it has been shown that the interpretation of STM images of highly ordered structures on the atomic scale is not always a simple task.

In the case of the $c(2\times 2)\text{MnCu}/\text{Cu}(100)$ surface alloy much experimental data is available. The large relaxation of this surface alloy seems to make the interpretation of the STM results particularly easy. However, the *ab initio* results presented in chapter 5 indicate, that the correct interpretation of the experimental results will be only possible if one takes the actual electronic configuration into account. The assumption that the corrugation amplitude of the STM tip will be dominated by the surface relaxation of the alloy turns out to be very doubtful. This simple interpretation predicts the protrusions in an STM image to be at the Mn sites. In a detailed analysis I have shown, that this is probably incorrect. The protrusions can be seen at the Cu sites of the $c(2\times 2)$ alloy and the Mn atoms are imaged as depressions.

This result indicates that the STM is not a tool which always give results easy to relate to the actual surface geometry or topography. In this work only results for one MnCu surface alloy and a MnAg surface alloy have been presented. However, this difficulty in the interpretation of STM results is a rather general feature of atomically resolved STM images on metal surfaces. The results for these two alloys cannot easily be generalized to other structures. Instead, a similar analysis of the electronic structure of the system under investigation has to be performed for any dense surface structure.

In the last chapter of this work, the possibility to detect atomic structures buried underneath the metal surface by the STM has been investigated. It turned out that it might be possible to obtain STM images which show the influence of the subsurface layers. The $c(2\times 2)\text{MnAg}/\text{Ag}(100)$ alloy should be detectable even if it

is buried with 10 additional monolayers of Ag. The formation of a quantum well between the surface and a buried alloy structure has found to mediate the deeply buried MnAg alloy to the surface. This indicates, that the structure investigated in this work is only one example of a much wider range of systems in which it will be possible to probe subsurface structures with STM and STS. The formation of quantum wells open a wide range of exciting new experimental systems which might become accessible to STM-studies. Especially the STS of thin-multilayer systems might be an interesting field to explore. First groups started to investigate similar systems with astonishing results [ACM98, HAB⁺99].

The theoretical approach presented here allows extensions in several directions. The most obvious approach which already is partly implemented is the replacement of the Tersoff-Hamann model by the numerical evaluation of Bardeen's matrix elements. One no longer assumes the density of states of the tip to be a constant or the tip wave-functions to be atomic s - or d_{z^2} -states, but instead treats the electronic structure of the tip and the sample on the same footing. The FLEUR-program can be used to calculate both the tip Ψ^T and the sample Ψ^S wave-functions in the vacuum region. These wave-functions then are used to evaluate Bardeen's matrix element $M_{\mu\nu}^{ST} \propto \int (\Psi^{T*} \nabla \Psi^S - \Psi^S \nabla \Psi^{T*}) d\vec{S}$ numerically. This approach allows one to include the true electronic structure of the tip. This will be especially important for STS. In several test calculations this improved theoretical treatment showed little effect on the main features of the STM-image. This improved treatment of the tip suffers from the non-trivial problem that the geometry of the tip is not known experimentally and that many different tip configurations have to be tested.

Even this improved model will be restricted in its application by the approximations made by Bardeen. Probably the most important restriction will be the improper description of the vacuum barrier at higher bias voltages. To include effects due to the change in the barrier height or effects which will occur in tunnel processes through non-conducting materials one has to overcome Bardeen's theoretical approach, which will be a major task for the future.

Bibliography

- [AB98] R. Abt and S. Blügel. First-principles investigation of the formation of Mn/Ag(100) surface alloy. *Philosophical Magazine B*, 78:659–663, 1998.
- [Abt] R. Abt. private communication.
- [ACM98] I. B. Altfeder, D. M. Chen, and K. A. Matveev. Imaging buried interfacial lattices with quantized electrons. *Phys. Rev. Lett.*, 80(22):4895, 1998.
- [Alv95] S. F. Alvarado. Tunneling potential barrier dependence of electron spin polarization. *Phys. Rev. Lett.*, 75:513, 1995.
- [AM76] Niel W. Ashcroft and N. David Mermin. *Solid State Physics*. Saunders College Publications, 1976.
- [AMC97] I. B. Altfeder, K. A. Matveev, and D. M. Chen. Electron fringes on a quantum wedge. *Phys. Rev. Lett.*, 78(14):2815, 1997.
- [And75] O. K. Anderson. *Phys. Rev. B*, 12:3060, 1975.
- [BGW98] M. Bode, M. Getzlaff, and R. Wisendanger. Spin-polarized vacuum tunneling into the exchange-split surface state of Gd(0001). *Phys. Rev. Lett.*, 81:4256, 1998.
- [Blü96] S. Blügel. Magnetically stabilized surface alloys. *Appl. Phys. A*, 65:595, 1996.
- [Che90] C. J. Chen. Tunneling matrix elements in three-dimensional space: The derivative rule and the sum rule. *Phys. Rev. B*, 42(14):8841, 1990.
- [Che92] C. Julian Chen. Effects of $m \neq 0$ tip states in scanning tunneling microscopy: The explanations of corrugation reversal. *Phys. Rev. Lett.*, 69:1656, 1992.

- [Che93] C. Julian Chen. *Introduction to Scanning Tunneling Microscopy*. Oxford University Press, New York, Oxford, 1993.
- [Cun74] S.L. Cunningham. Special points in the two-dimensional brillouin zone. *Phys. Rev. B*, 10:4988, 1974.
- [Esc96] H. Eschrig. *The fundamentals of Density Functional Theory*. Teubner, Stuttgart, Leipzig, 1996.
- [FHW92] T. Flores, M. Hansen, and M. Wuttig. Structure and growth of Mn on Cu(100). *Surf. Sci.*, 279:251, 1992.
- [FJW97a] T. Flores, S. Junghans, and M. Wuttig. Atomic mechanisms for the diffusion of Mn atoms incorporated in the Cu(100) surface: an STM study. *Surf. Sci.*, 371:1, 1997.
- [FJW97b] T. Flores, S. Junghans, and M. Wuttig. Atomic mechanisms for the formation of an ordered surface alloy: an STM investigation of Mn/Cu(100). *Surf. Sci.*, 371:14, 1997.
- [GBW82a] Ch. Gerber G. Binnig, H. Rohrer and E. Weibel. *Phys. Rev. Lett.*, 49:57, 1982.
- [GBW82b] H. Rohrer Ch. Gerber G. Binnig and E. Weibel. *Phys. Rev. Lett.*, 50(120), 1982.
- [Gen] O. Genser. Reine und Si-bedeckte Fe(001)-Oberfläche im Rastertunnelmikroskop: Begleitende Bandstrukturechnungen. Master's thesis, Technische Universität Wien.
- [HAB⁺99] S. Heinze, R. Abt, S. Blügel, G. Gilarowski, and H. Niehus. Scanning tunneling microscopy images of transition-metal structures buried below nobel-metal surfaces. *Phys. Rev. Lett.*, 83:4808, 1999.
- [Ham79] D. R. Hamann. *Phys. Rev. Lett.*, 212:662, 1979.
- [HBP⁺98] S. Heinze, S. Blügel, R. Pascal, M. Bode, and R. Wiesendanger. Prediction of bias-voltage-dependent corrugation reversal for STM images of bcc (110) surfaces: W(110), Ta(110), and Fe(110). *Phys. Rev. B*, 58:16432, 1998.
- [Hei97] Stefan Heinze. Ab-initio elektronenstrukturechnungen im hinblick auf rtm-experimente an fe/w(110). Master's thesis, Universität Hamburg, 1997.

- [HK64] P. Hohenberg and W. Kohn. *Phys. Ref.*, 136:B864, 1964.
- [Jan78] J.F. Janak. Proof that $\partial e/\partial n_i = \epsilon_i$ in density-functional theory. *Phys. Rev. B*, 18(12):7165, 1978.
- [JG89] R. O. Jones and O. Gunnarson. Density functional formalism, its applications and prospects. *Rev. Mod. Phys.*, 61:689, 1989.
- [KA75] D.D. Koelling and G.O. Arbman. *J. Phys. F*, 5:2041, 1975.
- [Koh83] Walter Kohn. Density functional theory: Basic results and some observations. In Reiner M. Dreizler and Joao da Providencia, editors, *Density Functional Methods in Physics*. NATO ASI Series, 1983.
- [KPF97] H. Krakauer, M. Posternak, and A. J. Freeman. Linearized augmented plane-wave method for the electronic band structure of thin films. *Phys. Rev. B*, 19:1706, 1997.
- [KS65] W. Kohn and L.J. Sham. *Phys. Rev.*, 140:A1133, 1965.
- [Kur97] Philipp Kurz. Non-collinear magnetism of ultrathin magnetic films. Master's thesis, RWTH Aachen, 1997.
- [Lev79] Mel Levy. Universal variational functionals of electron densities, first-order density matrices, and natural spin-orbits and solution of the v-representability problem. *Proc. Natl. Acad. Sci.*, 76(12):6062, 1979.
- [LLP79] L. D. Landau, E. M. Lifshits, and L. P. Pitaevskij. *Quantenmechanik*, volume 3 of *Lehrbuch der theoretischen Physik*. Akademie Verlag, Berlin, 6 edition, 1979.
- [LYB⁺99] V. P. LaBella, H. Yang, D. W. Bullock, P. M. Thibabo, Peter Kratzer, and Matthias Scheffler. Atomic structure of the GaAs(001)-(2×4) surface resolved using scanning tunneling microscopy and first-principles theory. *Phys. Rev. Lett.*, 83:2989, 1999.
- [MJW78] V.L. Moruzzi, J. F. Janak, and A. R. Williams. Pergamon, New York, 1978.
- [NHDJ⁺94] H.P. Noh, T. Hashizume, Y. Kuk D. Jeon, H.W. Pickering, and T. Sakurai. Structure of the Mn-induced Cu(100)-c(2x2) surface. *Phys. Rev. B*, 50:2735, 1994.

- [OT95] W. L. O'Brien and B.P. Tonner. Magnetic properties of Mn/Cu(001) and Mn/Ni(001)c(2x2) surface alloys. *Phys. Rev. B*, 51:617, 1995.
- [OZT93] W. L. O'Brien, J. Zhang, and B. P. Tonner. Local magnetic properties and magnetic ordering of the two-dimensional surface alloy c(2x2)Mn/Cu(001). *J. Phys.: Condens. Matter*, 5:L515, 1993.
- [Pen96] Rossitza Pentcheva. Ab-initio Rechnungen zum Zusammenhang zwischen Magnetismus und Struktur ultradünner Filme. Master's thesis, Universität Köln, 1996.
- [Per83] John P. Perdew. What do the Kohn-Sham orbital energies mean? How do atoms dissociate? In Reiner M. Dreizler and Joao da Providencia, editors, *Density Functional Methods in Physics*. NATO ASI Series, 1983.
- [PZ81] J. P. Perdew and A. Zunger. *Phys. Rev. B*, 23:5048, 1981.
- [RGC⁺97] O. Rader, W. Gudat, C. Carbone, E. Vescovo, S. Blügel, R. Kläsges, W. Eberhardt, M. Wuttig, J. Redinger, and F. J. Himpsel. Electronic structure of two-dimensional magnetic alloys: c(2x2) Mn on Cu(100) and Ni(100). *Phys. Rev. B*, 55:5404, 1997.
- [RVW⁺97] O. Rader, E. Vescovo, M. Wuttig, D. D. Sarma, S. Blügel, F. J. Himpsel, A. Kimura, K.S. An, T. Mizokawa, A. Fujimori, and C. Carbone. Correlation satellite driven by reduced dimensionality. *Europhys. Lett.*, 39:429, 1997.
- [Sch93] F. Schwabl. *Quantenmechanik*. Springer, 4 edition, 1993.
- [SHV96] M. Schmid, W. Hebenstreit, and P. Varga. Quantum wells and electron interference phenomena in Al due to subsurface noble gas bubbles. *Phys. Rev. Lett.*, 76:2298, 1996.
- [Sin94] D. J. Singh. *Planewaves, Pseudopotentials and the LAPW Method*. Kluwer Academic Publishers, Boston, Dordrecht, London, 1994.
- [SKHG97] P. Schieffer, C. Krembel, M. C. Hanf, and G. Gewinner. Room-temperature instability of the Mn/Ag(100) interface in the monolayer range. *Phys. Rev. B*, 55:13884, 1997.
- [SKHG98] P. Schieffer, C. Krembel, M.C. Hanf, and G. Gewinner. Growth of a flat Mn monolayer on Ag(001). *Phys. Rev. B*, 57:1141, 1998.

- [SKMC⁺99] P. Schieffer, C. Krembel, M.-C.Hanf, M.-H. Tuilier, P. Wetzels, G. Gewinner, and K. Hricovini. High spin state of Mn in an ideal monolayer on Ag(001). *Eur. Phys. J. B*, 8:165–168, 1999.
- [SLP99] A.B. Shick, A. I. Lichtenstein, and W. E. Pickett. Implementation of the LDA+U method using the full-potential linearized augmented plane-wave basis. *Phys. Rev. B*, 60(15):10763, 1999.
- [SW93] Max Schubert and Gerhard Weber. *Quantentheorie*. Spektrum Akademischer Verlag, Heidelberg, 1993.
- [TH83] J. Tersoff and D.R. Hamann. Theory and application for the scanning tunneling microscope. *Phys. Rev. Lett.*, 50:1998, 1983.
- [vBH72] U. von Barth and L. Hedin. Local density approximation. *J. Phys. C.*, 5:1629, 1972.
- [vdKvK95] R.G.P van der Kraan and H. van Kempen. Growth of Mn on Cu(100) studied by STM: the c(2x2) and pgg(4x2) ordered surface alloys. *Surf. Sci.*, 338:19–30, 1995.
- [VSB⁺97] B. Voigtländer, V. Scheuch, H.P. Bonzel, S. Heinze, and S. Blügel. Chemical identification of atoms at multicomponent surfaces on an atomic scale: CoSi₂(100). *Phys. Rev. B*, 55:R13444, 1997.
- [VWN80] S.H. Vosko, L. Wilk, and N. Nusair. Accurate spin-dependent electron liquid correlation energies for local spin density calculations: a critical analysis. *Can. J. Phys.*, 58:1200, 1980.
- [WGB93] M. Wuttig, Y. Gauthier, and S. Blügel. Magnetically driven buckling and stability of ordered surface alloys: Cu(100)c(2x2)Mn. *Phys. Rev. Lett.*, 70:3619, 1993.
- [WGG⁺90] R. Wiesendanger, H.-J. Güntherodt, G. Güntherodt, R. J. Gambino, and R. Ruf. Observation of vacuum tunneling of spin-polarized electrons with the scanning tunneling microscope. *Phys. Rev. Lett.*, 65:247, 1990.
- [WJFB96] M. Wuttig, S. Junghans, T. Flores, and S. Blügel. Comment on "structure of the Mn-induced Cu(100) c(2x2) surface. *Phys. Rev. B*, 53:7551, 1996.

- [WKFG93] M. Wuttig, C.C. Knight, T. Flores, and Y. Gauthier. LEED structure determination of two ordered surface alloys: Cu(100)-c(2x2)Mn and Ni(100)-c(2x2)Mn. *Surf. Sci.*, 292:189–195, 1993.
- [WKWF81] E. Wimmer, H. Krakauer, M. Weinert, and A.J. Freeman. Full-potential self-consistent linearized-augmented-plane-wave method for calculating the electronic structure of molecules and surfaces: O₂ molecule. *Phys. Rev. B*, 24:864, 1981.